CHARACTERIZATION OF MAGNETIC DYNAMICS EXCITED BY SPIN TRANSFER TORQUE IN A NANOMAGNET

A Dissertation

Presented to the Faculty of the Graduate School

of Cornell University

in Partial Fulfillment of the Requirements for the Degree of

Doctor of Philosophy

by

Yongtao Cui

January 2012

CHARACTERIZATION OF MAGNETIC DYNAMICS EXCITED BY SPIN TRANSFER TORQUE IN A NANOMAGNET

Yongtao Cui, Ph.D.

Cornell University 2012

This dissertation presents our investigation of the effects of spin transfer torque on a nanoscale ferromagnet. Spin transfer torque is generated by the transfer of angular momentum from spin polarized electrons to a ferromagnet. This torque provides an efficient means to manipulate the dynamic motion of the magnetization of a nanomagnet, and can be strong enough to induce magnetization reversal or steady-state precession. We have developed new techniques to characterize such dynamics induced by spin transfer torque.

In the first study, we perform an experiment demonstrating that spin transfer from a microwave current pulse can produce a resonant excitation of a nanomagnet and improve switching characteristics in combination with a square current pulse. With the assistance of a microwave-frequency pulse, the switching time is reduced and achieves a narrower distribution than when driven by a square current pulse alone, and this can permit significant reductions in the integrated power required for switching.

In the second study, we develop a single-shot electrical technique to capture the magnetic dynamics during the spin torque switching of a magnetic tunnel junction in real time. With substantially improved sensitivity compared to previous experiments, we directly resolve the resistance oscillations associated with magnetic dynamics, yielding detailed views of switching modes and variations between events. This also enables us to analyze the coherence times

and non-equilibrium spectra of the magnetic dynamics under the effects of thermal fluctuations.

In the last study, we use X-ray microscopy to image the magnetic normal modes which serve as the basis states for the magnetic dynamics. By applying a microwave current at the normal mode frequency, we selectively excite a particular normal mode and perform time resolved X-ray microscopy measurement to image its spatial structure. We observe different degrees of spatial non-uniformity for two mode branches we imaged. The branch with higher frequency is more spatially uniform than the other. At low magnetic fields where the two modes are close in frequency and excited at the same time, the more non-uniform mode dominates the overall behavior of the dynamics.

BIOGRAPHICAL SKETCH

Yongtao Cui was born on August 7th, 1983, in Yuxia, a small town 40 miles away from Xi'an, China. He was the only child in the family due to China's "One Child" policy. His childhood though was not lonely. He played a lot with his fellow friends after school time and often forgot to go back home for dinner so that his mother had to look for him all over the places. He attended Hui'an Elementary School (6 years) and Hui'an Middle School (3 years), both of which were affiliated with the company his parents worked at. He enjoyed the science courses more than others, since he learned how to explain things with simple principles and equations, without having to memorize a lot of stuff. He also loved playing sports. He played ping-pong and soccer, and made it to the school teams. Today he is still a big soccer fan and plays regularly.

In 1998 when he finished middle school, he got an opportunity to study at the High School Affiliated with Xi'an Jiaotong University, located in the city of Xi'an. He thus had to leave home and started dorm life earlier than many of his peers, which gained him a lot of funny memories and invaluable friendships. He attended the physics study group and learned many tricks on solving physics Olympiad problems. He also got some luck in the competition and won a Gold medal in the Chinese Physics Olympiad in his senior year, which allowed him to skip the National College Entrance Exam and enter the School of Physics in Peking University in 2001.

His freshman year in Peking University was basically a loop connecting three places: dorm, library and classrooms. In the sophomore year, this loop became larger as the university arranged the entire class to move into new dorms outside campus, which resulted in an one-hour bicycle time for a roundtrip commute. Later in the year, two things happened. "SARS" broke

out in the city. The empty streets did not generate much fear preventing him from biking to physics classes but rather reduced his commute time by quite a bit. At around the same time, he received the Chun-Tsung Scholarship, an undergraduate research program which led him into the research world of experimental physics for the first time. Working with Prof. Dapeng Yu, he practiced growing semiconductor nanowires and watching them with SEM and AFM. He also tried doping them with magnetic elements. Even though without much success, he became quite interested in magnetic materials and eventually decided to study spins in graduate school. In his junior year, he spent four months in National University of Singapore as an exchange student. During this visit, he realized that studying physics in an English-speaking environment was not entirely terrible, so he applied for graduate school in the United States.

In the summer of 2005, he took a 13-hour flight and enrolled in the PhD program of Applied Physics at Cornell University. He joined the Ralph group at the end of his first year and started playing with nanomagnets and microwave equipment. Ralph group provided him with very rich resources to satisfy his curiosity about the nano world. He learned not only how to make devices on the length scale of a few nanometers but also how to manipulate them on the time scale of less than a nanosecond. He even got a chance to load his devices next to the high energy accelerator in Berkeley and shine them with ultra-bright X-ray photons. He has now completed all the requirements for his PhD degree upon finishing up this last part of the biographical sketch. His next stop will be on the other side of the continent where he will study electron dynamics as a postdoc in Prof. Zhi-Xun Shen's group at Stanford University.

To my parents and my wife, for their love and support.

ACKNOWLEDGEMENTS

Six years of graduate school is not a short time. It would not have been possible for me to survive through without help from so many people. I would like to take this opportunity to acknowledge all the people who have encouraged, helped, and supported me over the years.

First of all, I would like to thank my advisor, Prof. Dan Ralph, from whom I have been fortunate enough to receive tremendous guidance and knowledge during these past years. I have learned a great deal about how to be a good scientist - how to think of the big picture and how to grasp the essence of the problem by focusing on its physics. His suggestions not only have helped me solve so many problems in my experiments, but also have been good examples to show me how to tackle a problem in a physicist's way. Dan has also set a good example on how to be a good advisor and manager. His care on every student in the group has allowed everyone to work creatively and efficiently. I am grateful that he has given me the freedom to pursue the research directions that interested me and has always been available whenever I needed his advice. I also want to thank him for his patience and help in improving my writing and presentation skills. In all aspects, I could not have asked for a better advisor than Dan to guide my graduate research.

I would also like to thank Prof. Bob Buhrman for answering many of my questions, as well as raising many questions in reviewing my work. His questions and comments have been a key to help ensure the quality of my research. I want to thank both Bob and Dan for finding the funds to buy equipments which have made our research possible and much easier.

I also want to thank Prof. Bruce van Dover for teaching me magnetics and serving on my committee. His "Magnetic Materials" course was the most useful

course I have taken in graduate school and helped me quickly get on the track to the world of magnetics.

All the Ralph group people have helped and supported me along my way to the PhD, both scientifically and personally. Their talent and creativity have inspired me all the time, and their companion and encouragement have made life in basement much easier, especially during my depressing times.

Jack Sankey, Kiran Thadani and Zhipan Li were my mentors and teachers when I joined the group. Jack taught me everything about the measurement techniques from wire bonding to microwave measurement. He gave me a jump start for my first project with his circuit to generate a microwave pulse. He was also the original author of the "Ralph Studio Xtreme" LabWindows program and the "spinmobules" python scripts, from which I have benefited a lot in my data taking and analysis. I have also learned many programming tricks reading his codes and the comments in between the lines, and he even supplied me with updated python codes after he left. Kiran taught me everything about the nanopillar fabrication process and helped me all the way through my first fab. She has also been a good friend who has provided much support not only in research but also in the life outside Clark where I have enjoyed many Indian meals with her in Sangam and Diamond's. Zhipan Li worked in Ralph group as a postdoc for a little over one year during which he influenced me quite a bit. He started the whole X-ray project and led me into a very different area. He has also shared with me a lot of his experience and advice on career development.

Sufei Shi has been one of my closest friends in Ithaca. He has been like a big brother to me, whom I can ask for suggestions on almost anything, physics related or not. We share many common interests on electronic gadgets and finding deals to questionably save money. It has also been fun to hear his comments

and insights about the stock market and China's current events. Chen Wang has directly contributed to many of my work. I appreciate discussions with him about experiments, and I admire his efficiency and intriguing insights about many things. Special thanks to Lin Xue who has helped a lot on the X-ray device fabrication and measurements and many other things. Without his accompany and help, my five months on crutches would have been much worse[1]. I have also enjoyed many photography activities with him.

I also want to thank Joshua Parks, who has often encouraged me and provided many helpful suggestions, and has shared his North Star lunch benefits with all of the group. Thanks to Eugenia Tam for many interesting chats and for bringing fun to G3 (with Josh and friends from Abruna Group). Thanks to Wan Li who has been a thoughtful friend and helped with many P-card purchases. Many thanks to Takahiro Moriyama. I learned much about microwave techniques from him and benefited a lot from the hardware parts he made and the group server he set up. I also thank Ted Gudmundsen for many fun talks, for setting up the new sputtering system which saved me a lot of wait time on pumping down, and for keeping many stuff in the group organized. Thanks also to Alex Mellnik for the sputtering system and for the help on measurements during my leg recovery. Thanks to Colin Heikes for many interesting conversations on culture, life, sports and more. I would also like to thank other previous Ralph group members: Kirill Bolotin, Ferdinand Kummeth, Jacob Grose, Saikat Ghosh and new Ralph group members: Jennifer Grab, David MacNeill, Greg Stiehl, for making this group such a fun place.

In the past years, I have been lucky to collaborate with a bunch of great people in the Buhrman group. Thanks to Ozhan Ozatay, Greg Fuchs and Pat Braganca, for teaching me spin torque, training me on various fabrication

[1]In fact, the crutches were borrowed from him.

tools, and more recently giving me advice on career development. Thanks to Vlad Pribiag for discussions on the X-ray device fabrication and experiment, to Praveen Gowtham for telling many funny stories, to Luqiao Liu, Hsin-Wei Tseng and Yun Li for many useful suggestions on fabrications, to Oukjae Lee and Hsin-wei Tseng for bearing with my experiment schedules on the pulsers and oscilloscope, to Junbo Park for the soccer plays, and to Chi-Feng Pai for the suggestions on my Taipei trip. I also want to thank all the Buhrman group members for maintaining the deposition and etching tools at smooth operation status, which requires a lot of time and efforts and directly benefits everyone in their nanopillar fabrications.

I would also like to thank all my collaborators outside Cornell. I am grateful to Giovanni Finocchio at University of Messina and Mario Carpentieri at University of Calabria for doing micromagnetic simulations for my single-shot and x-ray experiments. I want to thank Peter Fischer, Mi-Young Im and Tolek Tyliszczak at the Advanced Light Source for the fantastic support during the X-ray experiments. I thank Jordan Katine at Hitachi GST for providing nice low-RA MgO tunnel junction samples for my measurement.

I want to thank all the terrific support I have received from Jon Shu and Steve Kriske at CNS, Nate Ellis at the machine shop, all the staff members at CNF and CCMR, all of whom have been great sources of information and extremely helpful in different areas of my research.

My life in Clark Hall basement was made fun by a number of smart physicists in addition to Ralph and Buhrman people: Lu Bai, Ethan Bernard, Ji Cheng, Pinshane Huang, Jing Jin, Tchefor Ndukum, Bo Sun, Miao Wang, Yang Xie, Huolin Xin, Xiaodong Xu, Xinjian Zhou, and Paul Zhu.

Outside of the basement, I have also enjoyed chats, dinners, parties and

many other activities with many great friends at Cornell: Kun Bao, Hao Chen, Yong Chen, Heng Li, Jing Sha, Wenteng Shao, Xin Shi, Meng Wang, Qi Wang, Yao Weng, Yi Xie, Wei Zhang, Yang Zhang, and Ying Zheng. Many thanks also to all the members in Chinese Dragon Soccer Club.

I would like to thank a few friends from high school who came to America and provided moral support to each other during the study away from home. Every reunion with them has been exciting to me. Thanks to Kai Chen for his accompany during my day-and-night beam time in Berkeley, to Fan Guo for the postcards sent from different continents, to Fei Liu for driving 50 miles to pick me up when I missed my flight, to Chun Wang for all the encouragement and Milan game videos, and to Yongliang Yang for the help during my postdoc interview.

Finally, I want to reserve this last part to give my deepest thanks to my family. First, to my parents, who has raised me, taught me, and supported me with their unconditional love. Though they are on the other side of the planet, I know that they never stop caring about me for even a single minute. Second, to my wife's parents, who has not only raised such a wonderful woman, but also helped and supported me as if their own son. And now, to my wife, Zheng, who has stood by me, encouraging and powering me to move forward, step by step, and sharing with me all the bitterness and happiness in life. I would not have come through to this point today without you. I love you!

TABLE OF CONTENTS

LIST OF FIGURES

CHAPTER 1

INTRODUCTION

1.1 Background of Spintronics

Technological advancement in 20th century was largely based on the development of electronic devices. These devices provide the ability to control electron flows on microscopic scales, thereby enabling functions essential to applications in information technology. So far, most electrical devices are based on manipulating the electron's electric charge. However, besides electric charge, electrons also possess an intrinsic spin. In recent years, there have been intensive efforts to explore the possibility of manipulating electrons via their spins. Many achievements have been made along the way and have led to the opening of a new field, so called "spin based electronics" or "spintronics".

Spintronics has promising potential for making a new generation of devices that can offer great advantages such as non-volatility, increased speed and density, reduced power consumption, etc. [1] One good example of the benefit of spintronics is the "Giant Magneto-Resistance" (GMR) effect. It allows electrical detection of the magnetic orientation of a ferromagnet. Compared to the traditional method of detecting magnetization via electro-magnetic induction, the GMR effect becomes more efficient when the size of the magnet shrinks down to the nano-scale. The GMR effect is used in the read head of a hard drive to sense the magnetic field generated by the storage media, and its use has led to the increase of storage density by orders of magnitude. Another example is "Magnetic Random Access Memory" (MRAM), which uses the magnetic element for storing data. As the magnetic bit will not lose its magnetization

over time, it can retain information without consuming any power (it is "non-volatile"). The reading and writing of data are done electrically (unlike the mechanical reading and writing in hard drives), which allows very fast operation speed. The reading mechanism is through the GMR effect mentioned above. For writing, one promising mechanism is through "Spin Transfer" effect, which is in fact the main topic of this dissertation.

In the following sections, I will introduce some basics about spintronics, with emphases on the giant magnetoresistance effect and the spin transfer effect, which serve as the background information for the rest of this dissertation.

1.2 Giant Magnetoresistance Effect

The Giant Magnetoresistance effect, discovered in 1988 [2, 3], refers to the change of resistance of a ferromagnetic / non-magnetic / ferromagnetic metallic multilayer structure as the relative orientation of the magnetizations of two ferromagnetic layers changes, as illustrated in Fig. 1.1. The resistance is maximum when the magnetizations of two ferromagnetic layers are anti-parallel and minimum when they are parallel. The resistance difference between the maximum and minimum values can be as much as a few 10's of percent, much larger than the scale of the anisotropic magnetoresistance ($\sim 1\%$) in metals, which is the reason for its name - "Giant Magnetoresistance".

To understand the GMR effect, let us first consider a simple case: electrons passing through a single ferromagnetic layer. For a 3d transitional ferromagnetic metal like Ni, Co and Fe, ferromagnetism comes from the exchange coupling of the 3d electrons. In a simplified band structure for ferromagnetic metals, the

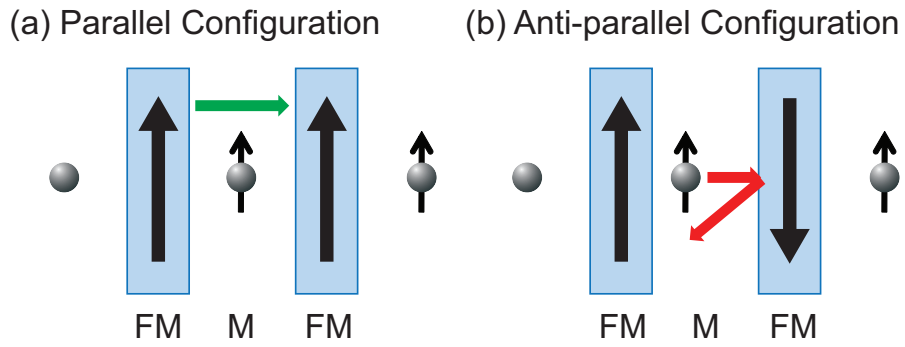

Figure 1.1: Illustration of the GMR effect.

exchange coupling results in an energy splitting of the 3d bands so that when the spin-up band and the spin-down band are filled up to the Fermi level there are more spin-up electrons than spin-down, so a net magnetization is induced. Another consequence is that the majority and minority spin bands also have different density of states at the Fermi level. (See Fig. 1.2 for illustration.) The conduction properties of a metal are primarily determined by the electrons near the Fermi level. Thus, when spin unpolarized electrons consisting of equal numbers of spin-up and spin-down electrons travel in a ferromagnet, different spins experience different resistances. In addition to the resistance within the ferromagnet, different types of spins also experience different scatterings at the ferromagnet / normal metal interface due to the band structure mismatch. Overall, one type of spin has a higher probability to transmit through than the other type. Therefore after passing through, electrons will become partially polarized in one spin direction. (For Fe/Cu, the polarization is in the majority spin direction, while for Fe/Cr where GMR was first discovered, it is in the minority spin direction.) The ferromagnet simply works as a spin filter.

When the spin polarized electrons travel into the non-magnetic spacer, they can maintain their spin directions for a relatively long distance when spin-dependent scattering is weak. For example, the spin diffusion length is on

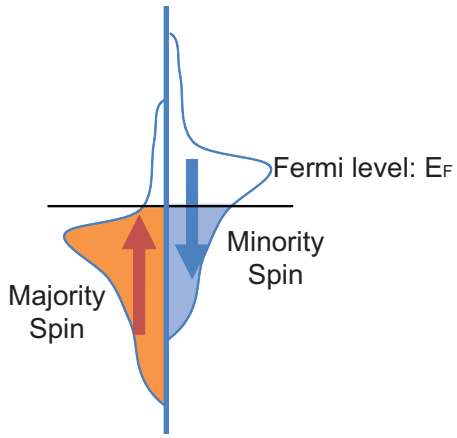

Figure 1.2: A simple band structure for ferromagnet. The majority and minority spin bands have an energy split so they have different densities of states at the Fermi level.

the order of 100's nm in Cu which is a typical material for the spacer. In the GMR structure, the spacer thickness is usually much smaller than the spin diffusion length so that the spin polarization is maintained when electrons reach the second layer. Then the probability for the electrons to transmit through the second ferromagnetic layer depends on the relative orientation of its magnetization and the electron spin polarization which is determined by the magnetization of the first layer. So when the second layer is parallel to the first layer, the same spin that has experienced a low resistance from the first layer will also have a higher probability to pass through the second layer. Overall this type of spin dominates the transport property through the multi-layer structure, which gives a low resistance. If the second layer is anti-parallel to the first layer, electrons of both spins experience high scattering in one layer or the other, and the resistance thus changes to a higher value. This resistance change is purely due to interactions with electron spins, so the GMR type of structure is also referred as a spin valve.

In general, the resistance of a GMR structure is minimum when the two

ferromagnetic layers are parallel, maximum when they are anti-parallel, and its dependence on the relative angle between the two layers, θ, has roughly a cosine form:

$$R(\theta) = R_P + (R_{AP} - R_P)\cos\theta \tag{1.1}$$

This resistance dependence on the relative orientation of the ferromagnetic moments makes GMR useful in a number of applications. For example, it provides a way to electrically detect the orientation of a ferromagnet. As mentioned previously, this has benefited greatly the hard drive industry. It is also the read-out mechanism in MRAM applications. Furthermore, GMR also has a broad impact in the study of spin dependent electron transport in solid state devices and its discovery is widely considered as the beginning of the spintronics field. For this reason, the 2007 Nobel Prize for Physics was rewarded to Fert and Grunberg for the discovery of GMR.

1.3 Tunnel Magnetoresistance

In a GMR structure, the non-magnetic metallic spacer can be replaced by a tunnel barrier. It will still show a similar effect of resistance dependence on the relative orientation of the ferromagnets, but with an even larger change. This is the "Tunnel Magnetoresistance" (TMR) effect. This effect was first discovered by Julliere in 1975 in Fe/GeO/Co magnetic tunnel junctions (MTJ). [4]. He also developed a simple model to explain the resistance change. His model assumes that the electron spin is conserved during the tunneling process. Therefore the tunneling probability of each type of spin can be calculated independently, as illustrated by Fig. 1.3. The tunneling probability across the tunnel barrier (and hence the conductance) is proportional to the density of states of both initial and

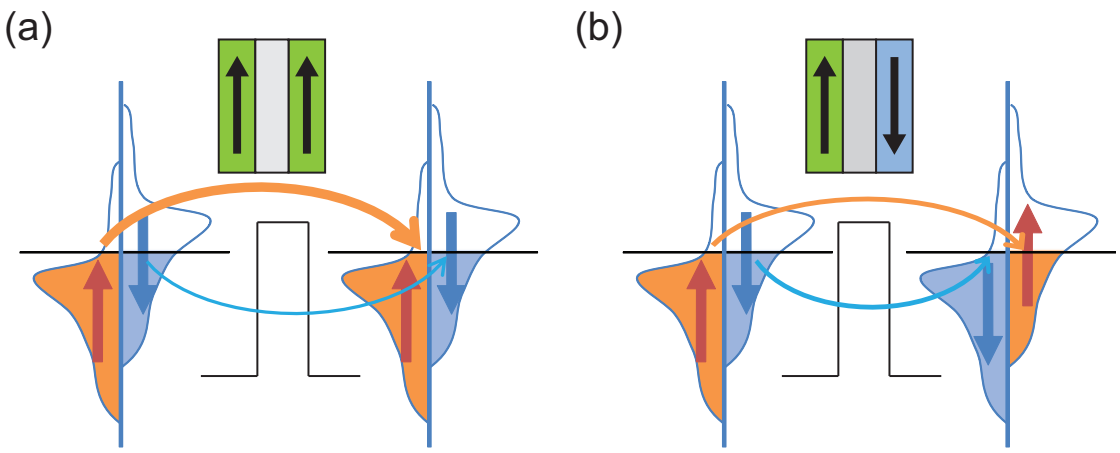

Figure 1.3: Spin dependent tunneling across the tunnel barrier for (a) parrallel configuration of two ferromagnet and (b) anti-parrallel configuration.

final states. Then we have

$$G_P \propto \rho_{L\uparrow}\rho_{R\uparrow} + \rho_{L\downarrow}\rho_{R\downarrow} \tag{1.2}$$

$$G_{AP} \propto \rho_{L\uparrow}\rho_{R\downarrow} + \rho_{L\downarrow}\rho_{R\uparrow} \tag{1.3}$$

where G_P (G_{AP}) is the parallel (anti-parallel) conductance, $\rho_{L\uparrow}$ and $\rho_{L\downarrow}$ ($\rho_{R\uparrow}$ and $\rho_{R\downarrow}$) are the densities of states for up and down spins of the left (right) ferromagnet. By definition, the spin polarization P is

$$P = \frac{\rho_\uparrow - \rho_\downarrow}{\rho_\uparrow + \rho_\downarrow} \tag{1.4}$$

Therefore the tunnel magnetoresistance ratio can be calculated as

$$TMR = \frac{R_{AP} - R_P}{R_P} = \frac{G_P - G_{AP}}{G_{AP}} = \frac{2P_L P_R}{1 - P_L P_R} \tag{1.5}$$

Unlike in the GMR structure where the spin dependent transport only contributes a small part to the total resistance, spin dependent tunneling has a dominating effect in TMR structure so that the TMR ratio can be much larger than GMR. In early studies of MTJs, a TMR ratio of a few 10's of percent was achieved with amorphous aluminum oxide (AlO) barriers. More recently, single

crystalline magnesium oxide (MgO) barriers were predicted to provide a much higher TMR ratio due to the wavefunction match between the ferromagnetic electrodes and the tunnel barrier. [5, 6] TMR ratios of around 200% were then demonstrated [7, 8] and led to intensive studies in MgO based MTJs. Today TMR values of 600% at room temperature and over 1000% at 4.2 K have been observed in CoFeB/MgO/CoFeB junctions. [9]

1.4 Spin Transfer Torque

In GMR and TMR structures, the ferromagnetic electrodes influence the transport property of the spin polarized electrons via their magnetization. On the other hand, the spin polarized electrons also have an effect on the ferromagnets, that is, they can apply a torque on the ferromagnets via transfer of angular momentum. This torque can be strong enough to reverse the magnetization of the nanomagnet or excite persistent precession of the magnetic moment. This "Spin Transfer Torque" effect was first predicted by Slonczewski [10] and Berger [11] in 1996. Direct experimental observations of spin-transfer-induced magnetic reversal were made in 1999 [12, 13] and first measurement of steady-state magnetic precession was done in 2003 [14], both at Cornell. The spin transfer effect provides an efficient way to manipulate the magnetic moment of a nanoscale magnet, which not only generates much interest in its technological applications, but also enables new kinds of studies of magnetic dynamics. A recent review of spin transfer torque can be found in [15].

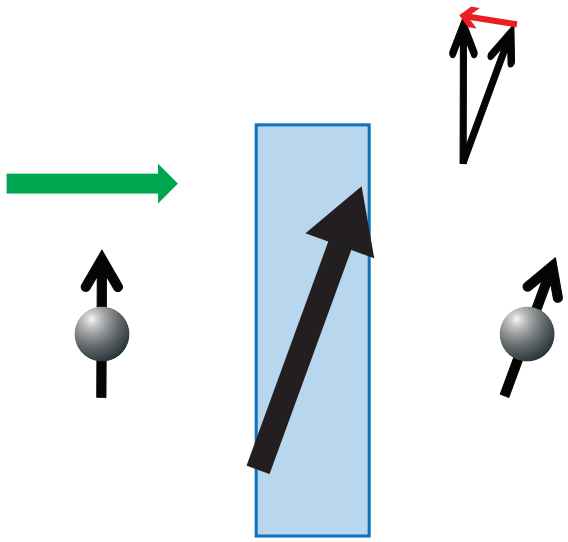

Figure 1.4: Illustration of the transfer of angular momentum when a spin polarized electron passes through a non-collinear ferromagnet.

1.4.1 A Cartoon Picture for Spin Transfer Torque

The spin transfer effect can be explained in a cartoon picture shown in Fig. 1.4. Consider a spin polarized electron entering a ferromagnet whose magnetization is in a direction non-collinear to the electron spin. When the electron passes through, as we have discussed in the GMR effect, the ferromagnet polarizes the electron spin so that the outgoing electron has its spin in the same direction as the ferromagnet. If we then analyze the electron spin before and after, we will notice that there is a net change in its angular momentum, shown as the red arrow in Fig. 1.4. Due to the conservation of angular momentum, this component must be absorbed by the ferromagnet as it repolarizes the electron, and therefore a torque is applied on the ferromagnet by the electron. This seems to be a small effect, since the maximum angular momentum one electron can transfer is only $\hbar/2$. However as many electrons add together, for a small enough magnet, we can apply a reasonable amount of current to achieve a torque strong enough to re-orient the direction of its magnetization.

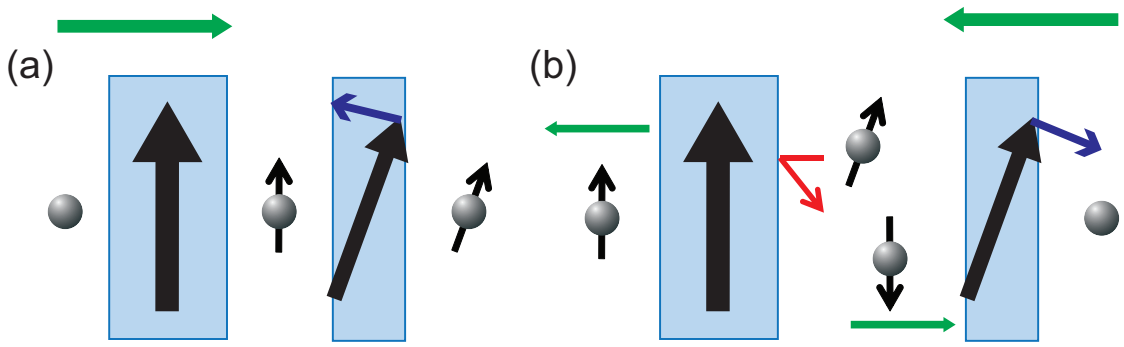

Figure 1.5: Direction of the torque on the free layer depends on the direction of the current.

In a GMR or TMR structure of ferromagnet / spacer / ferromagnet, one of the ferromagnetic layers is usually made thicker or kept fixed by exchange bias so that this layer (the fixed layer) is less susceptible to spin torque and mainly serves as a polarizer to provide spin polarization. The other layer (the free layer) is usually thin and can be excited by spin torque. Figure 1.5 illustrated the dependence of the spin torque on the direction of the current. When electrons flow from the fixed layer to the free layer, electrons are first polarized by the fixed layer, and then apply a torque on the free layer that rotate it toward the fixed layer direction. If current direction is reversed, the direction of torque on free layer is also reversed since now we need to analyze the electrons reflecting back from the fixed layer which have opposite spins as they enter the free layer compared to the previous case. The torque on the free layer now favors anti-parallel configuration of the two layers. So by controlling the current direction, we can control the direction of the spin torque, in favor of either parallel or anti-parallel configuration, providing an efficient way to manipulate the magnetic moment of a ferromagnet.

The above picture is only an intuitive cartoon for purpose of illustration. To calculate the quantitative behavior of spin torque, one needs account for many

realistic factors, for example, the detailed electronic structure of the material, whether the spin transport process is through diffusive or ballistic transport, etc. More detailed discussion can be found in the review paper [15] and references therein. One simple form for spin torque in a symmetric ferromagnet / metallic spacer / ferromagnet structure was given by Slonczewski [16]:

$$\frac{\mathrm{d}\hat{\mathbf{M}}}{\mathrm{d}t} = g(\theta)\frac{\gamma\hbar I}{eV_{free}M_s}\hat{\mathbf{M}} \times (\hat{\mathbf{M}} \times \hat{\mathbf{M}}_{fix}) \tag{1.6}$$

where $\hat{\mathbf{M}}$ and $\hat{\mathbf{M}}_{fix}$ are unit vectors for the magnetization of the two ferromagnetic layers, γ is the gyromagnetic ratio, $\hbar$ is the reduced Planck constant, I is the current, e is the electron charge, V_{free} is the volume of the free layer, M_s is the saturation magnetization of the free layer, and $g(\theta)$ is the unitless spin transfer efficiency. It has the form

$$g(\theta) = \frac{A}{1 + B\cos(\theta)} \tag{1.7}$$

where A and B depend on details of the layer structure.

As indicated by Eq. 1.6, the direction of the torque is confined to be in the plane defined by the two ferromagnetic moments, perpendicular to the free layer direction, and pointing either toward or away from the fixed layer moment depending on the sign of the current. This behavior is generally true for all metallic devices, while in magnetic tunnel junctions, there is also a component perpendicular to the plane defined by the two moments and it has a nonlinear dependence on the bias applied across the tunnel barrier. [17–21] Nonetheless, Eq. 1.6 is good enough to describe the general effects of spin transfer torque and I will only use this form for the rest of the introduction.

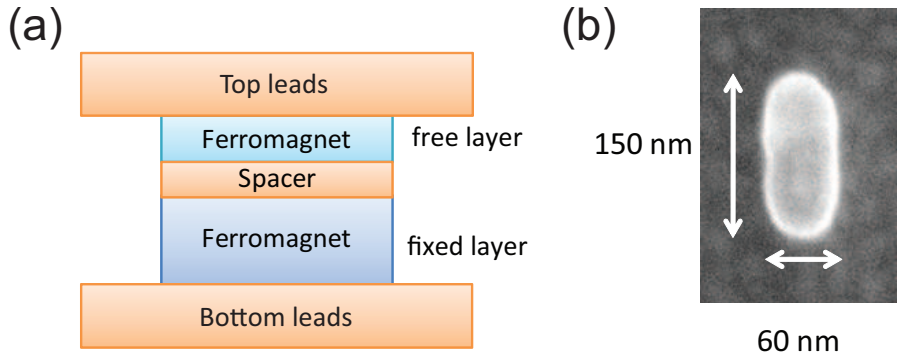

Figure 1.6: (a) Structure of a nanopillar device. (b) SEM image of the elliptical shape of the nanopillar.

1.4.2 Magnetic Dynamics in a Nanomagnet

The device we study typically has a structure of two ferromagnetic layers separated by a spacer. The multilayers are patterned into a elliptically-shaped nanopillar with size typically around 100 nm. (See Fig. 1.6) The top and bottom of the devices are connected to electrical leads to allow current to pass perpendicularly through the multilayers.

In each of the ferromagnetic layers, the magnetic moments of individual atoms are strongly coupled together via exchange coupling. The result is that these magnetic moments will tend to move together and the variations among different moments can usually be ignored on such a small length scale. So we can substitute all the magnetic moments with a single moment or a "macrospin". This macrospin picture makes the analysis much easier and is quite good in explaining many behaviors of the magnetic dynamics in the nanomagnet.

In the thin elliptical-shaped magnetic free layer made of typical ferromagnetic materials such as Ni/Fe alloy or Co/Fe alloy, the magnetic easy axis is

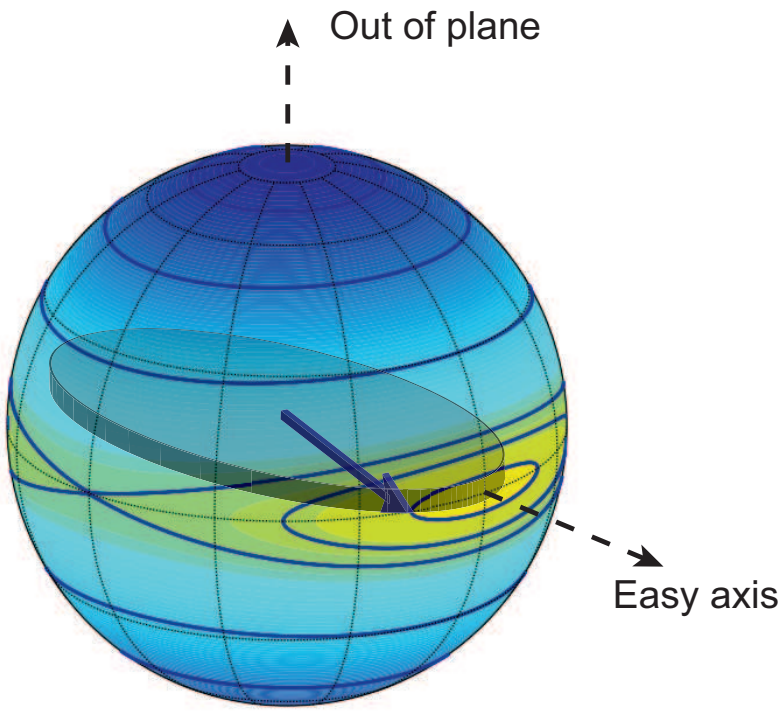

Figure 1.7: Magnetic energy contour of a nanomagnet.

along the the long axis direction of the ellipse due to shape anisotropy.[1] Without any external field, the magnetization of the free layer will lie in the energy minimum direction which is along the easy axis and can point to either end of the device. A detailed magnetic energy contour at zero external field can be calculated within the macrospin model and is shown in Fig. 1.7. Away from the magnetic easy axis, the energy contour has an elliptical shape due to the strong demagnetization field in the out-of-plane direction. Therefore when the magnetization is excited, it will follow these energy contours and precess around the easy axis.

The dynamics of the magnetization in the presence of spin transfer can be described by the classical Laudau-Lifshitz-Gilbert (LLG) equation including an

[1]The magnetic crystalline anisotropy in these materials is usually small and can be ignored.

additional term for the spin torque:

$$\frac{d\hat{\mathbf{M}}}{dt} = -\gamma\hat{\mathbf{M}} \times \mathbf{H}_{eff} + \alpha\hat{\mathbf{M}} \times \frac{d\hat{\mathbf{M}}}{dt} + g(\theta)\frac{\gamma\hbar I}{eV_{free}M_s}\hat{\mathbf{M}} \times (\hat{\mathbf{M}} \times \hat{\mathbf{M}}_{fix}) \qquad (1.8)$$

where $\mathbf{H}_{eff}$ is the total effective field including the applied field $\mathbf{H}_{applied}$ and the anisotropy field $\mathbf{H}_{anis}$, and α is the damping constant. The first term is the field torque term (τ_H) which makes the magnetization precess around the effective field direction, as illustrated in Fig. 1.8. The second term is the damping torque ($\tau_{damping}$) which characterizes the energy dissipation. On average it points toward the equilibrium position of the magnetization, so that without any excitation the magnetization will relax back to the equilibrium. The third term is the spin transfer torque (τ_{ST}). As discussed previously, the direction of this torque depends on the direction of the electron flow. For electron flow from the fixed layer to the free layer, this torque is in the same direction as the damping torque assuming the fixed layer also along the effective field direction, so that it works with the damping torque to accelerate the relaxation of the magnetization. For electron flow from the free layer to the fixed layer, this torque works against the damping torque and thus can reduce the relaxation or even excite dynamics of the magnetization depending on its strength relative to the damping torque.

Usually the spin transfer torque is small compared to the field torque. So the effects of spin transfer torque can be viewed as either increasing or decreasing the amplitude of the magnetic precession. In general the magnetic dynamics excited by spin transfer torque can be categorized into two types: switching and persistent precession.

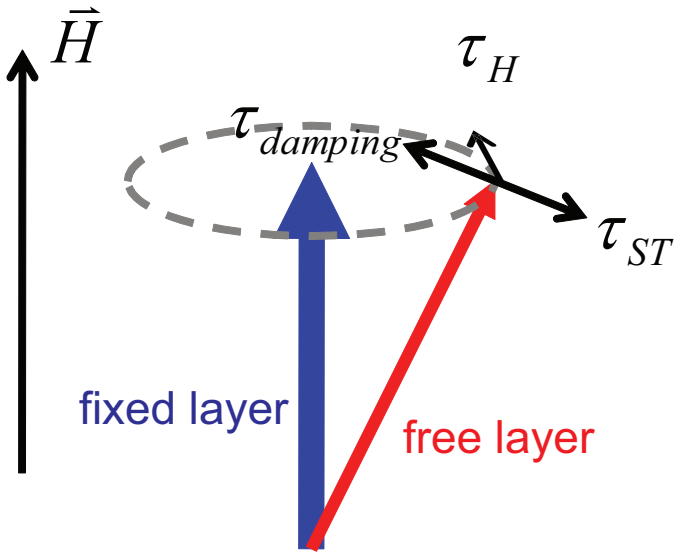

Figure 1.8: Directions of the field torque τ_H, the damping torque $\tau_{damping}$, and the spin transfer torque τ_{ST}.

1.4.3 Magnetic Switching

At zero or small fields, both directions along the easy axis correspond to local energy minimums so it is possible to switch the magnetization between these two directions with spin transfer torque. For example, for a device with both free and fixed layers staying in the easy axis direction and parallel to each other, if we flow a positive current defined as electron flow from free to fixed layer, according to previous analysis, the spin torque acting on the free layer points away from the fixed layer and destabilizes this configuration so that the magnetic moment of the free layer goes into a precession around the easy axis. When the current increases, the amplitude of the free layer precession increases until it reaches the energy barrier which is around 90°. After that, the damping torque changes its direction and points toward the other local energy minimum. Now the spin torque and the damping torque are in the same direction, and the free layer relaxes to that energy minimum corresponding to anti-parallel

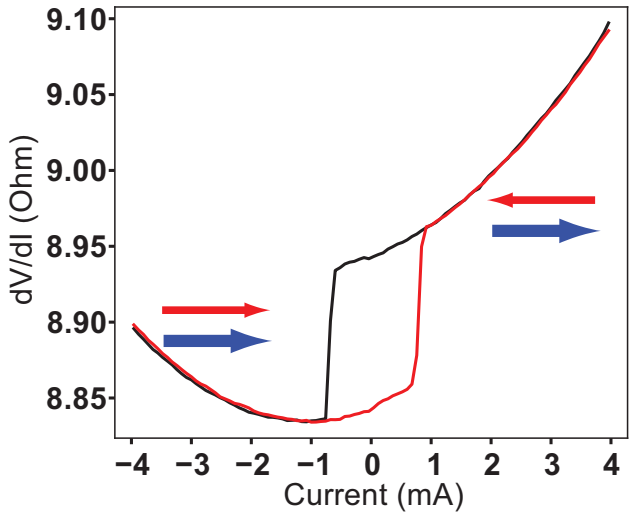

Figure 1.9: Hysteresis loop of resistance as a function of current.

alignment relative to the fixed layer. Similarly, starting in the anti-parallel configuration, a strong enough negative current can switch the free layer back to the parallel configuration. If we monitor the resistance of the device, it will exhibit a hysteresis loop as we sweep the current, as shown in the example scan in Fig. 1.9.

The current required to achieve switching at zero temperature (no thermal excitations) is defined as the critical switching current I_c. Above I_c, the spin torque is stronger than the damping torque and drives the free layer moment to switch direction. Figure 1.10 is a simulation example of a switching event. The switching proceeds via a precessional motion of the magnetization with increasing amplitude. Since the precession frequency is in the range of GHz, the switching can be a very fast process and typically finishes within a few nanoseconds. The switching time has a dependence on current in the form [22]

$$t_s \propto \frac{1}{I - I_c}. \tag{1.9}$$

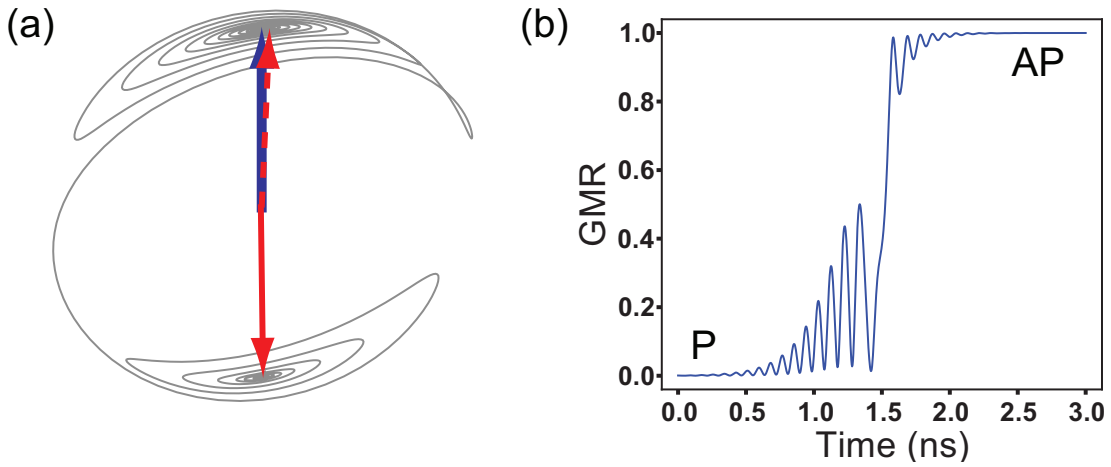

Figure 1.10: An example of a simulated spin transfer switching event. (a) Trajectory of the switching. Red arrows indicates the direction of the free layer before (dotted line) and after (solid line) switching. Blue arrow indicates the direction of the fixed layer. (b) Corresponding normalized GMR as a function of time.

When the applied current is less than I_c, the spin torque cannot drive the free layer moment to directly cross the energy barrier to achieve switching. Instead, it can only excite magnetic precession at small amplitudes. However, switching can still occur in this situation at finite temperatures due to thermal excitations. This is simply a thermal activation process. Disregarding spin transfer effect, thermally assisted magnetization reversal has been studied for a long time. The switching probability $P(t)$ can be described by the Neel-Brown relaxation time formula [23]

$$P(t) = 1 - \exp(-t/\tau) \tag{1.10}$$

where t is the observation time, and τ is the relaxation time. τ is given by

$$\tau = \frac{1}{f_0} \exp(E_b/k_B T) \tag{1.11}$$

where f_0 is the attempt frequency, E_b is the energy barrier, and T is the temperature. The effect of spin transfer on the thermally excited magnetic switching has also been studied in a number of experiments [22, 24–28].

Theoretical calculations [29, 30] suggest that the thermal fluctuations can be modeled by a fluctuating field with a Gaussian stochastic process. Then by solving the stochastic LLG equation including the fluctuating thermal field and its corresponding Fokker-Planck equation, they found that the form for the relaxation time τ can be modified as the following

$$\tau = \frac{1}{f_0} \exp\left[\frac{E_b}{k_B T}(1 - \frac{I}{I_c})\right]. \quad (1.12)$$

Therefore the effect of spin transfer torque can be viewed equivalently as introducing either an effective energy barrier $E_b^* = E_b(1 - I/I_c)$ or an effective temperature $T^* = T/(1 - I/I_c)$.

Above and below I_c, the switching time has very different dependences on the applied current (Eq. 1.9 and Eq. 1.12). In order to achieve a very short switching time, a large current is required. This presents a problem for ST-MRAM applications. Many strategies have been pursued to improve the performance of spin transfer switching. These include: reducing the switching current by using large-aspect-ratio elliptical shape to reduce the volume of the free layer while maintaining thermal stability [31] or by partially canceling the free layer demagnetization field [32], increasing the switching speed by using a perpendicular polarizer to achieve out-of-plane precessional switching [33, 34], and maintaining thermal stability by using perpendicularly magnetized materials [35]. In Chapter 2, I will describe our effort to improve the switching performance by resonantly exciting switching with the assistance of a microwave current pulse.

Another related topic is to develop techniques to characterize the magnetic switching process driven by the spin torque, especially on the ultrafast time scale down to below 1 ns. One technique is to study statistically the switching

induced by nanosecond current pulses. [31, 36–38] In this type of measurement, the device is excited by a nanosecond current pulse many times and the switching probability is measured. This technique is useful in determining the value of the critical current and its dependence on various experimental conditions and material parameters. However, it does not provide much information about the magnetic dynamics during switching. Another technique is to directly measure the switching in the time domain. [22, 39–43] During the switching process, the precession of the free layer induces a resistance oscillation which is, at the same time, converted to a voltage oscillation by the applied current bias. This oscillating voltage signal can then be recorded by an oscilloscope. For metallic spin valves, this voltage signal scale is very small due to the small GMR ratios. Therefore, to achieve enough signal-to-noise ratio requires averaging over many switching events. [22, 39, 40] However due to thermal fluctuations, the switching is not a repeatable process so that most of the oscillation signal is washed out after averaging. In magnetic tunnel junctions, the large TMR ratio makes it possible to study the switching with single-shot technique on an event-to-event basis. [41–43] In Chapter 3, I will discuss a technique we developed to enhance the signal-to-noise ratio in single-shot measurements so that we were able to directly resolve the pre-switching magnetic dynamics.

1.4.4 Persistent Magnetic Precession

DC-driven Precession

The other type of dynamics that can be excited by spin transfer torque occurs when a large magnetic field is applied on the sample. In this case, the energy profile of the free layer is changed and there is only one local energy minimum which is along the magnetic field direction. Now if a positive current is applied to the sample, the spin torque can drive the free layer away from the energy minimum. Since there is no other stationary equilibrium state, the free layer will remain in a dynamic state - it will precess steadily around the field direction, as shown in Fig. 1.11. During one cycle of precession, the spin torque cancels out the damping torque on average so that the precession reaches a steady state. This steady-state precession produces a resistance oscillation and hence a voltage oscillation in the microwave frequency range. The frequency can be tuned by the applied field and the applied current. These features allow spin transfer devices to be used as nanoscale microwave oscillators with tunable frequencies.

The first direct experimental observation of spin-transfer-driven persistent precession was made at Cornell in 2003 by measuring the microwave signal with a spectrum analyzer [14]. It can also be measured directly in the time domain [39, 44]. One important issue regarding spin-transfer based nano-oscillators are the coherence time. Long coherence time means narrow linewidth in the power spectrum, and this is desirable for nano-oscillator applications. A lot of efforts have been made in trying to understanding the mechanisms limiting the linewidth of spin-transfer-driven oscillations. In spin

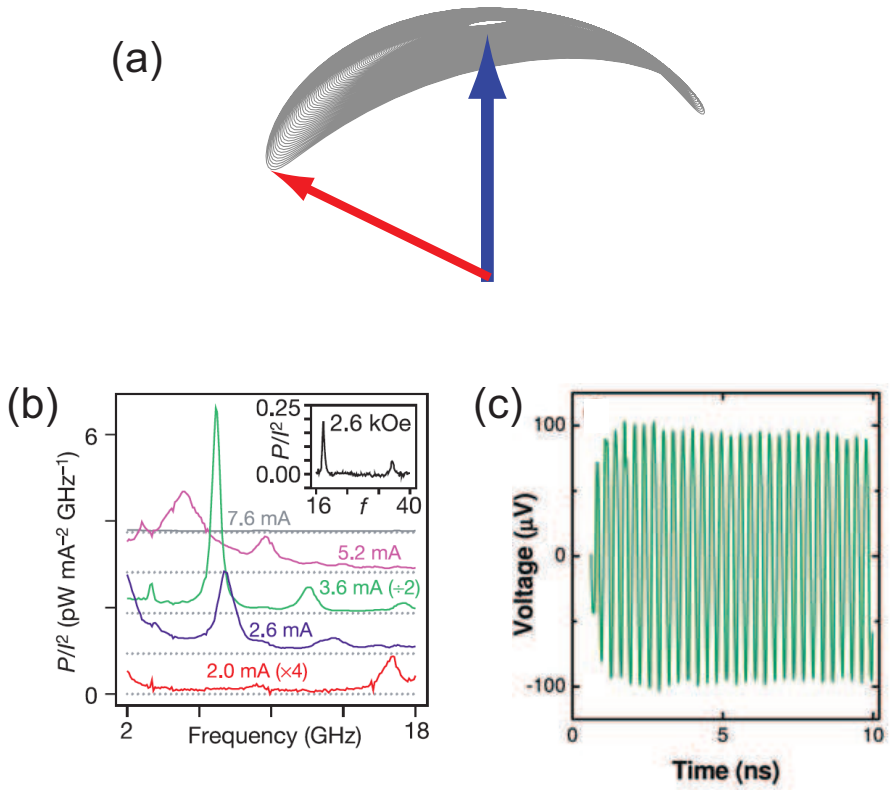

Figure 1.11: Illustration of persistent magnetic precession. (a) Trajectory of a simulated persistent precession. (b, c) Characterization of the persistent precession in (b) frequency domain (modified from [14]) and (c) time domain (modified from [39]).

valve structures, experiments have been made to study the dependence of linewidth on temperature [45], on the excitation of the fixed layer dynamics [46], on the in-plane angle of the magnetic field [47], and on the switching between different dynamic modes [44]. Non-uniform magnetic structures such as magnetic point contact devices [48, 49] and magnetic vortex devices [50, 51] have also been studied and have achieved much narrower linewidths than in spin valves.

Another important issue is the output power. Since GMR ratios are small, the output power from spin valve devices is also quite small. Recent studies have demonstrated that microwave oscillation emitted from MTJ devices can

have much higher power [52, 53]. The linewidth behavior in MTJ devices has also been studied [54, 55]. Another strategy to increase power output is mutual phase locking between nano-oscillators [56, 57] so that the microwave oscillations from different devices can coherently add up to give a larger signal.

Spin-Transfer Ferromagnetic Resonance

Besides the DC-driven persistent precession, an AC current can also excite magnetic dynamics in a resonant fashion. The AC-excited magnetic precession can be detected by measuring a DC voltage resulting from mixing between the resistance oscillation and the AC current drive. This Spin-Transfer Ferromagnetic Resonance (ST-FMR) technique [58–61] is similar to the traditional ferromagnetic resonance, but can be performed in much smaller samples. It can characterize important material properties such as magnetic damping. [59, 62] It can also directly measure the strength of the spin transfer torque, and, particularly, in magnetic tunnel junctions, it can provide quantitative measurements of the spin torque vector and its bias dependence [18–20], which is very important in understanding the spin dependent tunneling process and characterizing and optimizing the MTJs for applications. Furthermore, it can also provide information about the magnetic modes observed in the DC-driven dynamics measurements. [59] In Chapter 4, I will describe how we can use ST-FMR to isolate individual magnetic normal modes and perform X-ray microscopy measurements to study the spatial structure of the normal modes.

1.4.5 Micromagnetic Behavior of Magnetic Dynamics

In this last part of the introduction, I would like to briefly discuss the micromagnetic behavior of magnetic dynamics. (For a recent review on this topic, see [63].) As discussed previously, in the analysis of magnetic dynamics, the simplest macrospin model assumes all the magnetic moments in the ferromagnetic layer respond in the same way and treat them as a single spin. This model was quite successful in analyzing many spin transfer experiments and can often provide qualitative and even quantitative agreement. For example, the phase diagram of spin-transfer-driven dynamics [14] and the frequency and linewidth behaviors of the primary modes in DC-driven dynamics [14, 45] and ST-FMR [59] spectra can be well explained by macrospin calculations. This is mostly due to the fact that the magnetic layers in most spin transfer devices studied have dimensions comparable to or smaller than the widths of magnetic domain walls or the wavelengths of spin wave excitations so that the variations among different moments are small and can be ignored. [63]

However, in many experiments (for example, [18, 46, 47, 59]), some behaviors of the dynamic modes cannot be explained with a macrospin model and likely correspond to non-uniform micromagnetic modes. The non-uniformity of the dynamics can be due to a few factors. First, the size of the sample is not small enough so that there is competition between the spatially uniform and non-uniform modes. Second, the Oersted field generated by the current is not uniform inside the device. This results in different local field environments for different magnetic moments. In magnetic tunnel junctions, the current distribution can also be quite non-uniform because the conductance is very sensitive to the local magnetic configuration of the electrodes. Furthermore,

thermal fluctuations can excite multiple modes when the non-uniform modes are close to the uniform mode in energy.

Studies on micromagnetics have mostly been done through numerical calculations. In the modeling, the ferromagnetic layers are divided into many discrete finite size cells. Within each cell, the magnetic dynamics can be assumed to be uniform and can be described by a LLG equation. The variations in the local field and current are taken into account in each of the LLG equations. These LLG equations are coupled together and can be solved numerically. With appropriate parameters, micromagnetic modeling can provide full descriptions for the magnetic dynamics, though it is usually time consuming and computation demanding. Micromagnetic simulations have been able to explain many experimental observations that could not be explained with macrospin model. (For example, see [63] and references therein)

On the other hand, however, direct characterization of the non-uniform micromagnetic modes has been difficult due to the lack of experimental techniques capable of probing spatially and temporally the magnetic dynamics in spin transfer devices. X-ray microscopy is a promising tool, and initial efforts have been made to image the switching process driven by spin transfer torque. [64–67] I will return to this discussion in Chapter 4 and also describe our on-going (at the time of this dissertation) experiments to image the spin-transfer-driven magnetic normal modes with X-ray microscopy.

CHAPTER 2

RESONANT SPIN-TRANSFER-DRIVEN SWITCHING OF NANOPILLAR DEVICES ASSISTED BY MICROWAVE CURRENT PULSES

2.1 Introduction

As discussed in the introduction chapter, the spin transfer torque generated from a spin polarized current [10, 11] can be strong enough to reverse the magnetization of a nanomagnet. [13, 68] This provides a promising mechanism for writing information in the next generation of magnetic random access memory (MRAM). Improving switching characteristics is essential to improve device performance. Previous measurements have focused on spin-torque switching driven by DC currents [13, 68] and square current pulses [22, 36, 37]. In this chapter, I will present our measurements showing that spin transfer from a microwave-frequency current pulse can produce a resonant excitation of a nanomagnet and improve switching characteristics in combination with a square current pulse. With the assistance of a microwave-frequency pulse, the switching time is reduced and achieves a narrower distribution than when driven by a square current pulse alone, and this can permit significant reductions in the integrated power required for switching. Resonantly excited switching may also enable alternative, more compact MRAM circuit architectures. The contents of this chapter are adapted from work originally published as *Phys. Rev. B* **77**, 214440 (2008).

2.2 Motivation: Benefits From Resonant Excitation

The idea of using a microwave current to enhance switching comes from the understanding established by previous experiments that the spin-torque switching in a nanomagnet proceeds via a process of magnetic precession with increasing precession amplitude. [39, 44, 69, 70] Spin-transfer ferromagnetic resonance experiments have shown that an radio-frequency (RF) current can drive magnetic precession resonantly. [58, 59] For resonant excitations, it is possible to excite large amplitude precession with only a small driving force at the resonant frequency. This suggests that a microwave current on resonance might improve the switching characteristics of spin-torque devices. [71–73]

I want to note that, in magnetic recording community, microwave assisted magnetic recording (MAMR) has been actively pursued in recent years. [74] In this technique, a microwave magnetic field is applied to the storage media which produces magnetic precession of the storage bits. This then reduces the energy barrier required to achieve switching by conventional writing mechanism. In spin-torque devices, writing of information is achieved by applying a current. Therefore it is more convenient to use a microwave current than a microwave field to achieve similar benefits. Plus, generation of a localized microwave field[1] might require more complicated circuitry than generation of a microwave current.

[1] In fact, in MAMR technique, a spin-torque oscillator is used to generate such field.

2.2.1 Spin-transfer Switching in Collinear and Non-collinear Devices

The effects of microwave current on the switching process depend on the structure of the device, in particular, the relative orientation of the free and fixed layers in nanopillar devices. Collinear devices, where the free and fixed layers have an approximately collinear alignment, i.e., close to either parallel or antiparallel alignment, have been mostly studied in the initial experiments on spin-torque switching. [22, 36, 37] Since the spin torque vanishes at zero offset angle, spin-transfer switching in such devices requires that the moments have an initial deviation from completely parallel or anti-parallel alignment. This is usually initiated by thermal fluctuations. Therefore, the switching process is stochastic, with a broadened distribution of switching times. An alternative strategy is to use non-collinear devices, where there is a non-zero equilibrium angle between the two moments by biasing one of the two layers away from the easy axis defined by shape anisotropy. [39, 75–77] However, in this case using a square-wave current pulse (with a single sign of current) to drive switching may not provide optimum efficiency. As illustrated in Fig. 2.1(a), consider the initial stage of the switching process in a thin film nanopillar device, where the precession amplitude of the free-layer moment is less than the offset angle between the two moments. For positive currents (by our convention) the spin torque acts to push the free layer moment away from the pinned moment. This means that in one half of the precession cycle the spin torque from a square current pulse works to increase the precession amplitude, but in the other half of the cycle it acts to decrease the amplitude. In contrast, the alternating signs of torque from an RF current at the precession frequency can act always in the

direction to increase the precession amplitude throughout the entire precession cycle. [See Fig. 2.1(b)] Therefore, RF excitation can be expected to be more efficient than square current pulses for small precession angles in this geometry. After the precession amplitude has grown to exceed the offset angle, a square pulse will be preferred since its torque is then in the right direction to enhance precession throughout the whole precession cycle. In our work, we study the switching process driven by a combination of RF and square current pulses. We use an initial RF pulse to excite the free layer magnetization resonantly, and then we complete the switching with a square current pulse.

2.3 Method

2.3.1 Circuit Setup for Generation of Synchronized RF Pulse

We use the mixing circuit shown in Fig. 2.2 to generate the waveforms for our experiment, which consist of a combination of RF and square-wave current pulses. We are able to control all of the parameters of the waveform, including the RF and square-wave pulse amplitudes, the RF phase, and the relative delay between the RF and square-wave components (within 5 ps).

The RF component of the signal is generated by modulating a continuous-wave (CW) microwave source with a nanosecond-scale pulse from Pulser 1 using a mixer. This method was first developed by Jack Sankey [78]. A CW microwave signal is connected to the RF ("Radio Frequency") port of the mixer. The transmission signal at the LO ("Local Oscillator") port can be gated by a voltage at the IF ("Intermediate Frequency") port. When the IF voltage is zero,

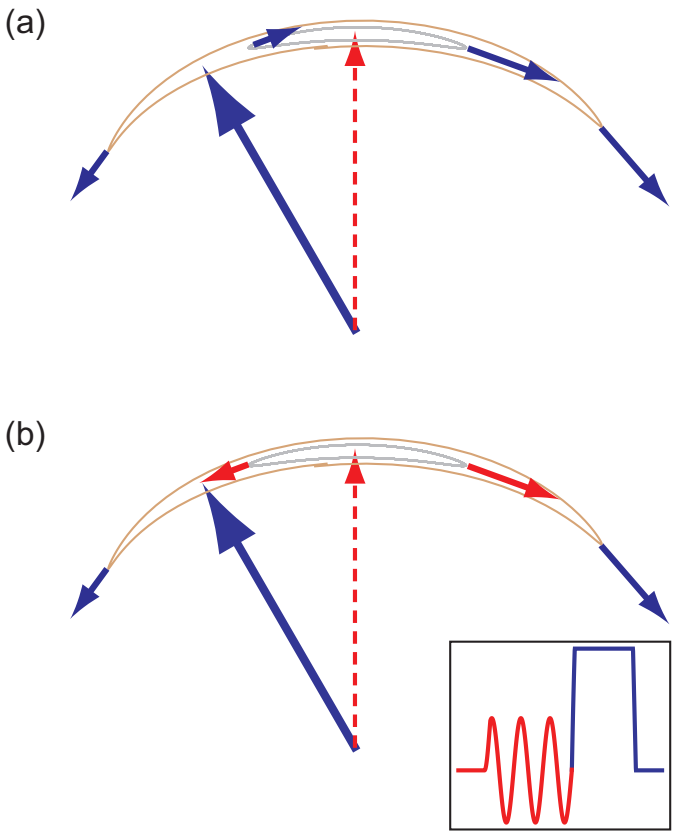

Figure 2.1: Comparison of the effects of the spin torque from a square pulse and a microwave pulse. (a) For a precession amplitude less than the offset angle between the pinned layer moment and the free layer precession axis (smaller trajectory), a DC current produces a spin torque (black arrows) that increases the precession amplitude over half the cycle but decreases it for the other half. Only when the precession amplitude is greater than the offset angle (larger trajectory), will the spin torque from a DC current increase the precession amplitude on both halves of the precession cycle. (b) For a waveform of an RF pulse followed by a DC pulse (inset), the spin torque from the RF current on resonance (red arrows) increases precession amplitude more efficiently for small angle precession throughout the entire cycle.

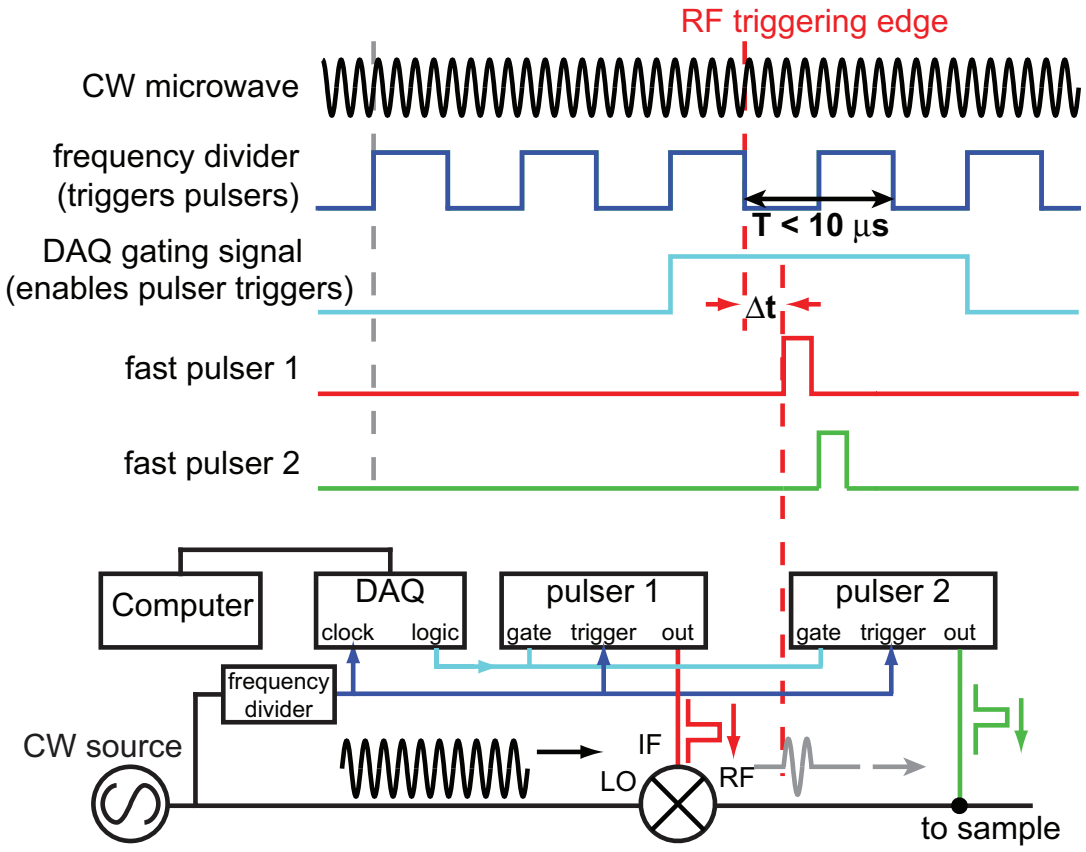

Figure 2.2: Circuit schematic and timing diagram for combining RF and square-wave pulses to make the excitation waveforms.

the LO output is isolated from the RF input; while the IF voltage is non-zero, the CW signal will be transmitted through. Therefore, when a square voltage pulse is applied at the IF port, the transmitted signal will be a chopped CW microwave, i.e., a microwave pulse.

The square pulse is generated by Pulser 2 and added to the RF pulse via a power divider. The combined waveform is then split into two parts using another power divider. One part is directed to a 12.5 GHz oscilloscope for recording the waveform, and the other to the sample through the RF port of a bias-tee.

The challenging part is to achieve a repeatable pulse pattern with controllable pulse parameters. This means that the triggers for the two pulsers must be synchronized to the CW RF signal. The solution is to use the RF signal to directly generate triggers for the pulsers. This can be done by dividing the RF signal frequency f_{RF} down to a slower frequency $f_{trigger}$ by frequency dividers. We use a two-stage frequency division. The first stage is a fixed-division-ratio (20 for the one used in this experiment) frequency divider (made by RF Bay Inc.) which is able to accept input frequency range 0.1~12 GHz and outputs square wave pulses at the divided frequency. This signal is then fed to the second stage frequency divider which is a variable-division divider (made by Pulse Research Labs). This divider can handle input frequency up to 1 GHz and has division ratio from 2 to 4096 set by the pins on the device. Both dividers have nice features that the output square wave pulses are phase synchronized with the input signal. The final output from the second stage divider (TTL standard) has a frequency $f_{trigger} = f_{RF}/M$ where $M = M_1 * M_2$ with M_1 and M_2 the division ratios of the first and second stage dividers. This output can be used to trigger the pulsers. Since we need to measure the resistance of the sample before and after firing the pulse to perform statistical study, we need to programmably control when the pulsers respond to the trigger signal. The gate inputs of the pulsers offer a way to achieve this. We use the DAQ card on the computer to read the TTL trigger signal[2] as a clock for the timing logic, and programmably generate a single pulse with a duration twice long as the period of the clock signal. This single pulse is then sent to the gate inputs of both pulsers. As illustrated in Fig. 2.2, the gate signal is synchronized with the rising edge of the

[2]Note: the TTL trigger signal is sent to the two pulsers first, so its amplitude will drop because of the loads at the trigger inputs. We boost the trigger signal by using a video Op-Amp to reach TTL logic level. The Op-Amp causes some jitter in the amplified trigger signal, but since this signal is used for generating the gating pulse, the timing jitter is not critical.

trigger signal, and spans two trigger periods. To avoid mistriggering, we set the pulsers to trigger off the falling edge of the trigger pulses. The pulsers have a limitation that the minimum response time between two triggers is 10 μs. We actually take advantage of this limitation by generating trigger frequency faster than 100 kHz so that within the same gate signal the pulsers can only fire one pulse at the first trigger edge. This in fact sets the value range for the division ratio M and we typically use M in the range between 8000 and 12000. With this triggering mechanism, we are able to generate a repeatable pulse pattern and trigger it programmably.

Next I will describe how to control the pulse parameters. For the RF pulse, the frequency is determined by the microwave source and thus can be accurately tuned. The RF amplitude depends on both the CW amplitude and the transmission of the mixer for a given IF voltage. For IF voltage greater than ~0.1 V, the mixer transmission reaches a constant. We want to work in this range so that we can control the RF pulse amplitude by only controlling the CW power at the microwave source. So we need to make sure the modulation square pulse from Pulser 1 has a large enough amplitude. The duration and transition time of microwave pulse is determined by the modulation square pulse.[3] Both Pulser 1 and 2 are the same model (Picosecond Pulse Labs 10070A). The pulse duration range is 0.1 - 10 ns in 2.5 ps steps. The rising and falling times are 70 ps and 100 ps respectively. The pulse amplitude range is 0.7 mV to 7.5 V with 1 dB step and is bipolar. These features provide good control of the individual parameters of RF and square pulses. The relative time delay between the RF and square pulses can be controlled in the following way. For coarse tuning, the pulsers can set the pulse delay relative to the trigger edge in the range of 0 - 63 ns with 1 ns step.

[3]For best performance, the IF port of the mixer should have a lower bandwidth down to DC, and upper bandwidth up to GHz to avoid distortion of the modulation pulse.

For fine tuning below 1 ns, we use trigger level function on the pulser. This sets the trigger level between -2 V to 2 V in 1 mV step. Since the TTL trigger signal generated from the frequency dividers has rising and falling times on the order of 1 ns, changing the trigger level by 10's of mV will change the pulse delay by 10's of ps.

Another important parameter is the phase of the RF pulse, ϕ, relative to the onset of the square pulse. It is determined by $\phi = \phi_{trigger} + 2\pi f t$, where $\phi_{trigger}$ is the phase of the RF signal at the time of the triggering edge and t is the time delay between the triggering edge and the moment when the output square pulse arrives at the IF port of the mixer. Since the trigger is synchronized with the CW RF signal, $\phi_{trigger}$ is not tunable. t is determined by the pulser and the length of the transmission cable, and is kept fixed during our experiment. Then we can control ϕ by varying the frequency of the RF signal slightly. In our typical set-up, a frequency change of only 6.4 MHz changes ϕ by 360°. Our resonance linewidths are on the order of 100's of MHz, so we are able to tune ϕ fully using a range of frequency that is negligible compared to the linewidth. The actual phase of each individual waveform is determined by fitting the RF pulse with a chopped sinusoidal function. We define ϕ to be zero when the RF current would be crossing zero in the positive direction at the moment of the initial rise of the square pulse. Our uncertainty in ϕ is determined by a trigger jitter of 5 ps, and corresponds to $\Delta\phi = 9°$ for $f = 4.9$ GHz. Figure 2.3 shows examples of the waveforms for two different values of ϕ, 0° and 180°.

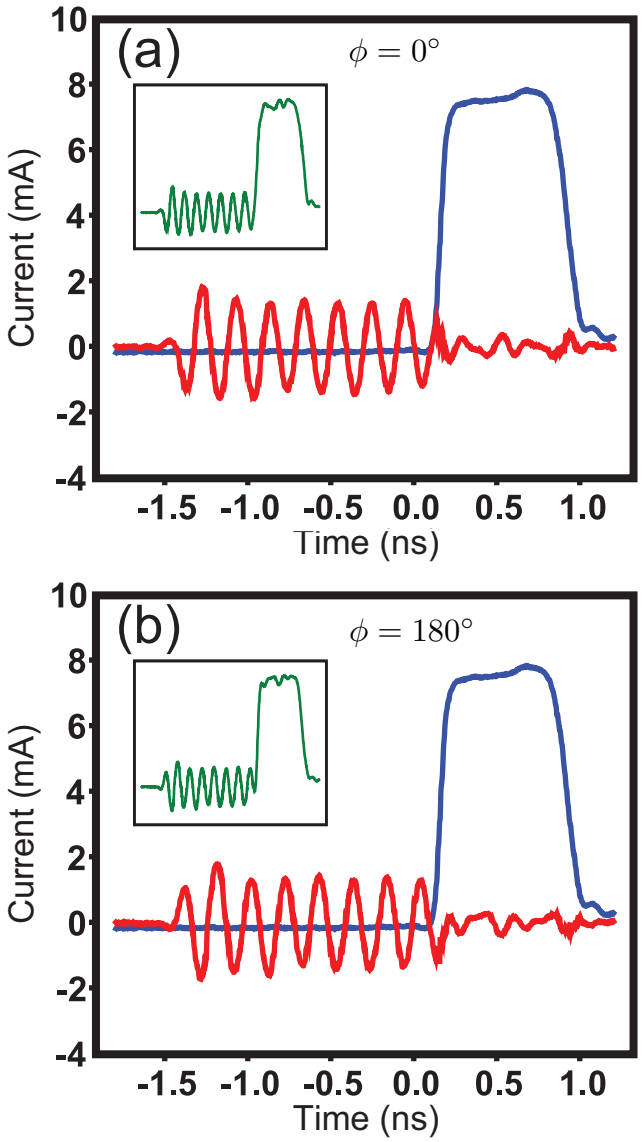

Figure 2.3: Examples of the excitation waveform, which combines RF and square-wave pulses, for (a) $\phi = 0°$ and (b) $\phi = 180°$. ϕ is defined as the phase of the microwave signal at the onset time of the square pulse.

2.3.2 Device Structure

We study exchange-biased spin valve nanopillars with the layer structure (in nm) IrMn 8 / permalloy 4 / Cu 8 / permalloy 4 / Cu 2 / Pt 30, with Cu contacts on top and bottom. Here permalloy (Py) is $Ni_{81}Fe_{19}$. All the layers are etched to have an elliptical cross section of approximately 80×150 nm^2. The long axis of the ellipse is designed to be 45° from the direction of the exchange bias between the IrMn layer and the bottom Py layer (pinned layer). Based on a macrospin-model fit to the curve of magneto-resistance as a function of the magnetic field applied along the exchange bias direction (see Fig. 2.4), we estimate that the actual equilibrium offset angle between the free and pinned layers in the low-resistance (LR) state is 30°. We perform the majority of our measurements at a background temperature of 20 K to reduce thermal fluctuations. We estimate [28] that the samples may heat to $\sim$ 100 K for our largest current pulses, assuming that the heat flow is dominated by electronic conduction to the contacts and that the Weidemann-Franz law is a good approximation. During the switching measurements, a field H_d = 140 Oe is applied along the exchange bias direction to cancel the dipole field from the pinned layer on the free layer, leaving the free layer near zero net magnetic field. We will focus on switching from the LR state to high-resistance (HR) state. (Measurements of HR to LR switching are qualitatively similar.). Extrapolated to zero temperature, the switching current and switching field for LR to HR switching were I_{c0} = 3.2 ± 0.2 mA and $|H_{c0} - H_d|$= 260 Oe. Positive current will correspond to electrons flowing from the free layer to the pinned layer.

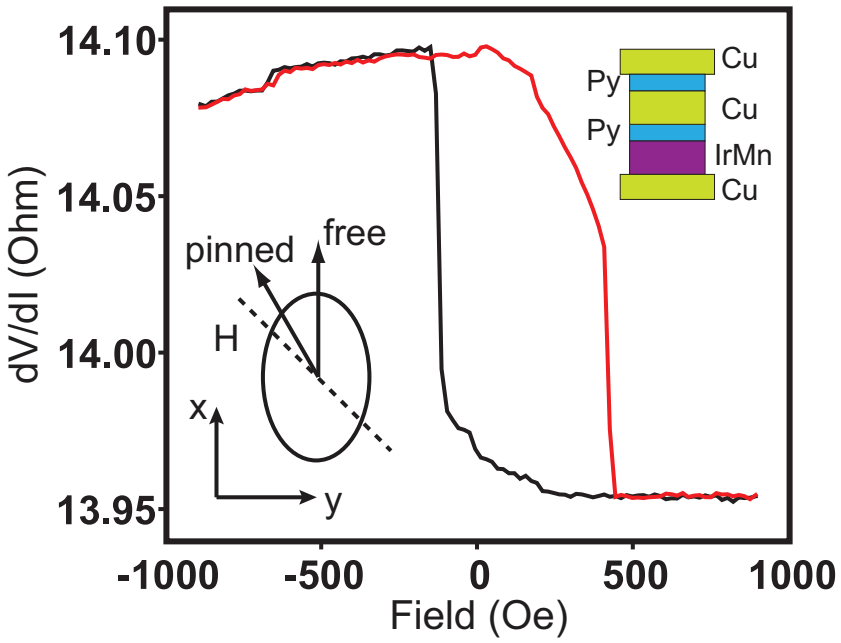

Figure 2.4: Resistance measured as a function of magnetic field applied along the exchange bias direction. Upper right inset: layer structure of the samples. Lower left inset: orientation of the free and pinned layer moments for the low-resistance equilibrium state.

2.3.3 Measurement of Switching Probability

The procedure to measure the probability of switching from the low resistance (LR) state to the high resistance (HR) state is the following. After the reset pulse is applied, we measure the differential resistance of the sample, R_{before}, to check the sample state and make sure that $R_{before} = R_{LR}$. Next, a gating signal from the DAQ computer is generated to enable the triggers on the pulsers, resulting in the generation of the combined RF + square-wave pulse and its transmission to the sample. After this, the differential resistance of the sample, R_{after}, is measured. R_{after} is close to either R_{LR} (not switched) or R_{HR} (switched), and the result is stored. These steps are repeated N times for each set of pulse

parameters. The switching probability is thus calculated as $P = N_{switched}/N$ where $N_{switched}$ is the number of switched events. The uncertainty is determined as $\sigma(P) = \sqrt{P(1-P)/N}$.

2.3.4 Calibration of the Pulse Amplitude

The pulse waveform recorded by the sampling oscilloscope is the voltage coupled to a 50 Ω termination. We need to calibrate this voltage relative to the current coupled into the sample. This calibration is done by measuring the switching probability excited by the combination of a pulse and a steady-state current in the following procedure (see Fig. 2.5). First the switching probability of a 2 ns long square-wave pulse is measured for different pulse amplitudes in the absence of any steady-state current. The switching probability is 0 for small amplitude and increases to 100% as we increase the pulse amplitude. We choose a reference point V_0 where P_0 is close to 50%. Then we decrease the square pulse amplitude to V_1 and apply a small positive steady-state current to the sample (small enough so that it does not excite any magnetic dynamics or shift the equilibrium orientations of the moments significantly), while measuring the switching probability corresponding to this combination of square-wave pulse V_1 and the steady-state current. We adjust the steady-state current, I, until the measured switching probability reaches the reference value, P_0. At this point, the difference between pulse amplitudes V_0 and V_1 is compensated by the applied steady state current, I. The voltage-to-current conversion ratio is therefore $\rho = I/(V_0 - V_1)$. We have checked this calibration relative to the current calculated using the measured microwave impedance of our devices, and they agree to within better than 10%.

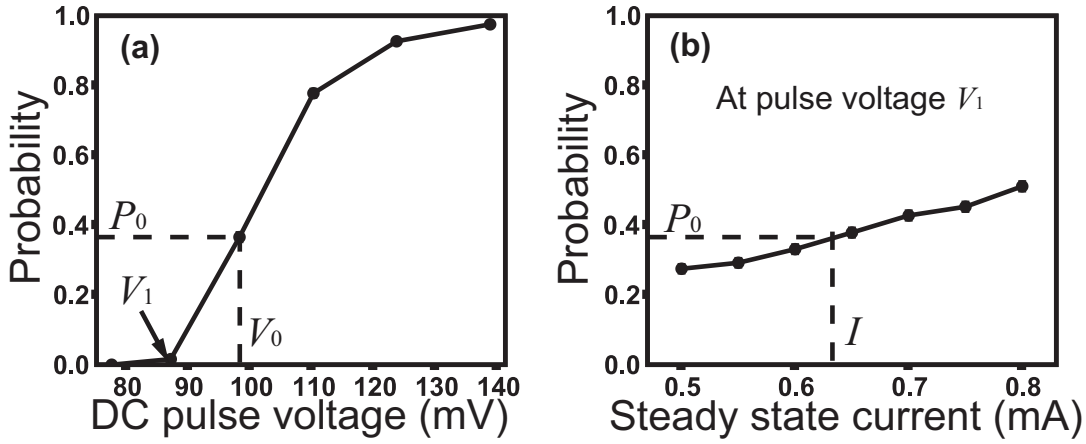

Figure 2.5: Calibration of the pulse amplitude. (a) Switching probability as a function of pulse amplitude. V_0 is chosen as a reference point, with P_0 close to 50%. (b) Switching probability at pulse voltage V_1 as a function of a steady-state background current, I. When I is large enough to return the switching probability to P_0, the steady-state current is equal to the difference in the currents generated at the sample by the pulses V_0 and V_1.

2.4 Measurement and Simulation Results

To study the effect of microwave pulse on the switching characteristics, we employ pulse waveforms similar to those shown in Fig. 2.3, consisting of a combination of RF and square-wave pulse signals chosen so that the switching process can be initiated by a RF pulse and then completed by the square pulse.

2.4.1 Dependence on Frequency and Phase

We begin by considering the regime in which the square pulse is sufficiently large (7.7 mA) and short (0.7 ns) so that thermal effects do not affect the switching trajectory dramatically (smaller, longer square pulses are discussed below). The amplitude of the square pulse is chosen to be just below the critical

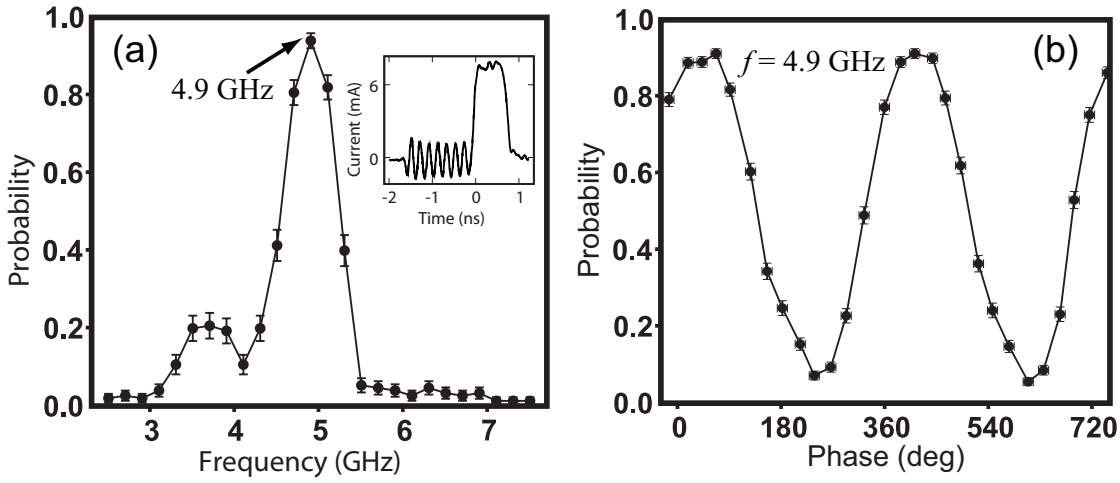

Figure 2.6: Dependence of the switching probability on the microwave frequency and phase. (a) Switching probability as a function of frequency, after optimizing the phase ϕ. RF pulse parameters: 1.4 mA, 1.7 ns; square pulse parameters: 7.7 mA, 0.7 ns. Inset: waveform for f=4.9 GHz and ϕ=50°. (b) Switching probability as a function of the phase ϕ for f = 4.9 GHz, using the same pulse parameters as in a.

value at which the switching probability driven by the 0.7 ns square pulse alone becomes nonzero for this sample. Using a fixed RF peak amplitude (1.4 mA) and length (1.7 ns), we vary the RF frequency f in discrete steps and at each value we vary the relative phase ϕ by more than 360 degrees. Figure 2.6(a) shows the maximum switching probability that can be achieved at each value of f after optimizing ϕ. (For each point we average over 150 identical pulses.) We observe a strong resonant response to the RF pulse, in that the switching probability is enhanced from nearly 0 to over 90% at the resonant frequency f_0 = 4.9 GHz. The switching probability oscillates as a function of ϕ with a period of 360 degrees [Fig. 2.6(b)]. At 4.9 GHz, the switching probability is greatest (92%) at ϕ= 50° and least (6%) at ϕ = 230°. As f is tuned through the resonance, the optimum value of ϕ varies by approximately 180°. In contrast to the strong dependence of the switching probability on the RF phase at the onset of the square pulse (ϕ), there is negligible dependence on the initial phase at the start of the RF pulse.

2.4.2 Enhanced Switching Characteristics Achieved by the RF Pulse

Compared to using square pulse alone, using a combination of RF and square-wave current pulses can enhance the switching characteristics in two aspects: (i) enhanced switching speed and reproducibility of switching times, and (ii) significant reduction of the integrated power required for switching.

Figure 2.7(a) shows the effect of the RF pulse on the experimental distribution of switching probabilities as a function of square pulse duration, for f = 4.9 GHz, $\phi = 50^{\circ}$, and RF pulse parameters of 1.4 mA peak amplitude and 0.3 ns duration prior to the square pulse. Each point corresponds to an average over 500 pulses. Compared to the distribution for no RF component, the length of the square pulse necessary to achieve switching is reduced, and the width of the distribution of switching times is narrowed dramatically, by a factor of 2.6. The length of the square pulse necessary to achieve switching with 95% probability changes from 1.64 ns to 0.93 ns, significantly more than the 0.3 ns duration of the RF pulse. We attribute the narrowing of the distribution to the coherent excitation of precession by the RF pulse, which may mitigate the effects of thermal fluctuations.

The potential for power savings that might be achieved by using resonant RF pulses is illustrated in Fig. 2.7(b). This panel shows two excitation pulses, one with an RF component and one without, which both give identical 95% switching probabilities. The integrated power consumption needed for switching is reduced by 40% when the RF pulse is used.

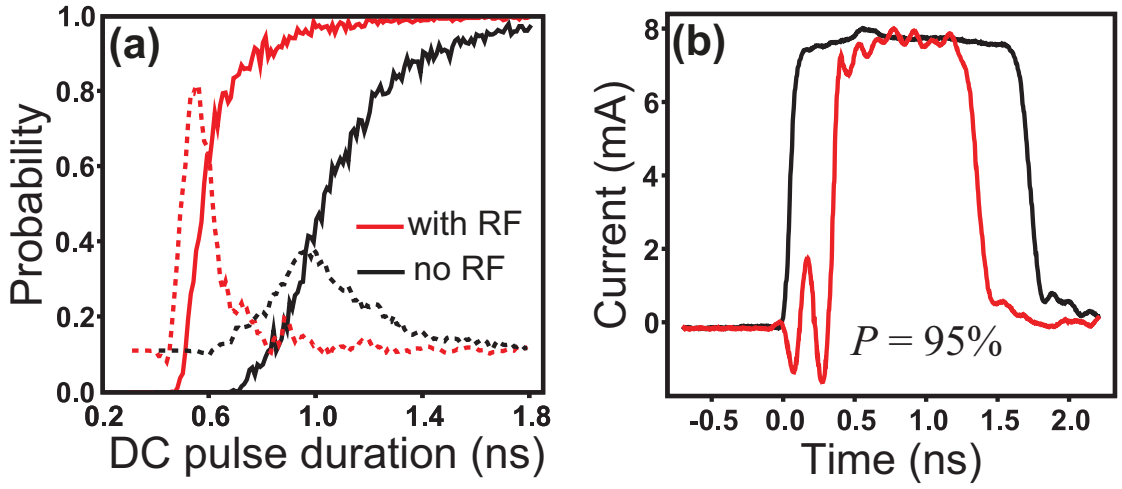

Figure 2.7: Enhancement of magnetic switching using microwave current pulses. (a) Solid lines: switching probability as a function of square pulse duration without a microwave pulse (black/darker curve) and with a 1.4 mA, 0.3 ns, ϕ=50° microwave pulse (red/lighter curve). The square-pulse amplitudes used are both 7.7 mA. Dotted lines: corresponding distributions of switching pulse duration, corresponding to the derivative of the switching probability versus pulse length. (b) Waveforms for two pulses that both give a 95% switching probability in (a).

2.4.3 Understanding the Effect of Microwave Pulse: Macrospin Simulation

In order to visualize how an RF pulse affects the free layer precession, we have performed macrospin simulations including thermal fluctuations corresponding to a temperature of 20 K (Fig. 2.8). An example of the simulated dependence of switching probability on ϕ is shown in Fig. 2.8(a). The simulations suggest that the free-layer magnetization precesses in phase with the RF drive with increasing amplitude. At the end of the RF pulse, the square pulse is applied, producing a torque on the free layer pointing away from the pinned layer moment. For ϕ = 50° [Fig. 2.8(b) and 2.8(c)], the square pulse begins just as the free layer moment enters the half of its precession cycle in which it is farther

from the pinned-layer moment. By the time that the free layer precesses to the extremum position, the current from the square pulse increases to a large value and applies a strong torque to increase the precession amplitude of the free layer. For a sufficiently large precession angle, the spin torque can then act to enhance precession in the whole precession cycle and it can complete the switching in a few cycles. On the other hand for $\phi = 230^\circ$ [Fig. 2.8(d) and 2.8(e)], the free layer is in the half of its precession cycle closer to the pinned-layer moment at the time when square pulse is applied and initially the spin torque acts to decrease the precession amplitude. The result is a decreased switching probability compared to $\phi = 50^\circ$.

2.4.4 Dependence on the RF Pulse Parameters

Next we explore how varying the RF pulse parameters affects the switching probability. We first measure the frequency dependence of switching probability with the same parameters as in Fig. 2.6 except that we use several different values for the amplitude of the RF pulse [Fig. 2.9(a)]. As the RF peak amplitude is increased from 0.7 mA to 1.8 mA, the maximum switching probability at the resonant frequency increases and eventually saturates. In Fig. 2.9(b) we show how the switching probability for $f = 4.9$ GHz depends on the duration of the RF pulse, for each of the RF amplitudes shown in Fig. 2.9(a). In each case, the onset of the square pulse is timed to correspond to the end of the RF pulse. The optimum relative phase ϕ does not change significantly as a function of RF amplitude. For all of the RF amplitudes, we observe that the probability saturates at long RF pulse durations, indicating that the precession amplitude excited by a given RF amplitude also saturates. Larger RF amplitudes give

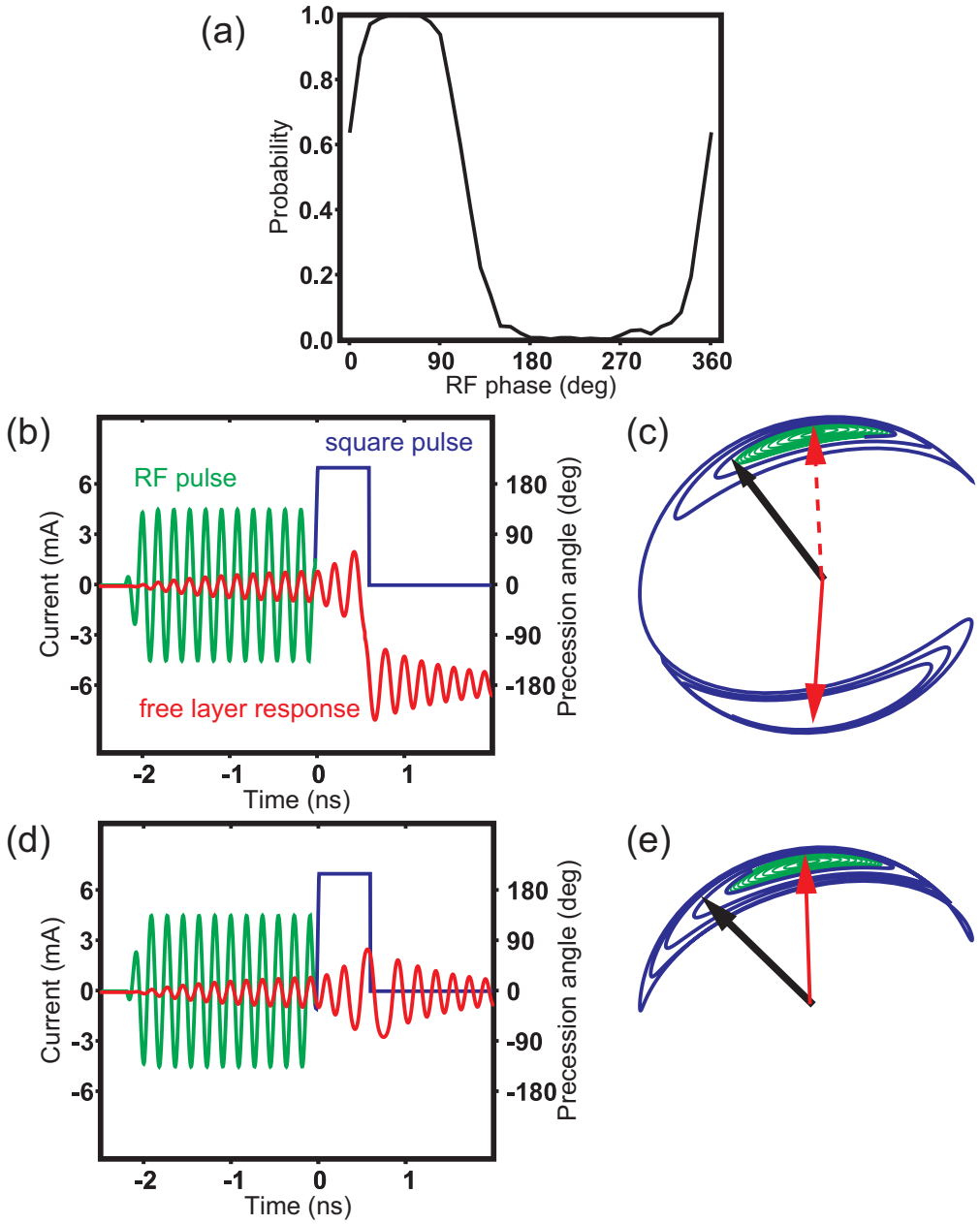

Figure 2.8: Macrospin simulations of resonantly-enhanced spin-torque switching at 20 K. (a) Dependence of the switching probability on the phase ϕ for a 4.5 mA, 2 ns RF pulse with a 7 mA, 0.6 ns square-wave pulse. (b-e) Free layer moment precession in response to the current pulse. (b) $\phi = 50°$. (d) $\phi = 230°$. (c) and (e) are 3D trajectories for (b) and (d). Green parts correspond to RF pulse excitation. Blue parts correspond to square pulse excitation. Red arrows indicate free layer moment. Black arrows indicate fixed layer moment.

higher switching probabilities at saturation and reach saturation for shorter RF pulse durations. For the RF amplitude of 1.8 mA, the switching probability saturates for RF pulse durations as short as 300 ps, corresponding to only 1.5 cycles of RF current.

In Fig. 2.9(c), for a fixed square-wave amplitude of 7.7 mA, we compare the square pulse durations required to achieve 95% switching probability, $T_{0.95}$, as a function of RF amplitude at the resonance frequency (f = 4.9 GHz) for both the optimum relative RF phase (ϕ = 50°) and the least-favorable phase for switching (ϕ = 230°). In all cases, the RF duration (1.7 ns) is long enough to achieve saturation. For the optimized value of ϕ, $T_{0.95}$ for all RF amplitudes is considerably less than for switching driven by a square pulse alone (dashed line). For the least-favorable relative phase ϕ for switching, $T_{0.95}$ is close to the square-pulse-alone value over most of the range of RF amplitude, and for very small RF amplitudes the RF pulse can actually suppress the switching slightly.

These results are in good accord with our macrospin simulations, which indicate that the RF drive causes the precession amplitude to grow with time until the point that the energy gained from spin transfer over one cycle is balanced by the energy lost to damping. Therefore, for small RF amplitudes, the saturation angle for the precession increases with RF amplitude. However, even for large RF amplitudes the precession amplitude cannot grow much beyond the offset angle between the free and pinned magnetic layers, because the spin-transfer torque changes sign to damp precession on the part of the magnetic trajectory where the precession angle exceeds the offset angle. We have considered whether other effects might also contribute to the saturation as a function of RF amplitude. We do not believe that the nonlinear shift

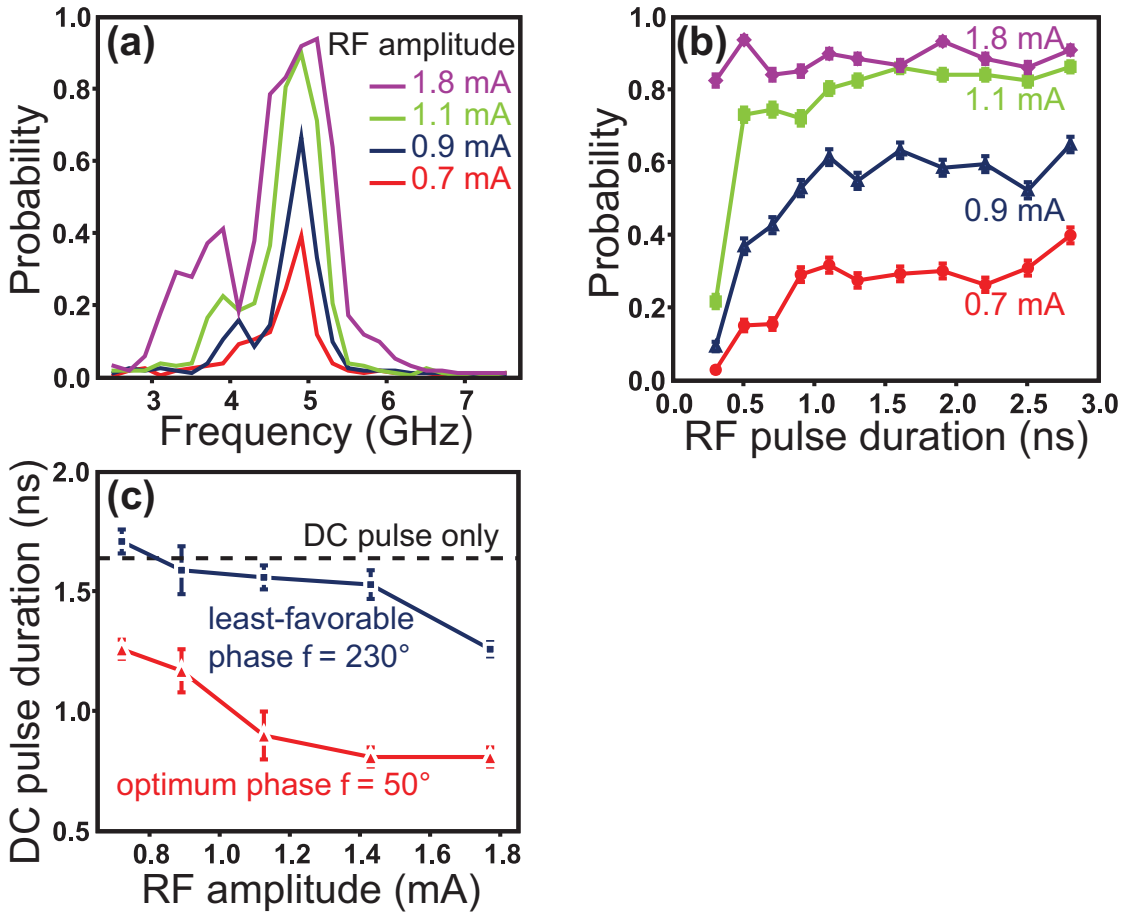

Figure 2.9: Dependence of switching on the parameters of the microwave pulse at a background temperature of 20 K. (a) Switching probability versus frequency at the optimum phase ϕ, measured using RF pulse amplitudes from 0.7 mA to 1.8 mA. The RF pulse duration is 1.7 ns and the square pulse parameters are 7.7 mA, 0.7 ns. (b) Switching probability for f = 4.9 GHz as a function of RF pulse duration measured at different RF pulse amplitudes from 0.7 mA to 1.8 mA. The square pulse parameters are the same as in (a).

in precession frequency with increasing precession amplitude should play a significant role for our devices, because macrospin modeling suggests that the change in frequency between precession angles of 5 and 30 should be only about 0.35 GHz, much less than the resonance linewidth, and because in Fig. 3a we observe little frequency shift as a function of RF amplitude. However, it is possible that instabilities in the macrospin state due to nonlinear coupling to short-wavelength spin waves at large precession angles might contribute to the

observed saturation. [79]

2.4.5 Effects of Thermal Fluctuations

While our results provide a proof of principle that resonantly-enhanced switching can provide better performance than switching by square pulses alone, for most applications switching must be achieved reliably in the presence of thermal fluctuations at room temperature, in contrast to our low-temperature results. In order to understand the influence of thermal fluctuations, and whether enhanced switching with resonant RF pulses might be extended to room temperature, we have performed experiments using square pulses with a lower amplitude (4.8 mA) and longer duration (2 ns), for which thermal fluctuations are significant even for a 20 K background temperature, and we also performed room temperature studies. At 20 K, we employed 1.4 mA, 0.8 ns RF pulses, which are sufficient to saturate the RF-excited precession even though they have considerably less amplitude than the square pulse. We find that the switching probability is still enhanced when assisted by RF pulse but its variation as a function of the relative phase ϕ is much weaker [Fig. 2.10(a)] than for the case of a larger, shorter square pulse [Fig. 2.6(b)]. In Fig. 2.10(b) we compare the distributions of switching times for a pulse with no RF component and for a pulse with an RF component with an optimized value of the relative phase ϕ. With the RF pulse, the square pulse duration needed for switching is shorter, but the width of the distribution is comparable to the case with no RF pulse. These results suggest a crossover to a regime in which thermal fluctuations occurring during the square pulse begin to dominate the dynamics. The RF pulse can still enhance switching by giving the free layer an increased

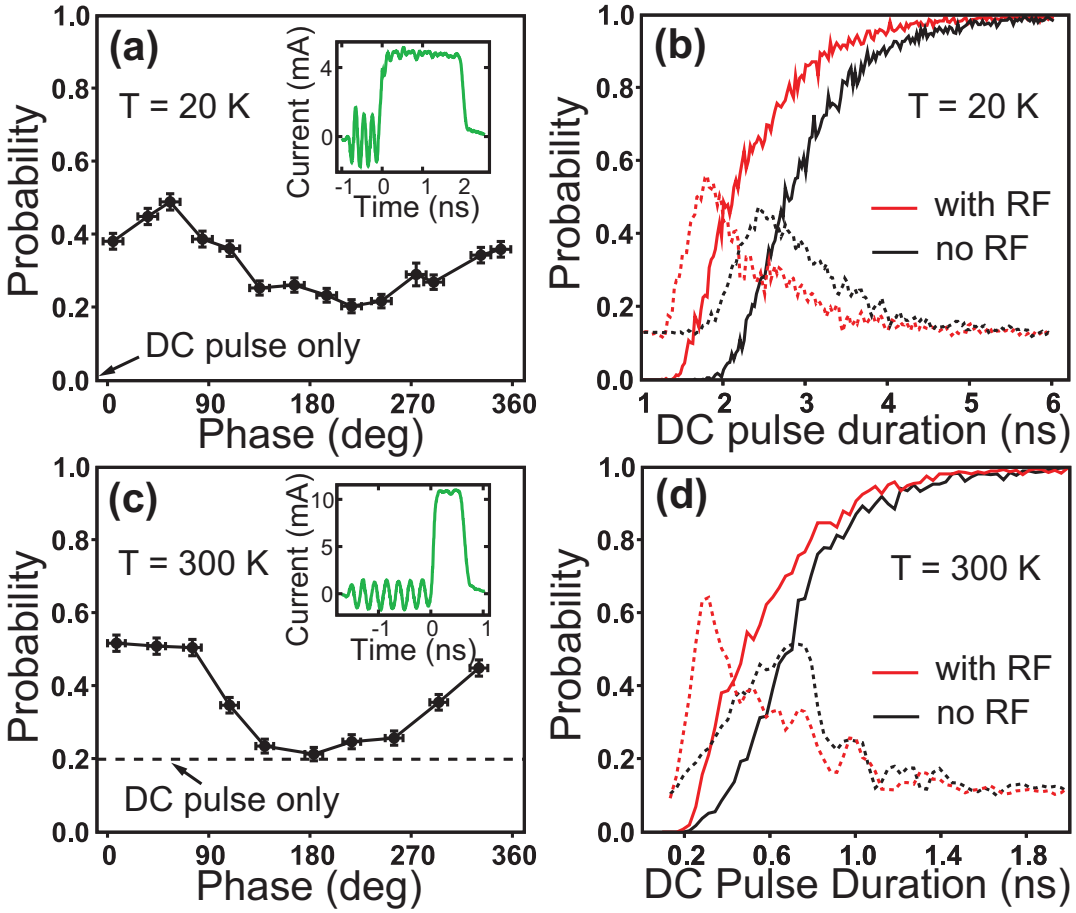

Figure 2.10: Effects of thermal fluctuations on resonantly-enhanced switching. (a) Switching probability as a function of the phase ϕ at a background temperature of 20 K, for 1.4 mA, 0.8 ns RF pulses with 4.8 mA, 2 ns square pulses. (b) Solid lines: Switching probability as a function of square pulse duration without an RF pulse and with a 1.4 mA, 0.8 ns RF pulse. The square pulse amplitudes are both 4.8 mA. Dotted lines: corresponding distributions of switching pulse duration. (c) Room-temperature switching probability as a function of the phase ϕ, for 1.5 mA, 1.5 ns RF pulses with 10.8 mA, 0.5 ns square pulses. (d) Solid lines: Room-temperature switching probability as a function of square pulse duration without an RF pulse and with a 1.5 mA, 1.5 ns RF pulse. The square amplitudes are both 10.8 mA. Dotted lines: corresponding distributions of switching pulse duration.

magnetic energy before the start of the square pulse, but the lack of strong phase dependence and the wide distribution of switching times indicate that the final switching process is dominated by thermal processes during the square pulse.

For temperatures above 100 K for our device geometry, we find that large square pulse amplitudes are necessary in order to observe any phase-dependent enhancement from an RF pulse – large enough square-pulse amplitudes to drive switching by themselves in just a few precession cycles. Figures 2.10(c) and 2.10(d) show the results of room temperature measurements using an RF pulse (1.4 ns, 1.5 mA) chosen to saturate the free layer precession, together with a 0.5 ns 10.8 mA square pulse. The distribution of switching times is centered at a slightly shorter square pulse duration when RF pulse is used, but the widths of the distributions in switching times are similar.

2.5 A Proposal to Enhance Spin-torque Switching at Room Temperature

These findings suggest a strategy for how the device design might be optimized to extend the benefits of resonantly-enhanced switching to room temperature. For the value of the equilibrium offset angle between the free and pinned layer magnetizations in our samples ($\approx 30^{\circ}$), we have seen that relatively small RF amplitudes are capable of exciting the precession amplitude to saturation (to a value close to the offset angle, according to macrospin simulations). The thermal fluctuations appear to interfere with the switching process primarily while the much larger square pulses are applied to complete the switching. This suggests that improving reliability in the presence of thermal fluctuations might be achieved by using a device design which allows the more-effective RF pulse to control the magnetic dynamics over a larger angular range, so as to rely less on the square-pulse component of the waveform. We therefore propose using

devices in which the pinned layer moment is exchange-biased at a very large angle, close to 90°, relative to the free-layer moment. It is true that this geometry will reduce the magnetoresistance signal used to read out the orientation of the free layer in memory devices, but the extraordinarily-large magnetoresistance values provided by MgO-based magnetic tunnel junctions [80] may provide sufficient read signal even for large offset angles, or else the free-layer orientation might be read out using a second junction on the opposite side from the pinned layer. An offset angle near 90° should allow the RF pulse to excite the free-layer coherently almost to the switching threshold, at which point only a modest square pulse may be needed to complete the switching process even in the presence of thermal fluctuations. This geometry also provides the advantage that an offset angle near 90° maximizes the strength of the RF torque per unit current, which may allow the use of thicker, more thermally-stable magnetic free layers without requiring larger RF current amplitudes. In addition to enabling potential improvements in switching speeds, reproducibility, and integrated power consumption, a successful implementation of resonant spin transfer switching might open new possibilities for memory architectures. For example, if the resonant frequencies of different storage elements in an array are varied using different shape anisotropies, it may be possible to address each element selectively by controlling the frequency of the RF pulse, thereby eliminating the need to include a select transistor with every storage bit.

CHAPTER 3

SINGLE-SHOT TIME-DOMAIN STUDIES OF SPIN-TORQUE-DRIVEN SWITCHING IN MAGNETIC TUNNEL JUNCTIONS

3.1 Introduction

Measurements in the time domain [22, 39–42, 64, 81] can provide the most direct information about magnetic dynamics. However, the majority of previous time-resolved studies of spin-torque switching [22, 39, 40, 64, 81] required averaging over many events, thereby hiding individual variations. Magnetic tunnel junctions (MTJs) can now provide resistance signals large enough for single-shot measurements, and previous initial experiments have measured resistance jumps associated with the completion of spin-torque switching in MTJs using single-shot techniques [41, 42], but they could not resolve the smaller signals associated with the precessional dynamics that produce the switching. Here we demonstrate a technique for substantially improving the sensitivity of single-shot measurements so that for the first time we observe directly the resistance oscillations associated with magnetic dynamics both prior to and during spin-torque switching. Analyses of individual traces allow measurements of coherence times, non-equilibrium excitation spectra, and variations in magnetization precession amplitude. We find that with a small in-plane hard-axis magnetic field the switching dynamics are more spatially coherent than for zero field. From these measurements, we obtain a view of the magnetic dynamics that is sufficiently detailed not only to assist in optimizing the switching process, but also to make MTJs promising model systems for probing the general properties of nonlinear systems subject to thermal fluctuations. The contents of this

chapter are adapted from work originally published as *Phys. Rev. Lett.* **104**, 097201 (2010).

3.2 Method

Time domain experiments of the resistance changes during spin-transfer switching are usually performed by measuring the response of the device resistance to an excitation voltage pulse by recording the reflected pulse or the transmitted pulse with a high speed oscilloscope. The reflection or transmission coefficient is determined by the device resistance. As the device resistance oscillates due to the precessional dynamics of the magnetic moment, it produces a time-varying reflection or transmission coefficient, which then mixes with the incident square pulse and produces an oscillating voltage signal. In previous experiments on spin valve devices [22, 39, 40], the scale of this oscillating signal was very small, typically less than 1 mV. Therefore, they required averaging over many switching events in addition to voltage amplification in order to achieve enough signal-to-noise ratio. This was done by exciting and resetting the device many times and triggering a sampling oscilloscope to record the averaged waveform. [82] For magnetic tunnel junctions, the large TMR ratio can now provide signals large enough (on the order of 10 mV) to be directly resolved by a storage oscilloscope without any averaging. [41, 42] However, current MTJ devices have resistance on the order of a few 100 Ω's. The large resistance mismatch to the 50 Ω transmission line produces a large background (100's of mV), which limits the dynamic range of the storage oscilloscope. To achieve sufficient sensitivity to resolve the oscillation voltage signal in detail, it is necessary to reduce the large background. Based on this idea, we have

developed a method to enhance the dynamic range of the measurement.

3.2.1 Circuit Design for Single-Shot Time Domain Measurement

The circuit we developed is shown in Fig. 3.1. The pulse generator produces an 100 ns long, 300 ps rise-time pulse. The pulse is split with a power divider into two parts. One part with amplitude V_{inc} is applied to the sample via one high-frequency probe. We detect the transmitted pulse with a second probe, and amplify initially with one stage of an inverting amplifier with effective gain of 5 dB. The transmitted pulse at the sample (before amplification) is

$$V(t) = \frac{V_{inc}}{1 + G_S(t)Z_0/2} \tag{3.1}$$

where $G_S(t) = 1/R_S(T)$ is the sample conductance (the reciprocal of the resistance), and $Z_0 = 50\ \Omega$ is the probe impedance. We can further expand $G_S(t)$ relative to a reference value. For example, for anti-parallel to parallel switching, we use the parallel state conductance G_P as the reference value, and write $G_S(t)$ as $G_S(t) = G_P + \Delta G(t)$. Since $\Delta G(t)Z_0$ is usually much less than 1, we can further expand Eq. 3.1 into

$$V(t) = \frac{1}{1 + G_P Z_0/2} V_{inc} + \frac{Z_0/2}{(1 + G_P Z_0/2)^2} V_{inc} \Delta G(t) \tag{3.2}$$

The first term in Eq. 3.2 can be attributed to the resistance mismatch between the device and RF probe. The second term corresponds to the resistance change associated with the magnetic dynamics. As mentioned before, the first term dominates the signal and limits the dynamic range of the experiment. A key step that substantially improves the dynamic range is that we combine the

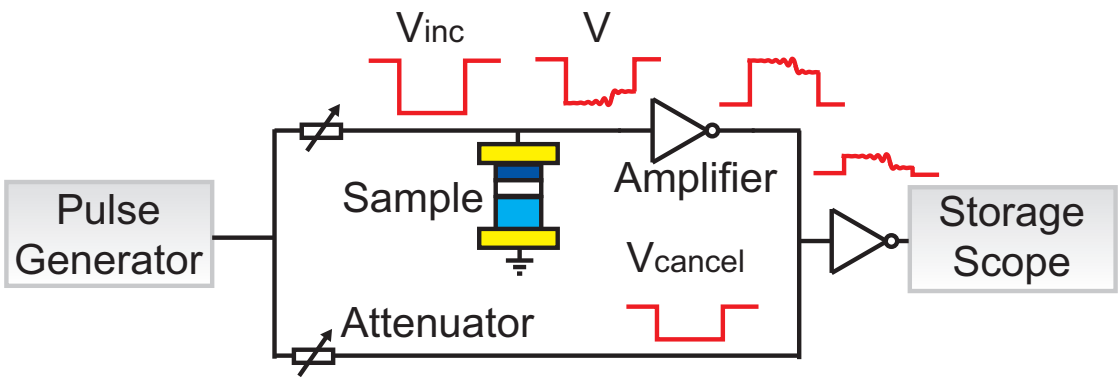

Figure 3.1: Schematic of the circuit for the single-shot time domain measurement.

transmitted signal with the split-off copy of the original pulse using a time delay and attenuation tuned so as to cancel the part of the transmitted pulse that does not depend on the magnetic dynamics. This enables us to detect smaller resistance changes than in previous single-shot measurements [41, 42], because we can apply additional amplification without saturating the amplifiers before or during the pulse. We record the signal with an 11 GHz, 40 GSamples/s storage oscilloscope following a total net gain of 14 dB.

3.2.2 Device Information

The MTJ samples that we study have the layer structure (in nm): bottom contact, synthetic antiferromagnet (SAF) pinned layer [IrMn (6.1) / CoFe (1.8) / Ru / CoFeB (2.0)], tunnel barrier [MgO], magnetic free layer [CoFe (0.5) / CoFeB (3.4)], top contact. Both the pinned and free layers are patterned into an elliptical 65×130 nm^2 cross section parallel to the SAF pinning. All measurements are performed at room temperature, and positive current corresponds to electron flow from the free to the pinned layer. An easy axis hysteresis loop is shown in Fig. 3.2. Our discussion of current-driven reversal will focus on switching

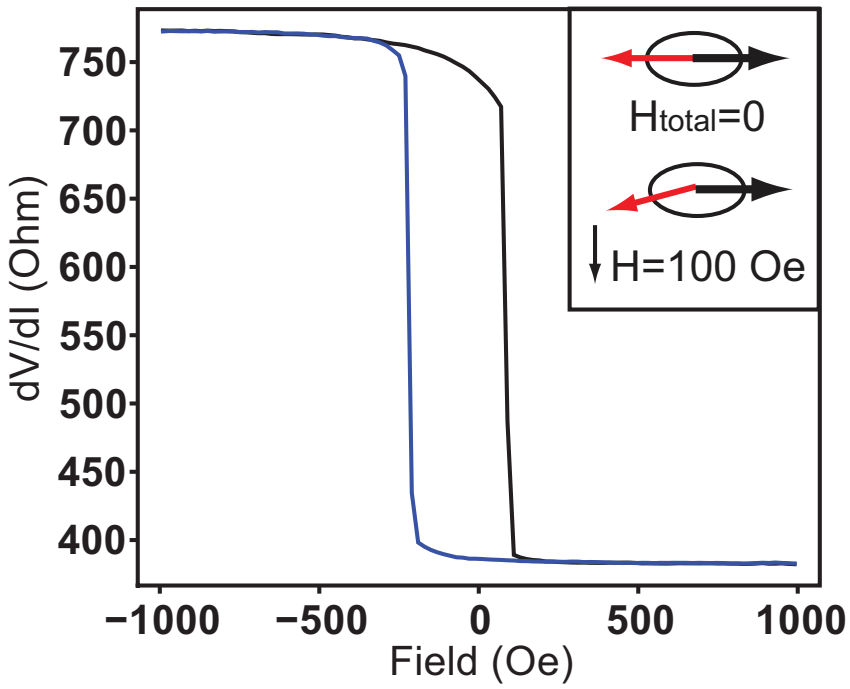

Figure 3.2: Resistance vs. magnetic field applied along the easy axis. Inset: initial magnetization configurations for zero total field and for an 100 Oe in-plane hard-axis field for which the free layer rotates by ~ 15° relative to the stationary fixed layer.

from the higher-resistance anti-parallel (AP) state to the parallel (P) state but measurements of P-to-AP dynamics are qualitatively similar. We will examine switching in both the case of zero total magnetic field on the free layer and the case that a small (100 Oe) field is applied along the in-plane hard axis, to rotate the free-layer magnetization approximately 15° from the AP configuration (see inset, Fig. 3.2). We will present data from one sample, but have studied two other devices in zero field and one other in the hard-axis field, with all showing the same differences depending on field geometry.

Figure 3.3 shows a representative measurement for the 100 Oe hard-axis field and a transmitted pulse amplitude V = 750 mV. The black curve in Fig. 3.3(a)

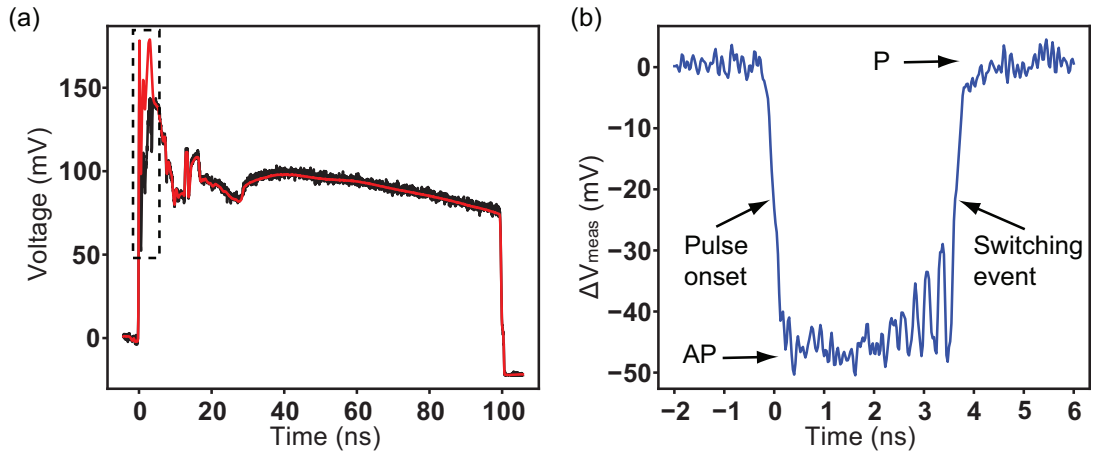

Figure 3.3: Example of the waveforms. (a) Black: waveform for one switching event from AP to P. Red: the average of 1000 traces taken for sample initiated in P state. This serves as a baseline curve for subtraction. (b) Switching waveform obtained by subtracting the baseline curve (the red curve in (a)) from the original waveform (the black curve in (a)).

is the waveform directly recorded by the oscilloscope as the output from the circuit corresponding to a switching event from AP state to P state. We can see that there is still some background that cannot be fully canceled by addition of the reference pulse, and the background is not flat due to distortion in the circuit, including multiple reflections, filtering, etc. To account for this background, we take an average baseline curve (the red curve in Fig. 3.3(a)) with the sample initialized to the P state, for which the negative pulse does not produce switching. Figure 3.3(b) is the waveform after background subtraction, which clearly shows the conductance variations above the noise background throughout the period between the pulse onset and the switching event. The rms noise level corresponds to $\sim$ 2% of the difference between AP and P conductances.

3.3 Measurement and Analysis

3.3.1 Distribution of Switching Times

Before analyzing the time traces, we will first demonstrate that our data correspond to thermally-assisted spin-torque switching [29, 30]. Figure 3.4 shows the switching-time distributions for three values of V, for the case of the 100 Oe hard-axis field. The broad widths of the distributions indicate that our pulse amplitudes $|V|$ are below the zero-temperature switching threshold so that switching is assisted by thermal fluctuations. The long-time tails of the distributions fit well to a simple exponential $\exp(-t/\tau_0(V))$. Extrapolating the measured values of $\tau_0(V)$ (Fig. 3.4, inset) to 1 ns gives an estimate for the zero-temperature switching threshold of -870 mV. We have not attempted to investigate higher values of $|V|$ because the MTJs are not sufficiently stable.

3.3.2 Switching Waveforms: Analysis of the Oscillation Pattern Leading up Switching

Now we turn to the detailed dynamics revealed by the time traces. In Fig. 3.5(a) and (b), we show selected traces with different switching times for V = -750 mV, for both the 100 Oe hard-axis field and zero total field. We resolve the conductance oscillations prior to switching in both configurations, with oscillation amplitudes that fluctuate with time. In the right columns of Fig. 3.5(a,b) we zoom in to each trace 2 ns before and after switching. For the 100 Oe hard-axis field (Fig. 3.5(a)), most traces show at least a few cycles

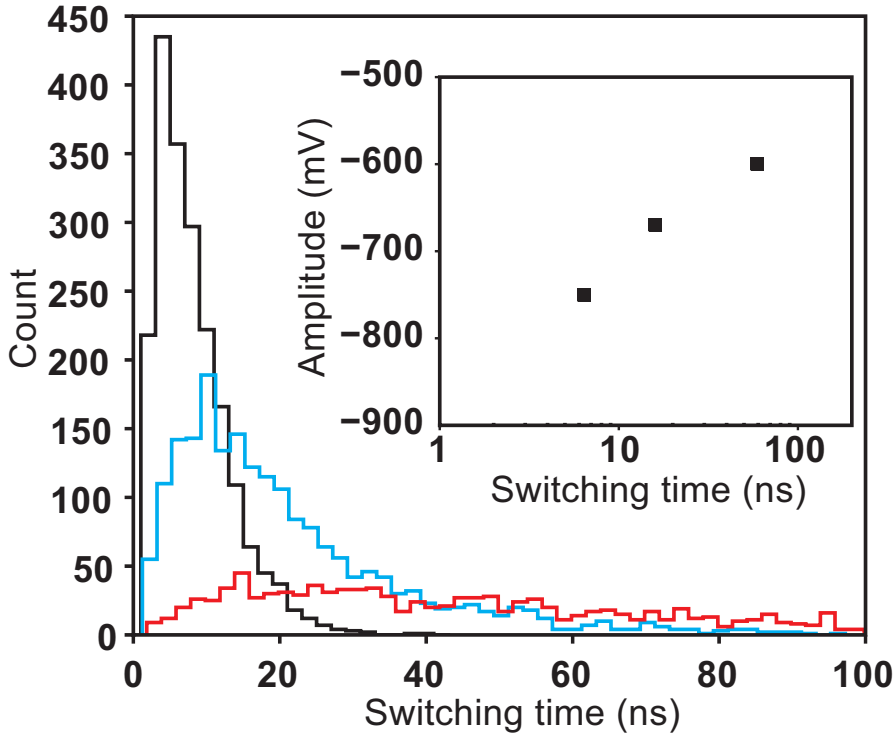

Figure 3.4: Histograms of switching times for V = 750 mV (narrowest distribution), 670 mV, and 600 mV (broadest distribution). Inset: Pulse amplitude vs. average switching time.

of large oscillations in the 2 ns prior to switching, corresponding to magnetic precession with large amplitude leading to reversal [10, 15, 39]. However, these oscillations show large variations from trace to trace, ranging from almost-vanishing amplitude (2nd curve in Fig. 3.5(a)) to oscillations close to one half the difference between the initial (≈AP) and final (≈P) values. For the zero total field case, the conductance oscillations immediately prior to switching are much weaker (Fig. 3.5(b)). Many traces for this case merely show a gradual increase in ΔV_{meas} without any significant oscillations immediately prior to switching.

Figures 3.5(c,d) show averages of 2000 traces with switching edges aligned, for the two field geometries. These averaged curves are very different from typical individual traces. Nevertheless, for the 100 Oe hard-axis field the

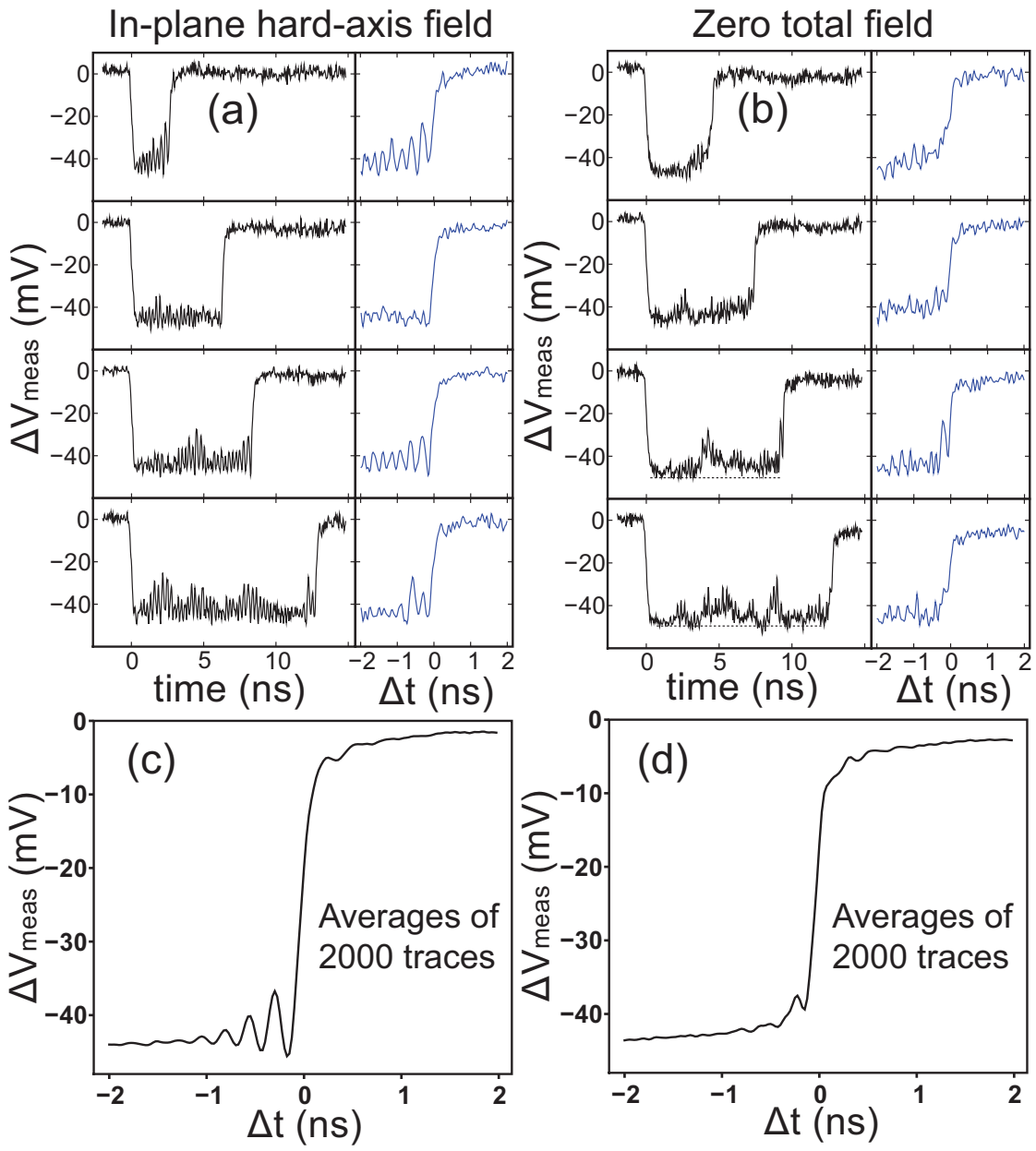

Figure 3.5: Measured oscillatory signals leading up switching for $V = 750$ mV. (a),(b) Representative switching traces for (a) an in-plane hard-axis field of 100 Oe and (b) zero total field, together with magnified views 2 ns before and 2 ns after the switching events. (c),(d) Average of 2000 measured traces with the switching edge aligned for (c) the in-plane hard-axis field and (d) zero total field.

averaged trace shows oscillations with increasing amplitude before switching (Fig. 3.5(c)), indicating that switching occurs preferentially at a particular phase of the conductance oscillations. The $(1/e)$ time scale for the averaged precession amplitude to build prior to reversal is 0.25 ± 0.02 ns for all V from -540 mV to -750 mV. This is likely a measure of the coherence time for dephasing between traces with differing precession angles, rather than a true measure of precession amplitude growth, because this scale is shorter than the correlation time for amplitude changes (determined below). For the averaged trace in the case of zero total field (Fig. 3.5(d)), the oscillatory features are almost entirely washed out, suggesting much weaker correlations between the oscillation phase and the switching time.

3.3.3 Micromagnetic Simulations: Non-Uniform Switching

We have performed micromagnetic simulations to understand these results, using the code described in [83, 84]. The simulation parameters are: free layer saturation magnetization $M_S = 1050$ emu/cm^3, damping = 0.025, exchange = 1.3×10^{-11} J/m, uniaxial anisotropy = 4×10^3 J/m^3, spin polarization = 0.6, and sample temperature = 400 K. The sample size is the same as in the experiment, the current density during the pulse is -2 $\times$ 10^7 A/cm^2, and the pinned layer is assumed to be immobile. We have implemented the simulations both with a spin torque vector oriented strictly within the plane defined by the electrode magnetizations and also with an additional perpendicular component with magnitude 30% of the in-plane torque [18], and we found no qualitative differences in outcomes for our sample geometry. All the simulation results we display will include the perpendicular torque. In Fig. 3.6, we plot examples of

simulated conductance traces for the two field configurations discussed above and also the averaged traces over 100 simulated reversals near the switching edges (compare to Figs. 3.5(c) and (d)). The simulations reproduce many of the features seen in the experiment including the differences in the coherence of the oscillations between the two field geometries. The calculated magnetic configurations during switching events (Fig. 3.6(e) and (f)) suggest that the typical mechanism for reversal differs for the two field geometries. Switching for zero total field generally proceeds with one end of the sample switching first and the rest following by domain wall propagation [42] (Fig. 3.6(e)). For the hard-axis field, the switching dynamics are generally more spatially uniform, albeit with local fluctuations (Fig. 3.6(f)). Our measurements therefore support a prediction that a hard-axis field should promote macrospin switching behavior [85]. Our findings may also be related to observations that a large (~1000 Oe) hard-axis field decreases the linewidth of spin-torque nano-oscillators at large currents [47], although this is a very different dynamical regime than thermally-activated switching.

The difference in the degree of spatial uniformity in our two field geometries can be observed directly in the time traces long before switching. For zero total field, the local minima in the fluctuations of ΔV_{meas} exhibit excursions from the global minimum on scales of several ns, much longer than any precessional period (see especially the 3rd and 4th panels in Fig. 3.5(b)). For the 100 Oe hard-axis field, the local minima in ΔV_{meas} are more closely clustered near the AP value (Fig. 3.5(a)). Large excursions of the sort present for the zero-field case are inconsistent with any approximately spatially-homogeneous dynamics for a thin-film magnetic sample, since at zero field the free-layer moment should pass close to the AP configuration twice per precessional cycle, each time giving the

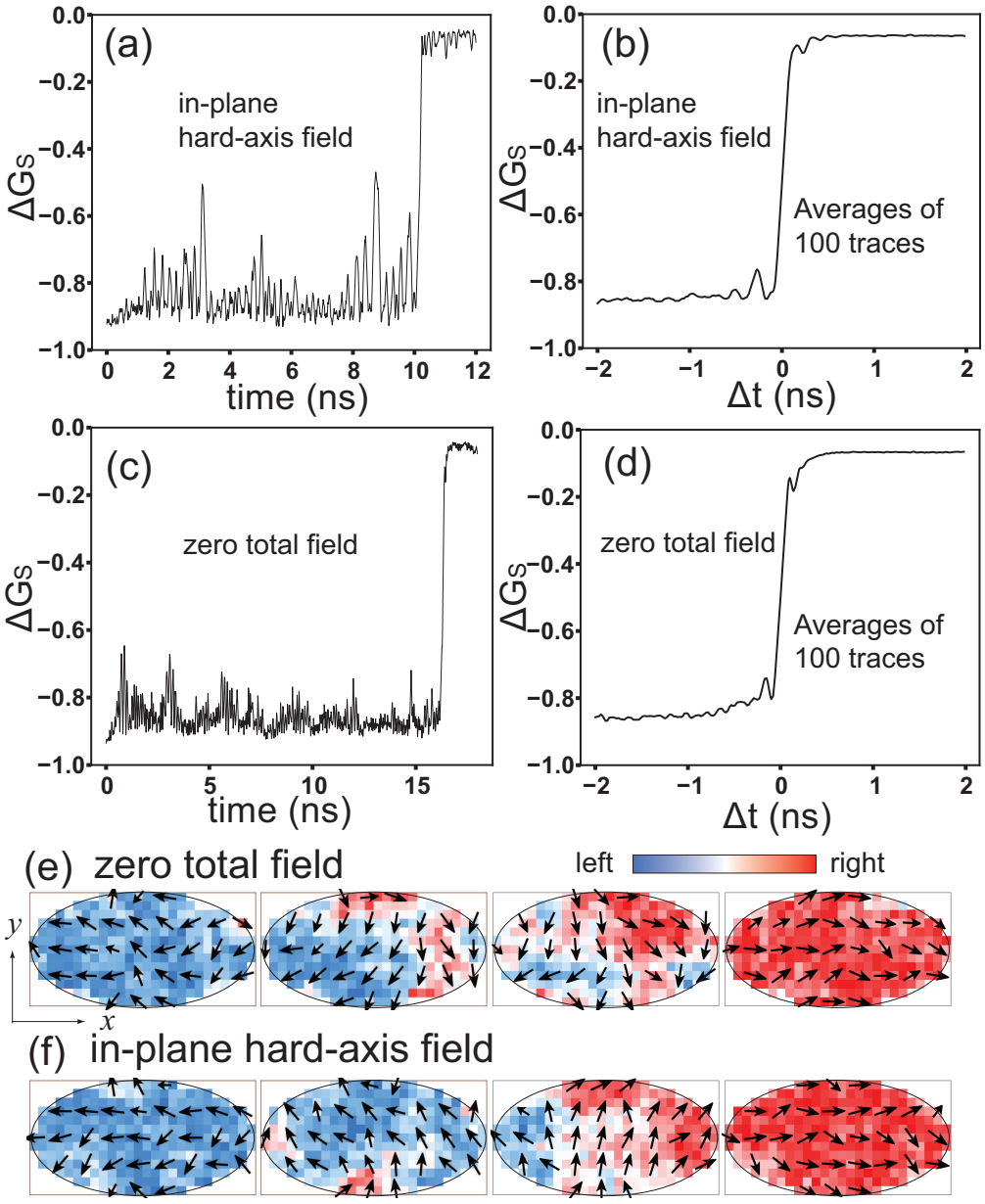

Figure 3.6: Micromagnetic simulation results. (a),(c) Simulated switching traces for the two field geometries. The change in conductance is normalized by the difference $G_P - G_{AP}$. (b),(d) Averages of 100 simulated switching traces with the switching edges aligned. (e),(f) Snapshots with 70 ps spacing of micromagnetic configurations during the switching events. The color scale denotes the magnetization component along the x axis.

same global minimum in ΔV_{meas}.

3.3.4 Analysis of Magnetic Dynamics in Thermally-activated Switching Traces

Coherence Times of Thermally Excited Magnetic Dynamics

The excellent sensitivity of our measurements allows us to analyze the magnetic dynamics even where the conductance oscillations are small, well away from the switching event. Fig. 3.7(a) plots autocorrelation functions of the conductance versus time for the full interval between pulse onset and switching in the case of the 100 Oe hard axis field, averaged over all switching traces with switching times longer than 10 ns at each value of V and normalized to the full difference between initial and final conductances. We find decoherence times t_c ranging from 0.54 ns at 540 mV to 0.45 ns at -750 mV (inset, Fig 3.7(b)). To help distinguish between frequency and amplitude variations, we plot in Fig. 3.7(b) autocorrelation functions of the oscillation amplitude versus peak number, determined by measuring every conductance peak between the pulse onset and switching. The coherence times for amplitude fluctuations Δt_A are greater than but comparable to Δt_c at each value of V, from which we conclude that both frequency and amplitude variations are significant in these $\geq$ room temperature fluctuations. The corresponding coherence times predicted by our micromagnetic simulation are $\Delta t_c \approx \Delta t_A = 0.22 \pm 0.03$ ns, approximately independent of bias. In both the experiment and simulations, Δt_c and Δt_A are short, at most a few precession periods, showing that thermal fluctuations are a strong perturbation and simple pictures of zero-temperature dynamics are not a

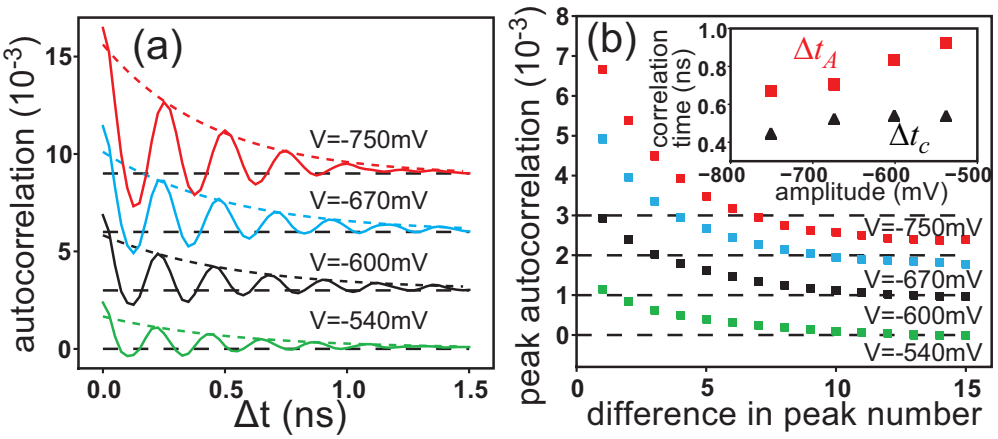

Figure 3.7: Analysis of the coherence times of thermally excited magnetic dynamics. (a) Autocorrelation functions of pre-switching conductance variations, normalized to the conductance difference before and after switching. The dotted lines are exponential fits to the peaks. The curves are offset vertically with horizontal lines denoting zero. (b) Autocorrelation functions for the conductance peak amplitude versus peak number. Inset: correlation times Δt_c from (a) and Δt_A from (b). Both (a) and (b) correspond to the 100 Oe in-plane hard-axis field configuration.

good approximation. [15] Surprisingly, the measured coherence times decrease with increasing values of $|V|$, whereas spin torque for $V < 0$ might be expected to decrease the effective damping and therefore increase the coherence time. We interpret the decrease in the coherence times with $|V|$ to be a sign of heating in these nonlinear oscillators.

Thermally-excited Ferromagnetic Resonance Spectra of the Pre-switching Dynamics

We can also Fourier transform our time traces for the pre-switching dynamics to achieve a measurement equivalent to thermally-excited ferromagnetic resonance [86], but accomplished for the very short-lived (< 100 ns) nonequilibrium state before switching. Figures 3.8(d) and (b) show power spectra for the

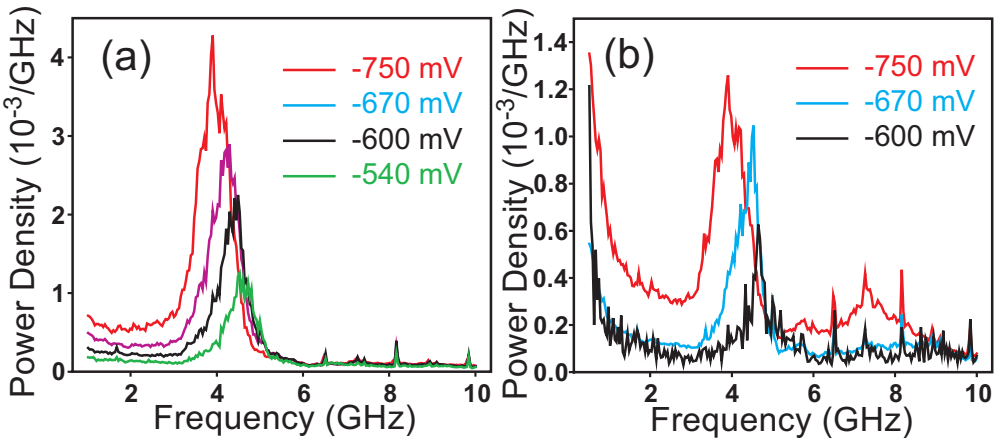

Figure 3.8: (a) Averaged Fourier spectra of normalized conductance variations for the hard-axis field configuration. (b) Averaged Fourier spectra for zero total field.

interval between the pulse onset and switching, averaged over all traces with switching times longer than 10 ns at each value of V for the two field geometries. For the 100 Oe hard-axis field (Fig. 3.8(a)), the spectra show a well-defined peak which with increasing $|V|$ grows in amplitude and shifts to lower frequency. The increasing amplitude of the peak can be explained by the reduction in effective magnetic damping due to the spin-transfer torque [10, 15], together with heating. The frequency shift can be understood as due primarily to the dependence of frequency on precession amplitude [14]. We estimate that the rms precesion angle ranges from 8° for V = -540 mV to 14° for V = -750 mV for the 100 Oe hard-axis field. For zero total field (Fig. 3.8(d)), the Fourier spectra show weaker peaks, and possess a low-frequency tail. This is another indication of incoherent dynamics for this field geometry.

Statistical Distributions of Magnetic Fluctuations

We can further test predictions that under the influence of the spin torque the non-equilibrium magnetic fluctuations are nevertheless described by a

Boltzmann distribution $\propto [-E/k_B T_{eff}(V)]$, where E is the magnetic energy and $T_{eff}(V)$ is an effective temperature [29, 30]. We do this for the more-spatially-uniform case of the hard-axis field. We first relate each local maxima in $\Delta V_{meas}(t)$ to a maximum in-plane deflection θ by assuming that the conductance of the MTJ varies as $\cos(\theta)$. For a hard-axis field, we can then estimate the magnetic energy per unit volume at the maxima to be

$$\begin{aligned} E(\theta) &= \frac{1}{2} M_S H_K \sin^2\theta - M_S H_{ext} \cos(\theta - \frac{\pi}{2}) + E_0 \\ &= \frac{1}{2} M_S H_K (\sin\theta - \frac{H_{ext}}{H_K})^2 \end{aligned} \tag{3.3}$$

where the arbitrary constant $E_0 = M_S H_{ext}^2/(2H_K)$ is chosen so that the minimum energy is zero. The energy barrier per unit volume for switching is $E_b = M_S H_K (1 - H_{ext}/H_K)^2/2$. In Fig. 3.9(a) we plot the resulting experimental histograms for $E(\theta)/E_b$ on a semilog scale for several different values of V, using the value $H_K = 280$ Oe determined from the magnetic-field switching curve near zero bias. These distributions fall to a good approximation on straight lines for energies corresponding to values of θ well above the background noise level, in agreement with the Boltzmann predictions. The slopes of the lines give a measure of $E_b/k_B T_{eff}(V)$ (Fig. 3.9(b)), which we find decreases as a function of $|V|$ in reasonable agreement with the predicted [29, 30] linear dependence $E_b/k_B T_{eff}(V) = (1 - V/V_{c0}) E_b/k_B T$.

3.4 Conclusion

In summary, we have performed single-shot measurements of the resistance during thermally-assisted spin-torque-induced switching in MTJs, achieving for the first time the sensitivity to measure the magnetization dynamics both before

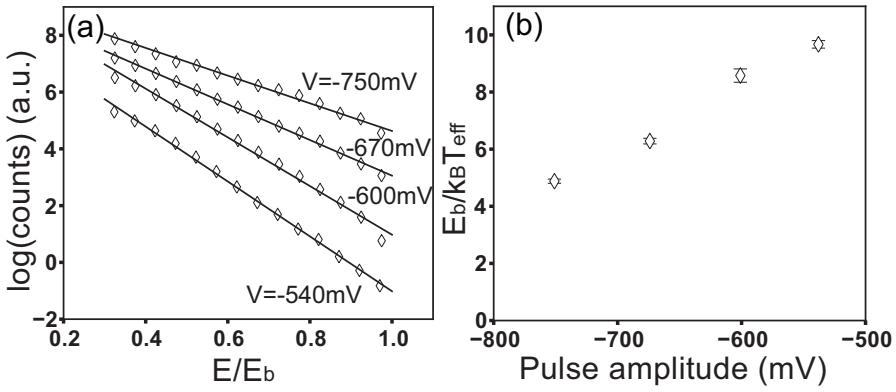

Figure 3.9: Statistical distribution of the magnetic energy. (a) Histograms of the energy distributions of the non-equilibrium magnetic dynamics generated by spin torque and temperature (at room temperature) for the in-plane hard-axis field configuration. The data for different V are offset vertically. The solid lines are linear fits for large values of E/E_b. (b) Values of E_b/k_BT_{eff} extracted from the fitted slopes in (a).

and during individual switching events. Our technique provides measurements of coherence times, frequency spectra and statistical distributions for the highly-nonequilibrium, short-lived fluctuational dynamics preceding switching. The measurements also provide a detailed view that the switching mechanism can vary depending on the magnitude of a hard-axis magnetic field.

3.5 Appendices: Notes on Single-shot Measurement Circuit

3.5.1 Calculation of the Transmission Coefficient

For the measurement circuit described in the main text of this chapter, the voltage transmission and reflection at the sample can be calculated considering the equivalent circuit shown in Fig. 3.10. Assume the incident pulse has an amplitude, V_{inc}. Since the device resistance, R_S, is mismatched to the

characteristic impedance of the RF transmission line and probe, $Z_0 = 50\ \Omega$, there will be signals both reflected (V_{ref}) and transmitted (V_{tran}). The requirements for the voltage and current at the sample junction are the following:

$$V_{inc} + V_{ref} = V_{tran} \tag{3.4}$$

$$V_{tran} = V_S \tag{3.5}$$

$$I_{inc} - I_{ref} = I_{tran} + I_S \tag{3.6}$$

The relations between the voltages and currents are:

$$\frac{V_{inc}}{I_{inc}} = \frac{V_{tran}}{I_{tran}} = \frac{V_{ref}}{I_{ref}} = Z_0 \tag{3.7}$$

$$\frac{V_S}{I_S} = R_S \tag{3.8}$$

We solve the above equations and obtain the expressions of V_{tran}, V_{ref} and V_S in terms of V_{inc}, Z_0 and R_S.

$$V_S = V_{tran} = \frac{1}{1 + \frac{Z_0}{2R_S}} V_{inc} \tag{3.9}$$

$$V_{ref} = -\frac{\frac{Z_0}{2R_S}}{1 + \frac{Z_0}{2R_S}} V_{inc} \tag{3.10}$$

Consider a device with parameters: $R_P = 400\ \Omega$ and $R_{AP} = 500\ \Omega$ under the voltage pulse applied. The signal corresponding to AP-P switching is $\Delta V = 0.011 V_{inc}$, while the background signal is $V_{tran} = 0.941 V_{inc}$, and $\Delta V / V_{tran} = 1.2\%$.

The equivalent circuit suggests a way to measure the actual voltage amplitude coupled to the sample by measuring directly the transmitted pulse since we have $V_S = V_{tran}$. Keep in mind that we need to avoid sample switching during the voltage measurement. For AP-P switching, we can either initialize the sample into P state and measure $V_{tran,P}$,[1] or we can apply a strong magnetic

[1] We actually want to measure the voltage coupled to the sample in the AP state, i.e. $V_{tran,AP}$, but $V_{tran,P}$ only differes from $V_{tran,AP}$ by a few percent and is a good enough approximation.

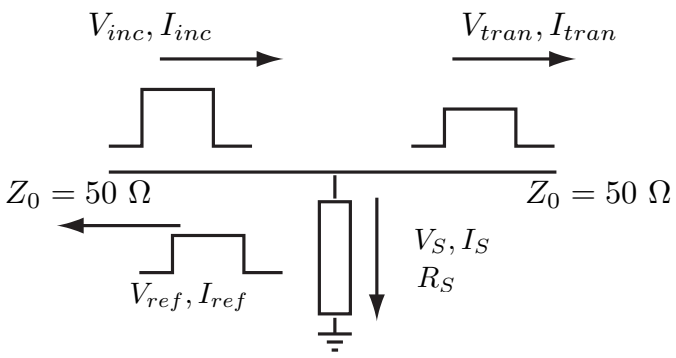

Figure 3.10: Equivalent circuit for the connection method used in the single-shot measurement.

field to stabilize the sample in the AP state so that the negative voltage pulse will not induce switching. We can also directly measure V_{inc} and use Eq. 3.9 to determine the sample resistance under the voltage pulse applied.[2]

3.5.2 Tuning the Reference Pulse

The key step in the single-shot measurement circuit is that we use a reference pulse which has the same shape as the pulse applied on the sample to cancel the background of the transmitted pulse. Both the amplitude and time delay of the reference pulse need to be carefully tuned to achieve the best cancellation results. For time domain measurement on spin-transfer switching, it is important to achieve a broad bandwidth in the microwave circuit, as the square pulse (100 ns long) and the magnetic dynamics during switching span a broad frequency range (from a few MHz to ~10 GHz).

To control the time delay of the reference pulse, we simply use cables of different lengths for the path of the reference pulse.[3] This can tune the time delay to

[2]Remember to measure V_{inc} after the bias tee since the bias tee attenuates the pulse by about 1 dB.

[3]There are some commercial delay line products, but those usually only work in a narrow

match the transmitted pulse down to nanosecond range. For fine tuning, there are SMA connectors (M-M, F-F, F-M, etc) of different lengths (millimeters in difference) and trying different combinations of them can achieve quite accurate time delay. The square pulse has a rise time of 70 ps, so mismatch of more than that will cause huge spikes around the rising and falling edges after combining the positive and negative pulses, which would compromise the dynamic range of the oscilloscope.

For the amplitude of the reference pulse, a 1-dB step variable attenuator with bandwidth of DC - 18 GHz is used. Changing the attenuation will not change the time delay through it. This allows the attenuation to be tuned independently of the time delay. 1 dB $\approx$ 12%, therefore we can only match the amplitude of the reference pulse down to below 12% of the background of the transmitted pulse. This limits how well the background signal can be cancelled. The voltage corresponding to AP-P switching is to the most only a few percents of the background. In most cases, the background cannot be fully cancelled and the residual background is comparable or even greater than the voltage level corresponding to switching. To avoid any saturation, the dynamic range used on the oscilloscope which needs to cover both the switching voltage and the residual background has to be three or four times of what is really needed (the switching voltage).

Another factor to be considered is that some microwave components in the circuit, such as bias tee or the RF amplifier, have a low cutoff frequency of around 100 KHz. The flat top of the square pulse will be inclined a little bit due to capacitor charging/discharging. Although it only causes about less than 5% change in pulse amplitude during the 100 ns pulse duration, it can still be a

frequency bandwidth for analog signals.

problem limiting the dynamic range. To minimize this problem, I added the same type of bias tee[4] in the reference path to generate similar slope in the reference pulse so as to balance the circuit.

3.5.3 Another Connection Method with Better Performance

In the experiment we have discussed in this chapter up to now, we use two RF probes to connect to the sample, both of which are connected in the same fashion, i.e., both signal pins to the top leads and both ground pins to the bottom leads. As illustrated in the equivalent circuit shown in Fig. 3.10, the sample is parallel with the transmission line loads. There can be another type of connection scheme, where the sample is in series with the transmission line loads. This was first mentioned to me by Jonathan Sun. I have recently implemented this method and it turns out that with this method the background voltage amplitude in the transmitted pulse is much less and the switching signal is larger by about a factor of 2 compared to the original method, both of which favor an enhanced dynamic range of the measurement.

The connection method is illustrated in Fig. 3.11. Figure 3.11(a) shows how the two RF probes are connected to the sample. The signal pin of one probe is connected to the top lead and the signal pin of the other to the bottom lead. The ground pins of two RF probes are connected together to define the ground level. Note that the grounding pads are not connected to either top or bottom leads. As shown in the equivalent circuit in Fig. 3.11(b), the square pulse is applied through one RF probe, transmitted through the sample, and then gets picked

[4]The bias tee and the RF amplifier have similar low cutoff frequency. Adding one of them is usually good enough to balance the circuit.

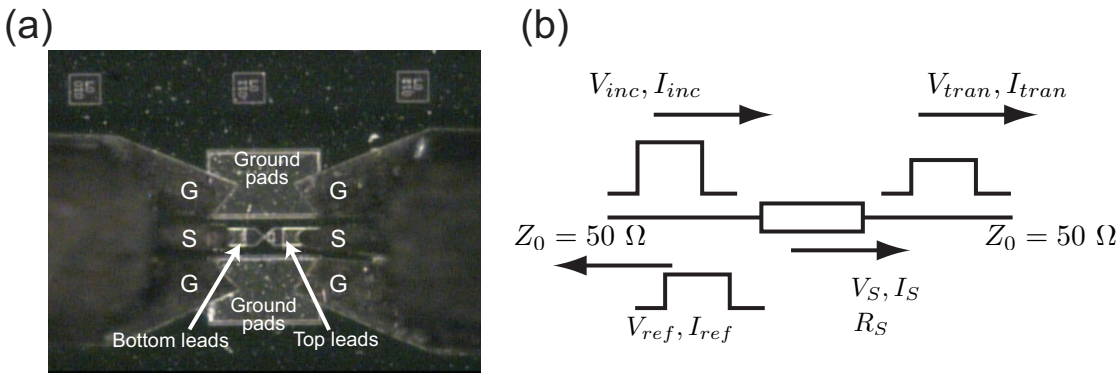

Figure 3.11: (a) CCD image of the sample in series with the two RF probes. Neither leads are connected to ground pads. (b) Equivalent circuit.

up by the other probe. Following similar analysis, we can calculate the relations between V_{inc}, V_{ref}, V_{tran} and V_S. We have

$$V_S = V_{inc} + V_{ref} - V_{tran} \tag{3.11}$$

$$I_{inc} = I_{ref} + I_S \tag{3.12}$$

$$I_S = I_{tran} \tag{3.13}$$

and

$$\frac{V_{inc}}{I_{inc}} = \frac{V_{tran}}{I_{tran}} = \frac{V_{ref}}{I_{ref}} = Z_0 \tag{3.14}$$

$$\frac{V_S}{I_S} = R_S \tag{3.15}$$

The solutions are

$$V_{tran} = \frac{1}{1 + \frac{R_S}{2Z_0}} V_{inc} \tag{3.16}$$

$$V_{ref} = \frac{\frac{R_S}{2Z_0}}{1 + \frac{R_S}{2Z_0}} V_{inc} \tag{3.17}$$

$$V_S = 2V_{ref} \tag{3.18}$$

Figure 3.12 shows the comparison between two connection methods for the transmitted voltage amplitude V_{tran} normalized to the actual voltage on

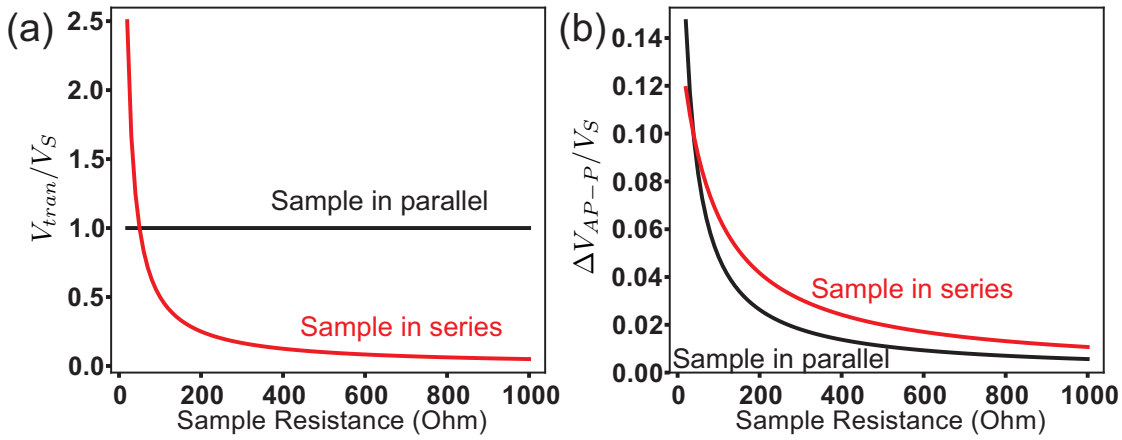

Figure 3.12: Comparison between the two sample connection methods for (a) V_{tran} normalized by V_S and (b) ΔV_{AP-P} normalized by V_S

.

the sample V_S (Fig. 3.12(a)) and the signal amplitude corresponding to AP-P switching normalized to V_S (Fig. 3.12(b)). For sample resistance greater than 50 Ω, the "series" connection method provides lower background voltage and larger signal amplitude than the "parallel" method. For the MTJ devices we have measured, the resistance values are in the range of 200 Ω to 600 Ω. With the "series" method, the background is only about 20% of that for the "parallel" method, while the signal amplitude is enhanced by about a factor of 2.

CHAPTER 4

IMAGING MAGNETIC NORMAL MODES DRIVEN BY SPIN TRANSFER TORQUE IN MAGNETIC NANOPILLAR DEVICES

4.1 Introduction

The majority of previous spin transfer experiments have used electrical methods to characterize the magnetic dynamics excited by spin torque. These experiments have helped us establish good understanding of the spin transfer torque and the types of magnetic dynamics it can excite in a nanomagnet. As discussed in the introduction chapter, early analyses of these experiments often assumed for simplicity the macrospin picture where the moment of the ferromagnetic layers is described as a single domain without considering its internal spatial structure. This model is successful in explaining many of the phenomena observed in the experiments qualitatively or even quantitatively. This can be ascribed to the fact that the scale of the devices studied (~ 100 nm) is comparable to or shorter than the length scale of a magnetic domain wall due to strong exchange coupling between neighboring spins.

However, some experiments suggest that the macrospin picture is often insufficient in describing the magnetic dynamics in nanoscale magnetic devices, and one has to turn to micromagnetic modeling for correct understanding, where the spatial structure of the magnetic moment orientations is taken into account. (For example, explanation of some results in the single-shot time domain measurements described in Chap. 3) So the field is facing the following questions: How non-uniform are the high-frequency magnetic modes excited by spin-transfer torques? Which of the uniform or non-uniform modes

are important in understanding spin-transfer-driven magnetic precession and switching? To what extent are magnetic modes in different magnetic layers in a multilayer device coupled together?

In this chapter I will describe our ongoing experiment of using soft X-ray microscopy to image magnetic normal modes driven by spin transfer torque in a magnetic spin valve structure. By applying a microwave current, we selectively excite a particular normal mode and perform time-resolved X-ray microscopy measurements to image its spatial structure. We observe different degrees of spatial non-uniformity for two mode branches we imaged. The mode at higher frequency is more spatially uniform than the other. At low magnetic fields where the two modes are close in frequency and excited at the same time, the more non-uniform mode dominates the overall behavior of the dynamics.

4.1.1 X-ray Microscopy and X-ray Magnetic Circular Dichroism

Micromagnetic behaviors of spin transfer excited magnetic dynamics have been studied in a great deal through numerical simulations (for a recent review, see Ref. [63]). Experimentally, however, direct observation of the micromagnetic dynamics in the nanomagnet has been challenging since it requires a combination of key features for the imaging tool. These features include: i) high spatial resolution below 100 nm which is the typical size of the nanomagnet; ii) high temporal resolution below 100 ps as the magnetic dynamics is in GHz range; iii) the ability to apply current without interfering with imaging; iv) bulk sensitivity (not limited to the material surface) as the magnetic layers of interest are buried underneath metal leads which apply current to the sample. For

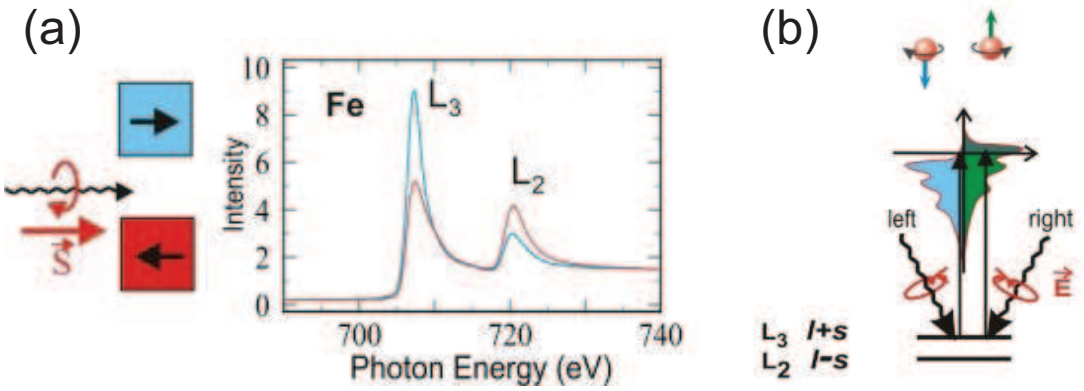

Figure 4.1: The XMCD effect illustrated for L-edge absorption in Fe metal. (a) The absorption spectra for the same X-ray polarization when the magnetization is reversed. (b) Illustration of the polarization dependent transition. Modified from [88].

many commonly used magnetic imaging techniques such as magneto-optical Kerr microscopy, magnetic force microscopy, spin-polarized scanning tunneling microscopy, photoemission electron microscopy, etc., each only offers some of the features but not all of them combined in a single technique. Synchrotron-based X-ray microscopy has the capabilities in all of these requirements and is a unique tool to study the micromagnetic behavior of spin-torque-driven magnetization dynamics.

X-ray microscopy is based on the X-ray Magnetic Circular Dichroism (XMCD) effect (for a review, see, for example, [87]). XMCD refers to the change of absorption between two different circularly polarized X-ray photons when passing through a magnetic material. The absorption depends on the relative orientation of the magnetic moments and the photon helicity, as shown in Fig. 4.1.

The physical process can be understood as the following. In 3d transition metals, the magnetic properties are primarily determined by the 3d shell electrons. In XMCD absorption experiments, transitions from 2p core electrons

to unfilled 3d states are excited by the circularly polarized X-ray photons. For the 2p states, the energy levels are split into two sublevels, $p_{3/2}(L_3)$ and $p_{1/2}(L_2)$, due to spin-orbit coupling, and these two sublevels have opposite sign for the spin-orbit coupling, $p_{3/2}$: $l + s$ and $p_{1/2}$: $l - s$. When a circularly polarized photon is absorbed by a 2p electron, it transfers its angular momentum ($\hbar$ or $-\hbar$ for right or left circular polarization) to the excited electron. This angular momentum in part is transferred to spin due to spin-orbit coupling. For $p_{3/2}$ and $p_{1/2}$ states, since they have opposite spin-orbit coupling, the spin of the excited electron is also opposite. Here the spin quantization axis is along the photon helicity axis which is also the X-ray propagation direction. During the transition from 2p to 3d states, electron spin is conserved due to dipole selection rules. The 3d states are spin polarized relative to the magnetization direction, i.e., they have different densities of states for spin-up and spin-down electrons. Therefore, when the magnetization direction (that defines the spin of the 3d states) is aligned along the X-ray photon polarization (that defines the spin of the excited 2p electron), the transition probabilities and hence the absorption are different for $2p_{3/2}$-3d (L_3 edge) and $2p_{1/2}$-3d (L_2 edge) transitions. When either the photon polarization or the magnetization is reversed, the changes in L_3 and L_2 absorption are opposite.

In XMCD microscopy experiments, to study the spatial distribution of the orientation of local magnetic moments, it is usually enough to look at a single absorption edge. The magnetic information can be extracted from the XMCD contrast by taking transmission data with opposite X-ray helicities from the following relationship [89].

$$\begin{aligned} \frac{\Delta I}{I} = \frac{I^+ - I^-}{I^+ + I^-} &= -\tanh(P\mu_c d\cos\theta) \\ &\approx -P\mu_c d\cos\theta \end{aligned} \tag{4.1}$$

where I^+ (I^-) is the transmitted light intensity for right (left) photon helicity, P is the polarization of the X-ray beam, μ_c is the spin-dependent part of the absorption coefficient per unit thickness, d is the thickness of the sample and θ is the relative angle between the beam axis (photon helicity axis) and magnetization. The approximation is valid for small values of $P\mu_c d\cos\theta$.

The absorption edge is material specific. This allows for imaging magnetic states of different elements in the sample by tuning the photon energy to a particular absorption edge. The elemental selectivity is very useful for studying spin-transfer physics as it allows for isolation of the magnetic states of the particular layer of interest and also enables the study of the coupling between different magnetic materials within the same layer or in different layers.

4.1.2 X-ray Transmission Microscopy

In our experiments, we perform X-ray microscopy measurements at two beamlines at the Advanced Light Source (ALS) of Lawrence Berkeley National Laboratory : the full-field X-ray transmission microscope station at Beamline 6.1.2 (XM-1) and the scanning transmission X-ray microscope station at Beamline 11.0.2 (STXM). The two beamlines are based on different imaging principles and each has its own advantages and disadvantages, which I will discuss below.

Full-Field X-ray Transmission Microscope at ALS Beamline 6.1.2 (XM-1)

The schematics of XM-1 is illustrated in Fig. 4.2. Its imaging mechanism is very similar to that in a conventional light microscope. The high intensity X-

ray photons produced by the bending magnet in ALS storage ring are directed to the condenser by a plane mirror. The condenser is a Fresnel zone plate that focuses X-ray photons of different energies at different distances from the zone plate. Then a pinhole is placed at the focus position of the desired photon energy to selectively pass through photons within a narrow bandwidth of that energy. The polarization of the photon can also be controlled by an entry slit before the condenser as X-ray photons of different helicities are spatially separated above and below the beam axis. These components together provide the X-ray illumination for the sample, which has a field of view of about 10 μm in diameter.

X-ray photons then transmit through the magnetic sample where XMCD effects take place. Transmitted photons are collected by the objective which is also a Fresnel zone plate. This zone plate focuses the X-ray photons onto the imaging plane similar to the objective lens in a conventional light microscope. On the imaging plane sits a soft X-ray sensitive CCD camera which records the X-ray image of the sample.

The CCD camera on the XM-1 records a full image all at once. The accumulation time is chosen based on the photon flux. The spatial resolution is diffraction limited by the objective zone plate and is currently about 25 nm for our experiment. The time resolution is 70 ps determined by the X-ray pulse width produced by the ALS storage ring. The procedure to perform time-resolved measurements on XM-1 will be described later.

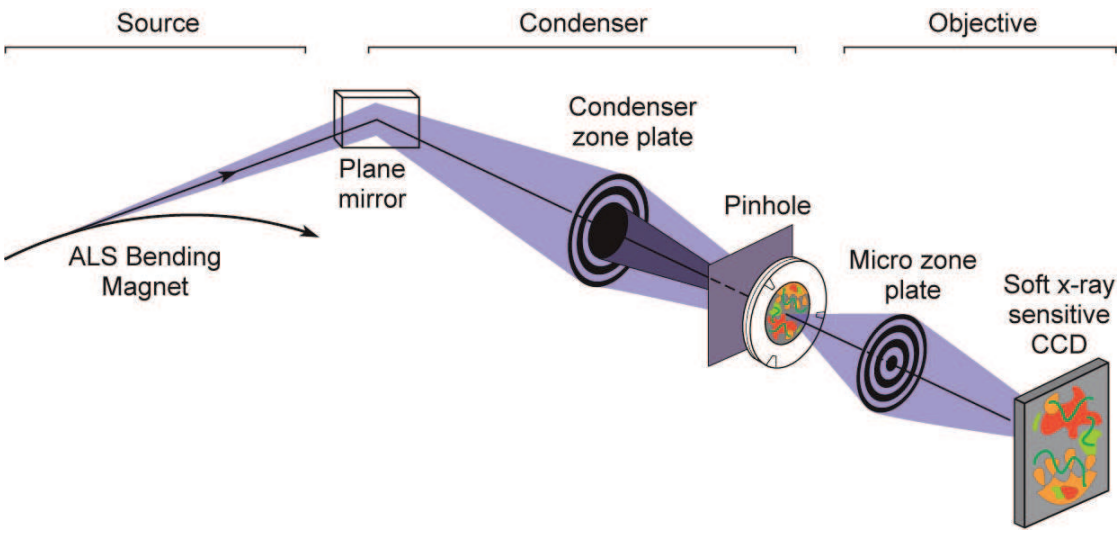

Figure 4.2: Schematic of the full-field X-ray microscope (XM-1) at Beamline 6.1.2 at ALS. From [90].

Scanning Transmission X-ray Microscope at ALS Beamline 11.0.2 (STXM)

The STXM station operates in a different way than the XM-1. Its schematic is shown in Fig. 4.3. Only one Fresnel zone plate is used. The X-ray photons from the storage ring are first monochromated by the monochromator. A spatial filter is used to enhance the coherence of the beam to improve the subsequent focusing. The Fresnel zone plate focuses the X-ray beam onto a diffraction limited spot on the sample. The transmitted photons through the sample spot are then detected by an Avalanche Photodiodes Detector (APD).

An image of the whole sample is obtained point by point by scanning the sample stage across the area of interest. The stage scan is controlled by piezoelectric motors and monitored by a laser interferometer with closed-loop feedback. This allows the stage position to be accurately controlled with high stability. A spatial resolution of 25 nm can be achieved by the current zone plate used for regular user operation, similar to that in the XM-1. The time

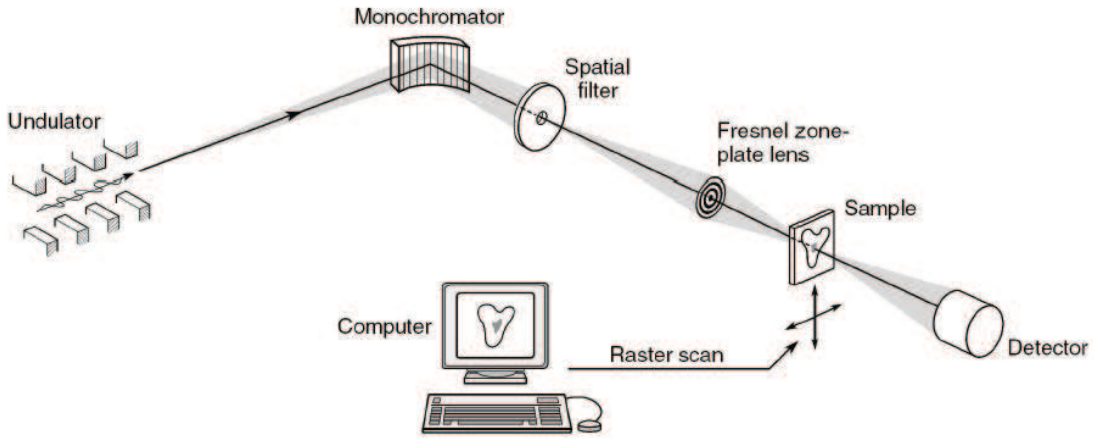

Figure 4.3: Schematic of the scanning transmission X-ray microscope (STXM) at Beamline 11.0.2 at ALS. From [91].

resolution is 70 ps, the same as the XM-1, as it is determined by the storage ring. The APD detector has a very fast response to the X-ray photon so that with an appropriate triggering mechanism time-resolved experiments can be performed, which I will describe later.

4.1.3 Motivation to Image the Magnetic Normal Modes

As mentioned above, the purpose of performing X-ray microscopy experiments on spin transfer samples is to understand the micromagnetic behavior of the spin-transfer-driven magnetic dynamics in a nanomagnet. The Stohr group at Stanford University has pioneered studies along this direction. In their pump-probe experiments ([64–67]), switching is initiated by a square current pulse and the micromagnetic configuration during switching is imaged by STXM at different time delays relative to the pulse onset. However, a square pulse is quite complicated for studying the spin-transfer-driven magnetic dynamics, because the switching dynamics involve multiple dynamical modes. In addition,

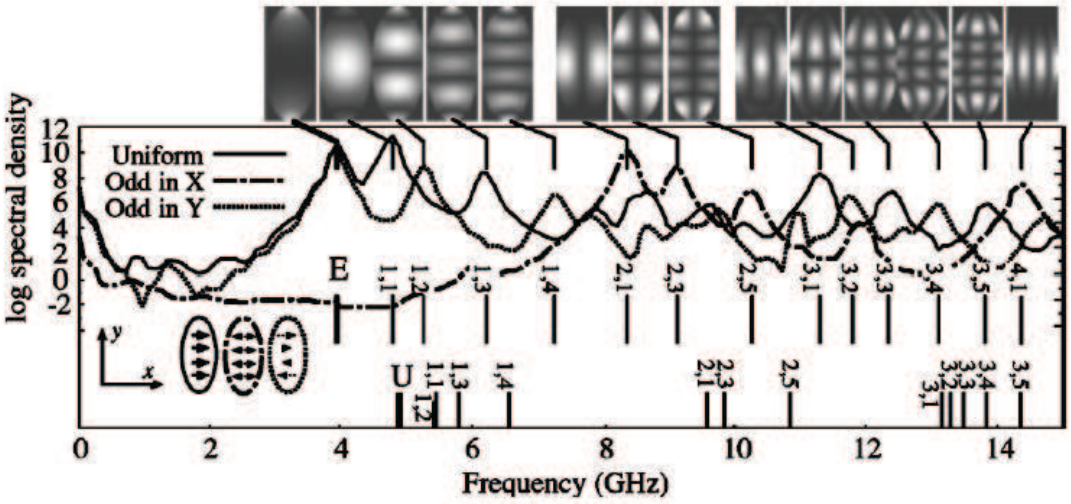

Figure 4.4: Example of micromagnetic simulation results of magnetic normal modes. Eigenmode images (top) and spatially averaged power spectra (middle) for a 160 nm × 350 nm × 5 nm ellipse of Permalloy in zero applied field. From [92]

the dynamics are not repeatable under excitation of a square pulse due to thermal fluctuations. In X-ray experiments, accumulation of photon counts are necessary to achieve enough signal-to-noise ratio, so the results must be averages of many switching events and therefore cannot reveal many important features.

In our experiments, we take a different approach to study the dynamics, by exciting and imaging the magnetic normal modes. Magnetic normal modes serve as the basis for linear dynamics at small amplitude, and are also helpful in understanding the nonlinear dynamics at large amplitude that can lead to switching and large angle oscillation. Reference [92] calculates the magnetic normal modes for a thin ellipse device. As shown in Fig. 4.4, normal modes of different structures have different frequencies and symmetries. Recent implementation of spin-transfer-driven ferromagnetic resonance (ST-FMR) ([18, 21, 58, 59]) provides a powerful tool to study the magnetic normal modes.

Using ST-FMR, we apply continuous RF current at the normal-mode resonant frequency. In this way, individual normal mode can be resonantly excited and isolated from other modes. Since the X-ray probe pulses come in a periodic pattern, we can lock the RF excitation frequency to the X-ray clock frequency so that thermal fluctuation issues can be avoided. By timing the X-ray detection to coincide with different phases of the RF excitation, the full amplitude and phase response of the magnetic normal modes can be measured. In this way, the spatial configuration and time-evolution of the normal mode and its phase relationship with the RF drive can be mapped out, and compared with theoretical models. The elemental sensitivity of XMCD will allow a definitive identification of which normal modes are associated with which magnetic layer, and to what extent there is coupling between the two layers, a crucial issue in spin-transfer-driven dynamics.

4.2 Experimental Methods

4.2.1 Device Information

We fabricate two types of devices: type I samples have the structure $Ni_{81}Fe_{19}$ 40 nm / Cu 6 nm / $Co_{90}Fe_{10}$ 15 nm, and type II samples have the structure $Ni_{81}Fe_{19}$ 15 nm / Cu 4 nm / $Co_{84}Fe_{16}$ 5 nm.

The free ($Co_{90}Fe_{10}$) and fixed ($Ni_{81}Fe_{19}$) layers are made of different ferromagnetic materials so that we can utilize the elemental sensitivity of XMCD to isolate the signal from the particular layer of interest and study its dynamics. This will also further allow us to study to what extent there is coupling between

the two layers. In each layer, the ferromagnetic alloy has richer composition of one magnetic material so as to maximize the XMCD signal, and we choose CoFe rather than NiFe to be the free layer material because Co provides stronger XMCD contrast than Ni. In our experiment, we will image at the Co L_3 edge (E = 778 eV).

Type I samples have a thicker-than-normal free layer (15 nm of CoFe) to provide strong enough signal to be imaged by both XM-1 and STXM for initial experiments. In this type of sample, the importance of the Oersted field is expected to increase relative to the spin torque since the size of the spin torque is independent of free layer thickness, while the torque due to the Oersted field scales $\propto$ thickness. We eventually aim to study the dynamics of 5 nm CoFe free layers, which will allow us to image the fundamental magnetic modes excited almost purely by spin torque, without significant interference from Oersted-field effects, and to make direct connection to previous electrical experiments on spin-torque nanopillars, all of which have used thin ($\leq$ 5 nm) free layers.

In both types of samples, the top free layers and the Cu spacer layers are patterned into an elliptical cross section of 100×200 nm^2 (see Fig. 4.5(a)), while the bottom fixed layers are left unpatterned on the scale of 20 μm. It will become clear later why we want to leave the fixed layer extended. The samples are fabricated on thin Si_3N_4 membranes for x-ray transmission measurements (see Fig. 4.5(b)). Details about the fabrication process can be found in the appendix of this chapter.

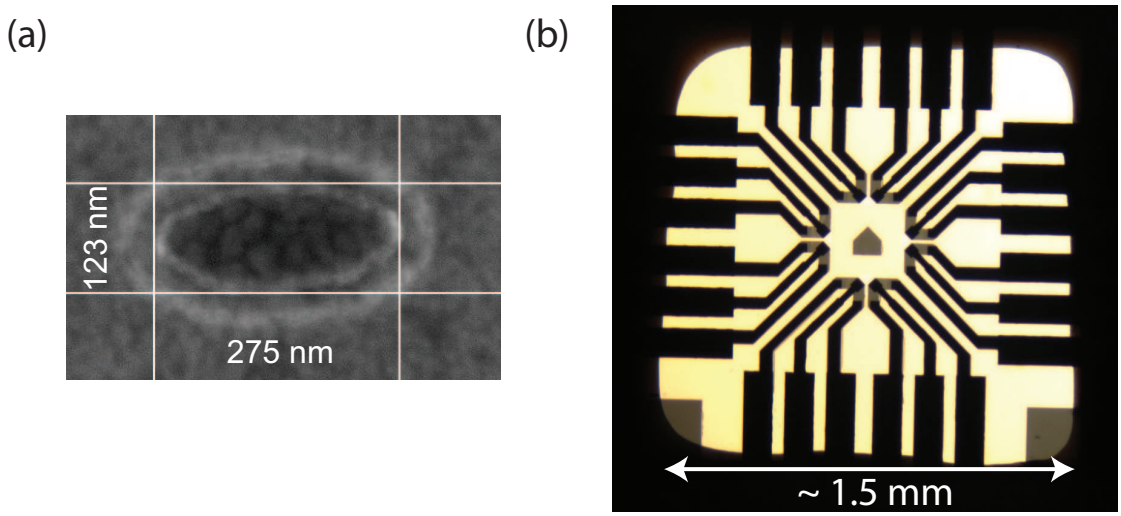

Figure 4.5: (a) SEM image of the nanopillar after ion mill etching and lift-off of HSQ resist. (b) Image of the devices on Si_3N_4 membrane taken by a light microscope in transmission mode.

4.2.2 Setup for Dynamics Measurements

Considerations for the Sample Arrangement

As mentioned in the introduction section, XMCD is only sensitive to the magnetization component along the photon helicity direction (the same as the beam direction). For thin film samples of the ferromagnetic materials used in our experiment (CoFe and NiFe), the magnetization precession will be confined mostly within the plane of the film due to large out-of-plane demagnetization factors. Therefore in order to image the in-plane magnetization, normal practice is to rotate the sample plane by 30° from X-ray normal incidence, as shown in Fig. 4.6. (We define this rotation axis to be the *x*-axis and beam direction to be the *z*-axis. The *y*-axis is normal to both the *x*- and the *z*- axes. The *y*′-axis is in the sample plane and normal to the *x*-axis.) Furthermore, we would like to arrange the sample in a way so that when the magnetic precession is excited, the precession trajectory will have a component projected along the *z*-axis,

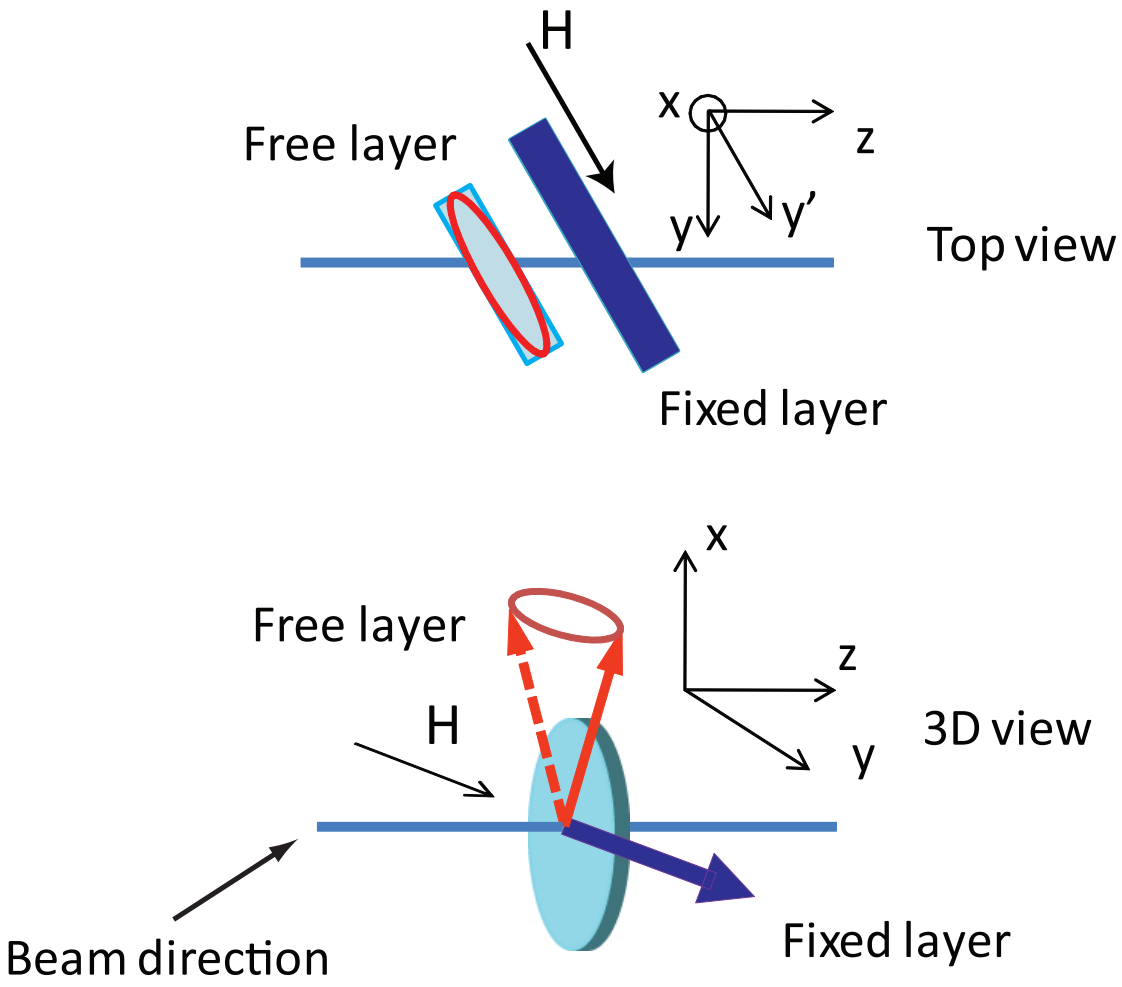

Figure 4.6: Schematics of the sample setup. (a) top view. (b) 3D view.

which will allow us to detect the magnetic contrast corresponding to different phases of the precession. This suggests that the precession axis (usually also the equilibrium direction of the free layer) be aligned as close as possible to the *x*-axis. The fixed layer will be preferentially aligned perpendicularly to the free layer, i.e. along the *y'*-axis, in order to provide the maximal spin torque efficiency.

One restriction for both XM-1 and STXM is that the magnetic field can only be applied in the *y'*-axis direction due to space limitation in the equipment

setup. Considering all these preferences and restrictions, we align our sample in the way shown in Fig. 4.6. The long axis of the ellipse is aligned along the x-axis so that shape anisotropy will try to keep the free layer along this direction. This then limits the magnitude of the magnetic field we can apply along the y'-axis because strong field will rotate the free layer moment away from the x-axis which will decrease the XMCD contrast signal. So we can only apply small field to saturate the fixed layer along the y'-axis. This is primarily why we choose the fixed layer to be extended so that it has a very small coercive field and can be saturated by small fields.

Time-resolved Setup

To perform the time-resolved experiment, the RF-drive frequency needs to be phase locked to the X-ray clock so that the X-ray pulses are synchronized to the magnetic precession. The X-ray pulse repetition rate is 500 MHz. The RF-drive frequency is in the GHz range, so in order to synchronize to the X-ray clock, the RF-drive frequency can only be integer or fractional harmonics of the X-ray clock frequency. This can be accomplished using a Phase Locked Loop (PLL) circuit shown in Fig. 4.7. In this circuit, a Voltage Controlled Oscillator (VCO) is used to generate RF signal of desired frequency, f_{RF}. This signal is then frequency-divided down by a ratio, M, to a value close to the X-ray clock frequency f_{clock}. The phase detector takes f_{RF}/M and f_{clock} as inputs and then outputs a tuning voltage, V_{Tune}, which is fed back to the VCO. When the circuit reaches a stable condition, the following relationship holds

$$f_{clock} = f_{RF}/M \tag{4.2}$$

where M = integer for XM-1 and M = integer + 1/8 for STXM.

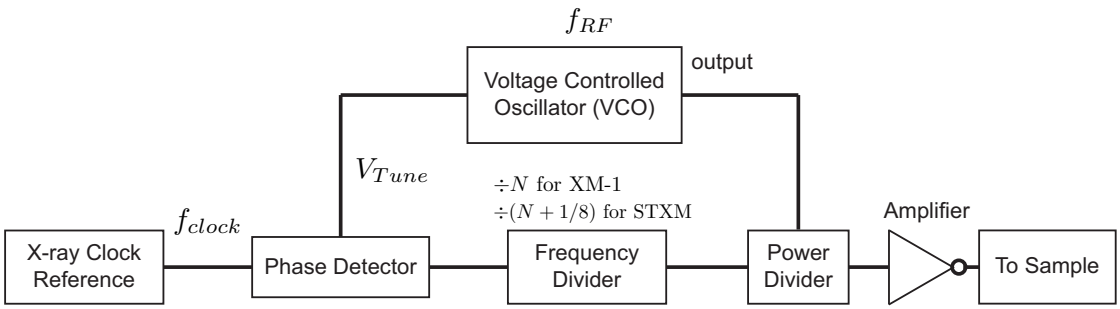

Figure 4.7: Circuit diagram for synchronization of RF-drive frequency to the X-ray clock frequency.

On XM-1, the image is recorded by a CCD camera. To perform time-resolved imaging with continuous RF excitation, we need to set up the synchronization so that every X-ray pulse corresponds to the same oscillation phase. This is illustrated in Fig. 4.8(a). Therefore, f_{RF} needs to be an integer harmonic of the f_{clock}. The relative phase can be tuned through a digital delay line. (See appendix of this chapter for more details)

On STXM, the APD detector has a very fast response to the X-ray photons. With proper triggering mechanism, multiple channels can be recorded via up to 16 counters. We can utilize this feature to use different counters to record signals corresponding to different RF phases. This can be done by setting the RF frequency to be a fractional harmonics of the clock frequency. In our experiment, we use 8 counters, so the fractional value should be an integer plus $1/8$. (See the appendix section of this chapter for more details)

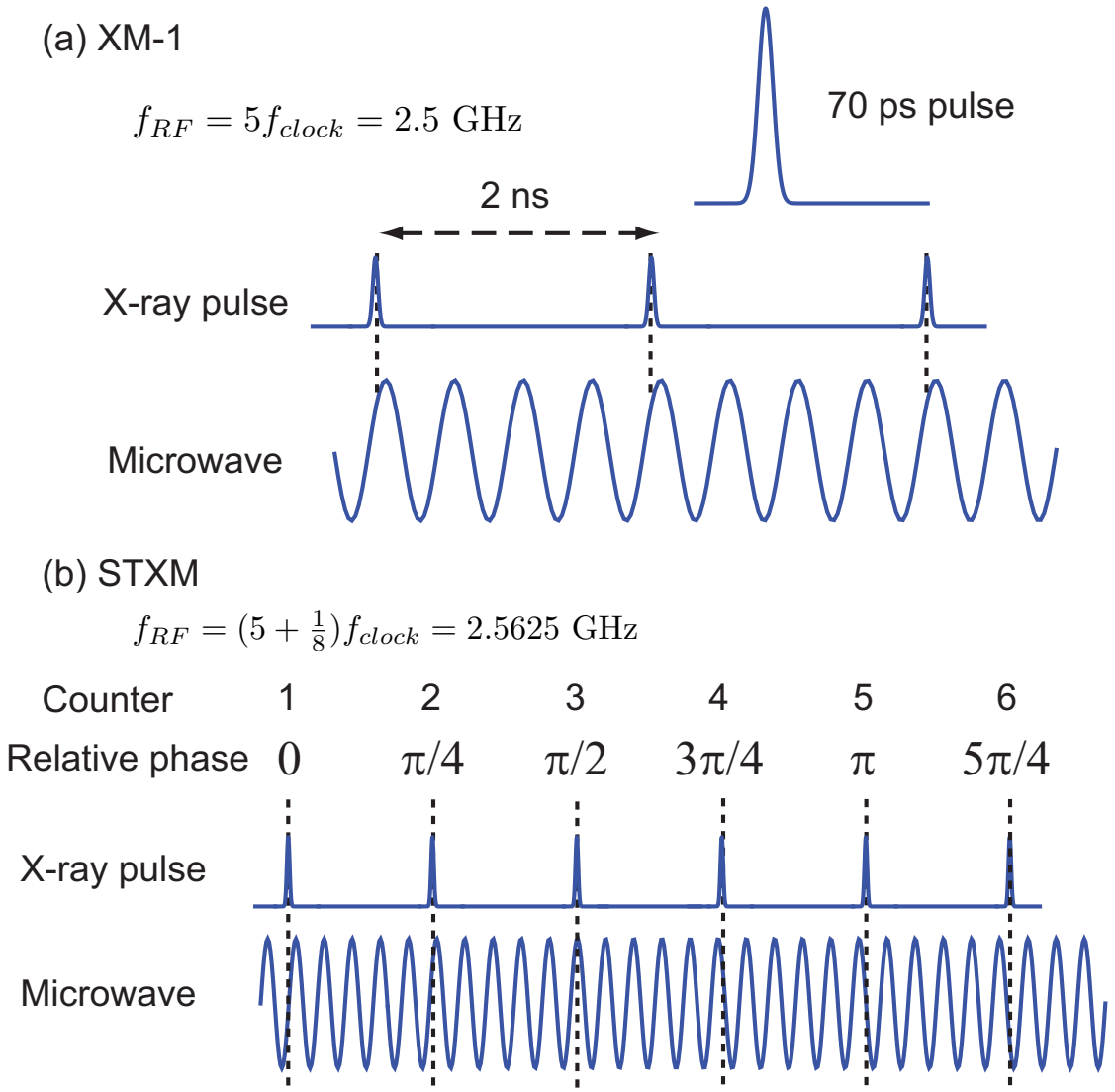

Figure 4.8: Synchronization of the pulse pattern (f_{RF} = 500 MHz) and the continuous RF drive (f_{clock} ~ 2500 MHz) for (a) XM-1 and (b) STXM.

4.3 Preliminary Measurement Results and Discussion

4.3.1 Electrical Characterization

We first characterize each device using electrical measurements to identify the frequencies of the normal modes. Figure 4.9 shows a resistance vs. magnetic

field scan taken at a field along the easy axis direction for a type I device. The switchings around zero field correspond switching of the extended fixed layer. This suggests that the fixed layer can be saturated along the field direction at small field strength. The coercive field of the free layer is about 130 Oe. A field scan perpendicular to the easy axis is shown in Fig. 4.9(b). In this geometry, the fixed layer always follows the field direction so that the maximum relative angle between the free and fixed layer is 90° at field close to zero. In the X-ray microscope setup, this is the geometry for applying magnetic field (refer to Fig. 4.6 for the sample orientation). Therefore, we are limited to the low field region to perform X-ray imaging experiment due to a few reasons. First, at low fields, the free layer moment is close to the easy axis direction (the *x*-axis) so its magnetic precession will have a large component projected along the beam direction (the *z*-axis), giving a relatively strong XMCD contrast. Secondly, the fixed layer is along the *y*'-axis field direction so the relative angle between two layers is close to 90° which gives a large spin torque efficiency. Third, at low fields, the frequency of the normal modes will be low so that we can have better relative time resolution given the fixed 70 ps X-ray pulse width.

ST-FMR spectra as a function of frequency and field are shown in Fig. 4.10. The spectra are quite symmetric about field direction. Below about 2.5 GHz, there is only one single peak. Above 2.5 GHz, this single peak splits into two branches: the one with lower frequency saturates to about 3.5 GHz at 300 Oe, and the one with higher frequency saturates to about 5.5 GHz at 300 Oe. Both branches bend down in frequency at high field (> 350 Oe).

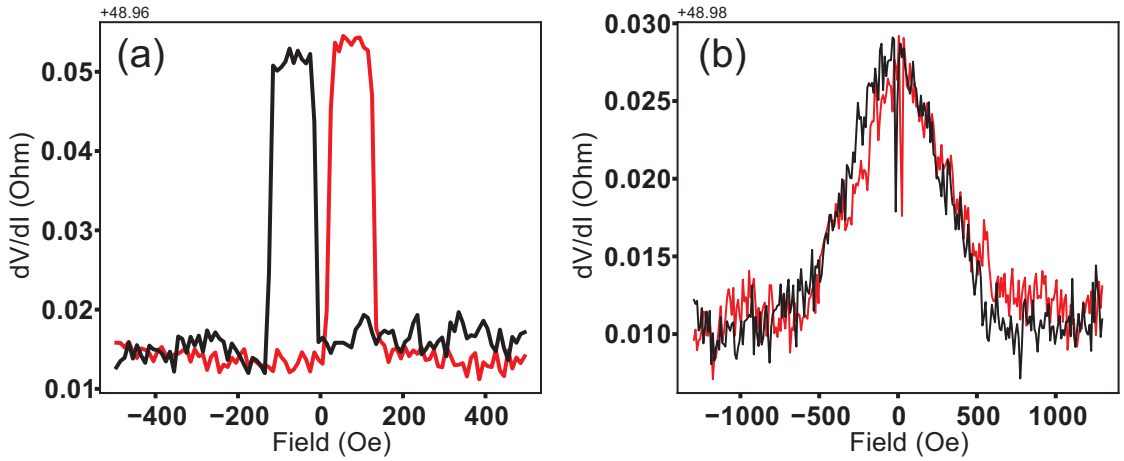

Figure 4.9: Resistance vs. magnetic field curves for a type I device imaged at XM-1 taken at (a) a field along easy axis and (b) a field perpendicular to easy axis.

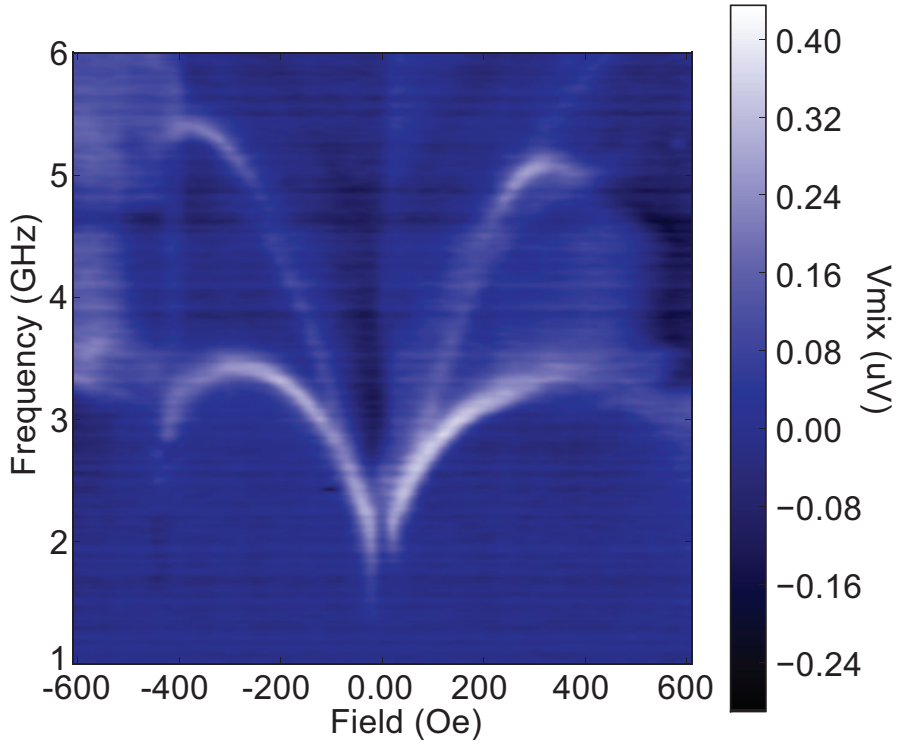

Figure 4.10: ST-FMR spectra as a function of frequency and magnetic field.

4.3.2 XM-1 Measurements

Static Images

For X-ray imaging, the sample is mounted on the setup according to Fig. 4.6. We apply a magnetic field of different strength along the y'-axis to form different offset angles of the free layer, and then image the static configurations of the free layer. This allows us to determine the data accumulation time needed to achieve enough signal-to-noise ratio to resolve the weak contrast expected for the dynamics measurement.

The results are summarized in Fig. 4.11. The contrast images are computed in reference to the image taken at $H = -700$ Oe where the free layer is saturated along $-y'$ direction. Figure 4.11(a) shows the contrast images at field values from 700 Oe to -200 Oe, and the averaged contrast is plotted as a function of field in Fig. 4.11(b). The maximal contrast (between H=700 Oe and 700 Oe) is about 5%. As a function of field, the average contrast shows an approximately linear behavior from -700 Oe to + 700 Oe, which is what we expected from the GMR curve (Fig. 4.9(b)) that the free layer moment saturates to the 90° direction roughly at $H = \pm 700$ Oe. The overall RMS noise in the background (the area outside the pillar where no magnetic contrast is expected) is around 1%. The accumulation time is about 400 sec per image. This gives us a rough idea about the accumulation time needed to image the dynamics.

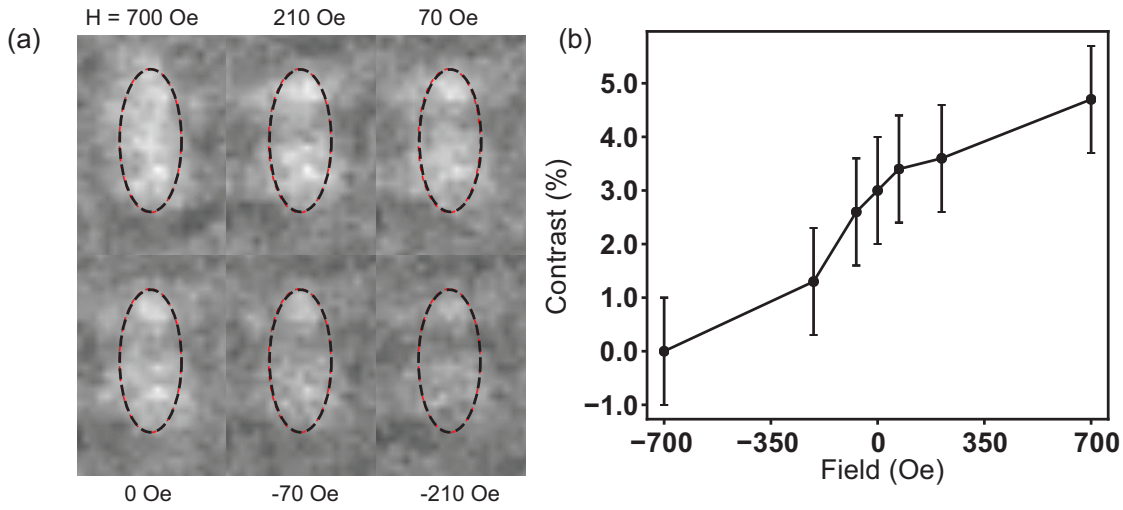

Figure 4.11: (a) Magnetic contrast images at different field strengths. The grayscale is 0.9 (black) to 1.1 (white). Dotted ellipses indicate the position of the pillar. (b) Averaged magnetic contrast inside the pillar as a function of field.

Dynamics Measurement

We then perform time-resolved imaging on the same sample as in Fig. 4.10. We first focus on the low frequency dynamics at $f = 2.5$ GHz (period $T = 400$ ps) at $H = -50$ Oe. We obtain 10 images at time delays in steps of 40 ps ($\Delta t = T/10$). The contrast images are calculated by using the average image of these 10 images as the reference. The results are shown in Fig. 4.12. The images show a contrast transition from dark at 0 ps delay to bright at 200 ps and back to dark again at 360 ps, corresponding to one period of precession.

To further demonstrate the oscillation feature, we plot the average contrast inside pillar as a function of relative delay in Fig. 4.13 for both $H = -50$ Oe and 50 Oe. At both fields, the magnetic contrast shows an oscillatory behavior and this behavior is opposite in delay (phase) when field is reversed. This symmetry can be understood as illustrated by the cartoons in Fig. 4.13. When the magnetic field is reversed, the fixed layer also reverses to follow the field

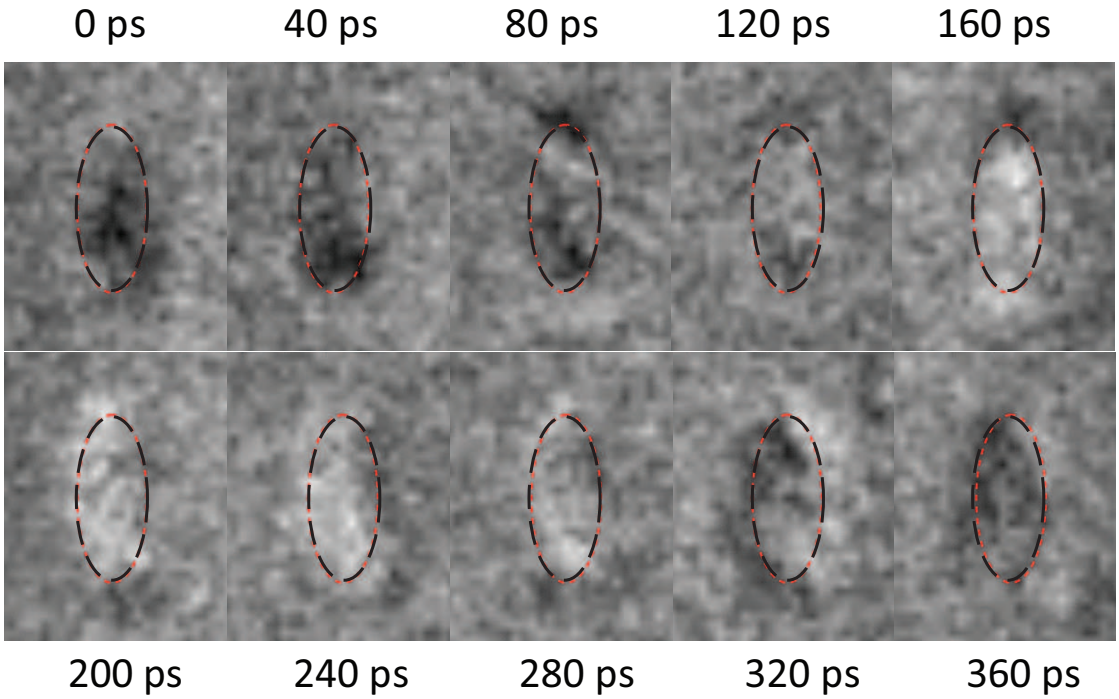

Figure 4.12: The magnetic contrast images at different relative time delays for excitation frequency of 2.5 GHz and magnetic field H= -50 Oe.

direction. The spin torque on the free layer produced at the same phase of the RF excitation will also change its direction. This results in a π phase shift in the free layer precession at resonance, which is then reflected in the magnetic contrast. This feature, in fact, gives us a confirmation that the dynamics we see in the contrast images are primarily excited by spin torque from the RF drive rather than the Oersted field because the Oersted field would not change its direction depending on the direction of the fixed layer.

Issues with XM-1 Measurements

The results above demonstrate the performance of the phase-resolved detection with X-ray microscopy measurements and confirm the type of dynamics excited in the magnetic layer. However, drawing an unambiguous conclusion about the

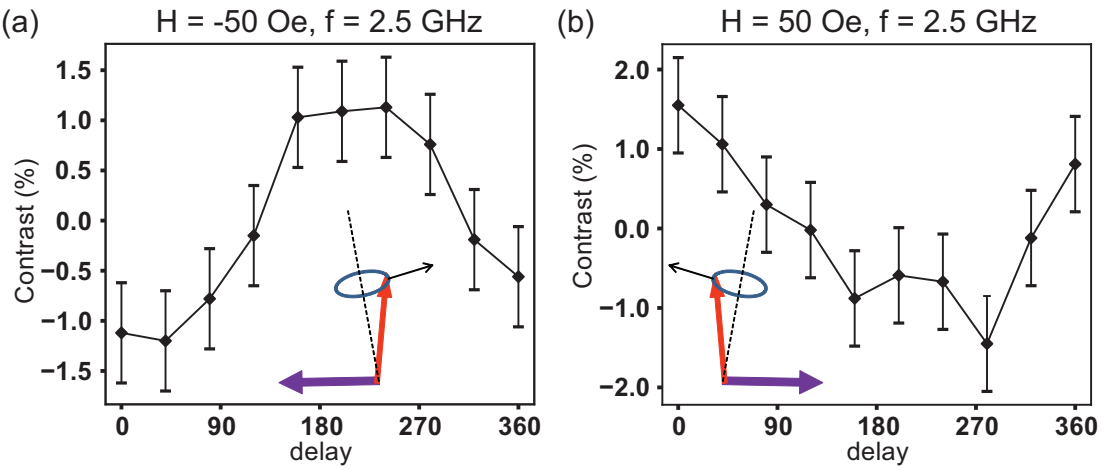

Figure 4.13: The average magnetic contrast as a function of relative delay at excitation frequency of 2.5 GHz for (a) H=-50 Oe and (b) H= 50 Oe.

uniformity of the magnetic dynamics in detail has been difficult due to the low signal-to-noise ratio. In Fig. 4.12, the fluctuations in the background are clearly visible, and the RMS value of the noise (~1%) is comparable to the signal level we observe (see Fig. 4.13). The low signal-to-noise performance is due to the full field nature of the XM-1 microscope. In XM-1, the incoming X-ray photons are distributed in a large area of about 10×10 μm^2, while our device is only about 100×250 nm^2 in size. The photons available for imaging the device are only a tiny fraction (less than 1%). To achieve enough photon counts requires long accummulation time. The stability of the device position and X-ray illumination (due to the stability of the X-ray optics in the microscope) will then become a problem. For the results above, the total accummulation time is about 2-3 hours. We do observe that the sample position shifts during the course of the measurements. We must thus take images at the same experiment conditions multiple times with each image having a short exposure time (~ 1 min), and numerically align these images afterwards to get the final image. This helps compensate the device position shift, but the signal-to-noise level achieved is still limited.

4.3.3 STXM Measurements

On STXM, all the incident X-ray photons are focused onto a small spot, which allows a better signal-to-noise performance. The scanning required to complete an image could take a long time for imaging large area samples, but it is not an issue for small samples like our devices. So STXM should be able to provide better quality data on our measurements.

Electrical Characterization

We study another type I device with STXM. This device has a similar behavior in DC and ST-FMR measurements to the one studied with XM-1 (see Fig. 4.14 for the summary of the electrical characterization for this device).

Dynamics Measurement

For dynamics measurement, we again first focus on the low frequency mode at 2.5625 GHz ($f_{RF} = (5 + 1/8) f_{clock}$). On STXM, we use 8 counters to record images corresponding to 8 different phases. When processing the image, we calculate the contrast by dividing two images that have a π phase shift, as illustrated in Fig. 4.15(a).[1] The STXM data have a better signal-to-noise ratio as expected. We can clearly see the spatial non-uniformity above the background noise level inside the pillar. At 2.5625 GHz, for H = -50 Oe (mode A), the lower right edge of the device precesses at a different phase and amplitude than the center of the device. For H = 50 Oe (mode B), the contrast around the center of the device is

[1] Here the values for the 8 phases shown in Fig. 4.15(a) are arbitrarily chosen, and do not represent the actual phases.

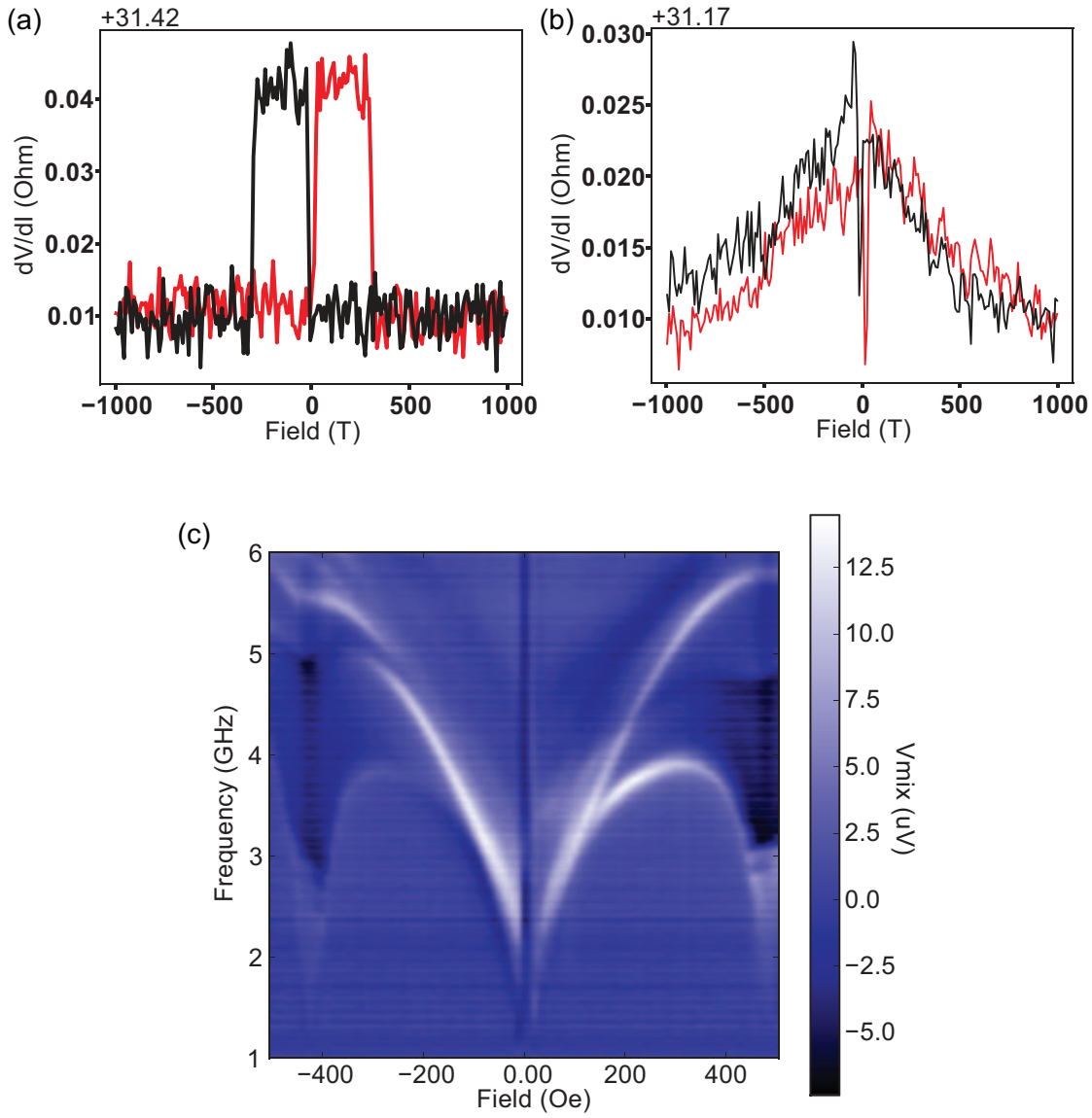

Figure 4.14: Electrical characterization of a type I device measured at STXM. (a,b) Resistance vs. magnetic field curves taken for (a) a field along easy axis and (b) a field perpendicular to easy axis. (c) ST-FMR spectra as a function of frequency and magnetic field. V_{mix} is measured after a transformer with ratio 1:100.

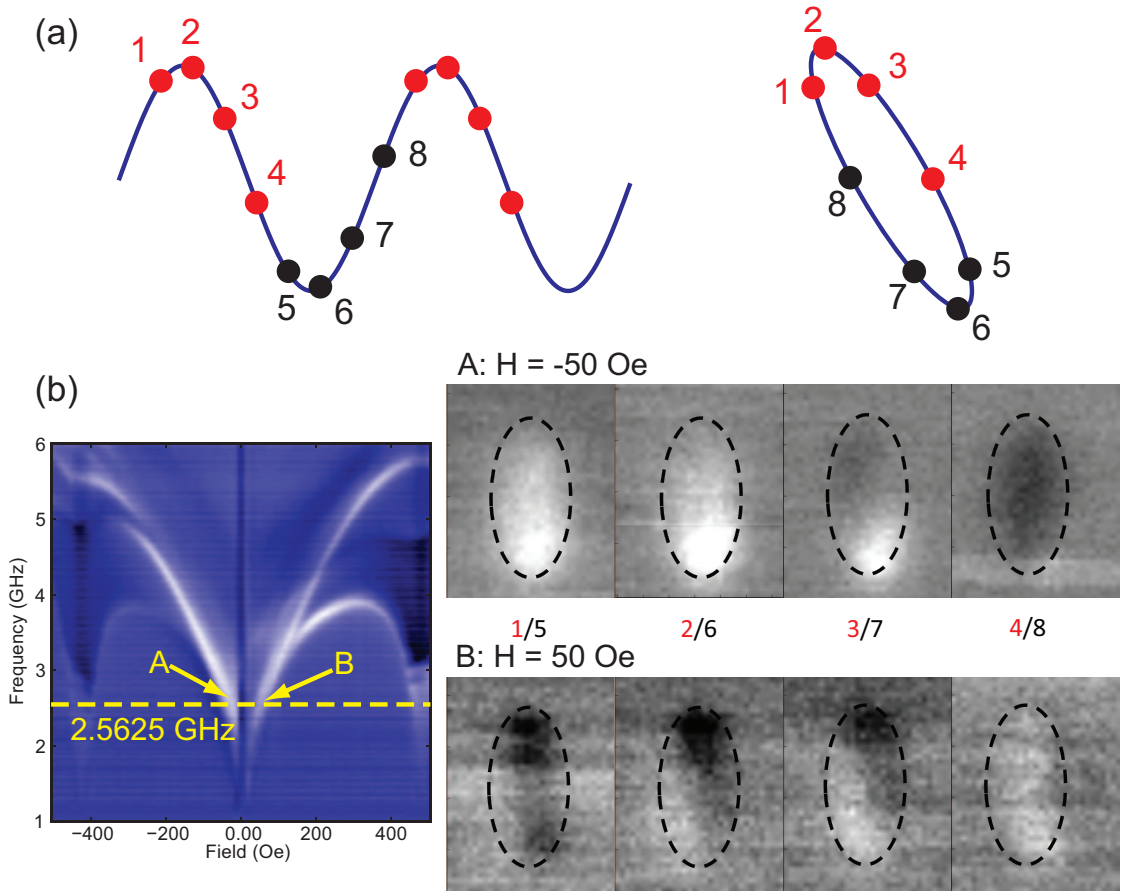

Figure 4.15: (a) Illustration of the 8 phases recorded in STXM experiments. (b) Magnetic contrast images at 2.5625 GHz taken at A: H = -50 Oe and B: H = 50 Oe as indicated in the ST-FMR spectra color plot.

reversed due to reversal of the fixed layer moment, similar to what we have seen in the XM-1 experiments. However, now the upper right edge of the device has a different phase and amplitude, corresponding to the lower right edge in the H = -50 Oe case. This cannot be explained only by considering the reversal of the fixed layer because the reversal of the fixed layer is along the short axis of the ellipse so it should not produce any change along the long axis direction. This behavior may be related to detailed coupling between the edge and the center of the device, and also effects of the Oersted field from the RF current.

We also studied the modes at a higher frequency 3.5625 GHz (f_{RF} = (7 +

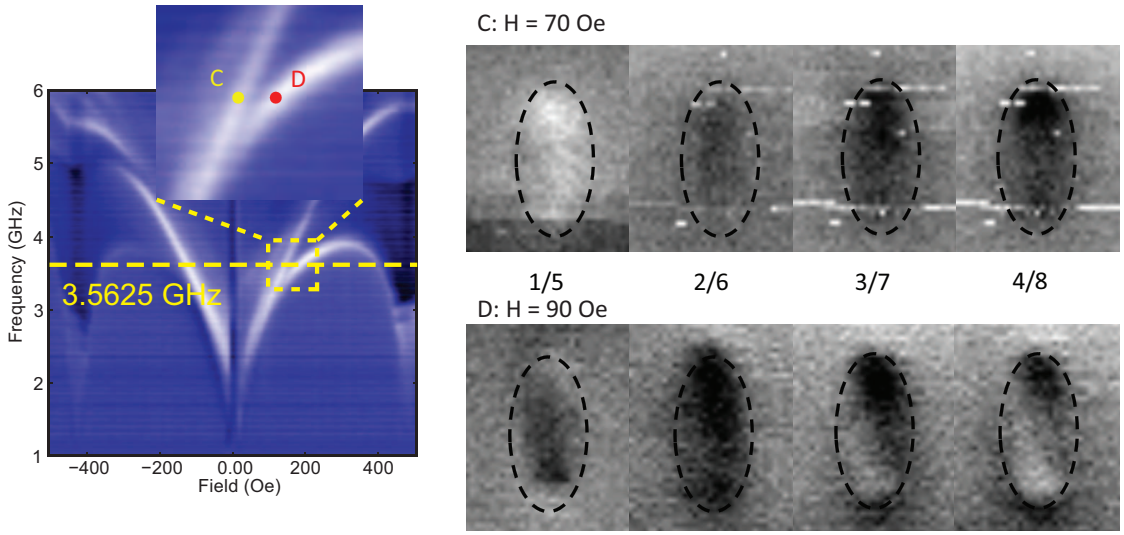

Figure 4.16: Magnetic contrast images at 3.5625 GHz taken at C: H = 70 Oe and D: H = 90 Oe as indicated in zoom-in of the ST-FMR spectra color plot.

1/8)f_{clock}) where the single low frequency mode starts to split into two branches. We attempted to image each of the branches by tuning the field strength. At H = 70 Oe, the mode (C) corresponds to the higher-frequency branch, while the mode at H = 90 Oe (D) corresponds to the lower-frequency branch. The magnetic contrast images are shown in Fig. 4.16. For mode C, the contrast around the upper edge of the device is greater than the center of the device, indicating that the upper edge has a larger precession amplitude. But they have the same behavior as a function of the RF phase, indicating both parts precess at the same phase relative to the RF drive. For mode D, the overall contrast change is also greater around the upper edge than around the center, but the phase dependence is different, indicating that the two regions precess at a different relative phase.

Comparing the mode structures at 3.5625 GHz to those at 2.5625 GHz, it suggests that the upper branch in the ST-FMR spectra is spatially more uniform than the lower branch. This is similar to the simulation results in Ref. [92] that

the lowest frequency mode corresponds to motion near the ends of the ellipse, though in our results the two ends are not symmetric in dynamics behavior. The Oersted field very likely plays a role in the symmetry breaking. At frequency below about 3 GHz, the two branches are close in frequency, and the dynamics would be a combination of both the uniform mode and the non-uniform mode. The fact we clearly see the non-uniformity in the 2.5625 GHz images indicates that the non-uniform mode has a greater weight than the uniform mode.

4.3.4 Discussions and Future Plan

These results demonstrate the ability of the X-ray microscopy in studying the magnetic dynamics in a nanoscale magnet. Further experiments and analyses are needed to investigate the nature of the spin-transfer-driven magnetic normal modes.

First of all, micromagnetics simulations are necessary to understand the details of the magnetic modes observed. The Oersted field effect needs to be carefully modeled. The devices studied so far have a free layer thickness of 15 nm, thicker than previous spin transfer experiments ($\leq$ 5 nm), for the purpose of obtaining a stronger XMCD signal. For such a thick free layer, it is not safe to apply our previous understanding about spin-transfer-driven dynamics directly to this experiment. In particular, a thicker layer requires more current to excite the dynamics via spin transfer and the Oersted field effect becomes more important. Plus, in the initial experiments, a large RF power is used to excite the magnetic precession into a large-angle region so as to provide stronger magnetic contrast between different precession phases. This results in an even

larger Oersted field, and the magnetic dynamics may also go beyond the linear small-angle region so that nonlinearity needs to be considered. Furthermore, the Oersted field from the RF current generates ac torque at the same resonance frequency. The magnetic dynamics is driven by the combination of resonant spin torque and Oersted field torque. The resulting dynamics behavior should therefore be different than what we have learned based on thinner layer devices. One other factor is that for such thickness, the free layer may not be considered as a simple 2D layer without considering the variation along the out-of-plane direction, especially around the edge of the ellipse where the magnetization tends to tilt out of plane due to the demagnetization field and tapering of the sidewalls.

Secondly, we would like to study devices with thinner (5 nm) free layer (the type II) devices. We have performed preliminary tests on STXM to examine the signal-to-noise level on type II device. The signal level is large enough for us to measure straightforwardly resonant precessional dynamics driven by spin torque. This will allow us to image the fundamental magnetic modes excited almost purely by spin torque, without significant interference from Oersted-field effects, and to make direct connection to previous electrical experiments on spin-torque nanopillars, all of which have used thin ($\leq$ 5 nm) free layers.

4.4 Appendices

4.4.1 Notes on the Fabrication of Nanopillar Devices on Suspended Silicon Nitride Membranes

For X-ray microscopy measurements, the sample needs to allow X-ray to transmit through the device and the substrate. The X-ray transmission depends exponentially on the sample thickness. The typical transmission distance of soft X-ray in solids is on the order of 100 nm. So the sample substrate needs to be thin and mechanically strong enough to support the device. A general practice is to use low stress silicon nitride membranes.[2] In our experiments, we fabricate devices on silicon wafers with 150 nm of low stress silicon nitride coated on both sides. The silicon underneath the device area is then etched away to suspend the device and the nitride membrane. The fabrication process is modified from our standard nanopillar process [82]. In the following, I will discuss a few considerations for the design of the electrode pattern and the process to form the suspended nitride membrane.

Geometrical Limitations of XM-1

For samples used on the XM-1 microscope, the size of the nitride window should be large enough for clearance relative to the X-ray optics components. A schematic of the optics components in XM-1 is shown in Fig. 4.17. For measurements of the in-plane component of the magnetization, the sample needs to be rotated 30° from the X-ray normal incidence. This rotation poses

[2]The tensile stress should be less than 250 MPa.

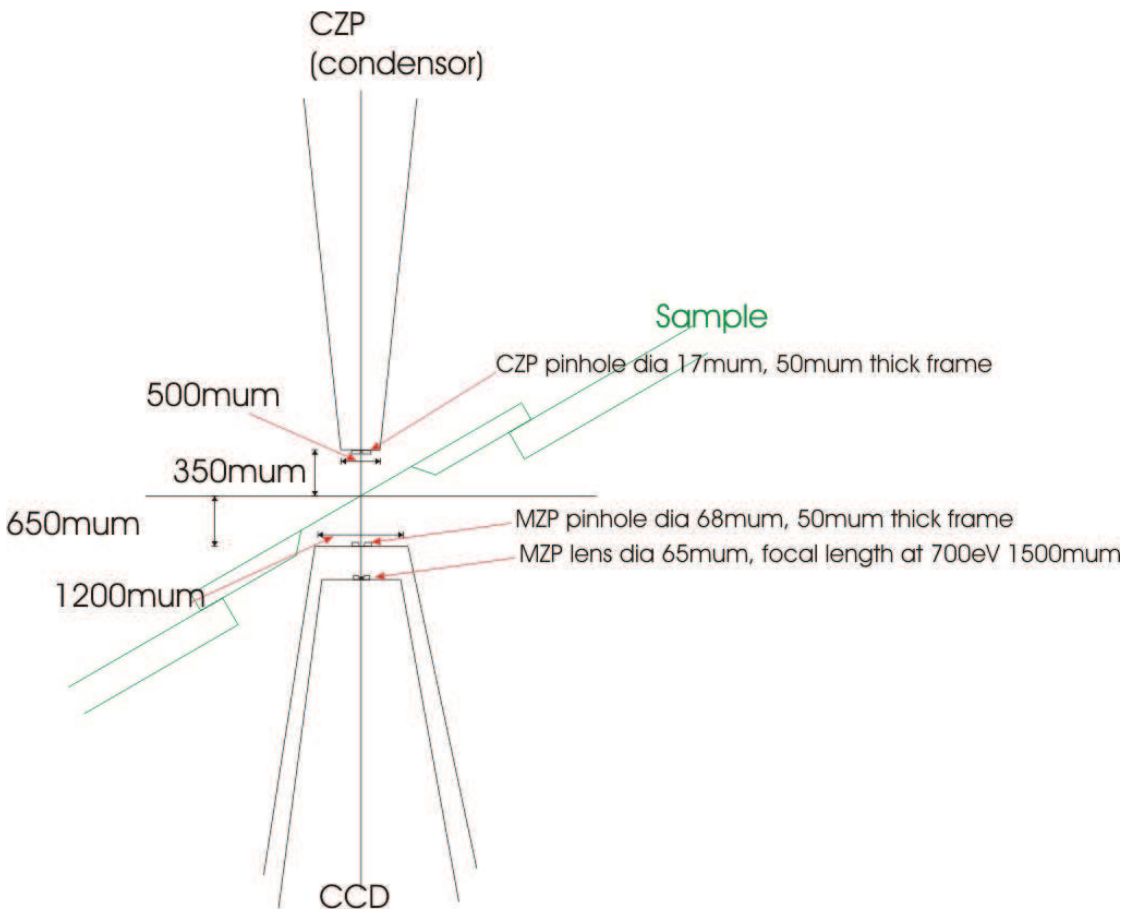

Figure 4.17: The geometry of the XM-1 sample stage. From [93].

a possibility that the sample substrate can hit the X-ray optics. The geometry of the sample stage and the X-ray optics requires that the sample substrate to be thinner than 200 um in a 2 mm by 2 mm area around the device. One option is to use Si wafers thinner than 200 um. But this increases the difficulty of handling during the fabrication and could result in complete loss of the wafer. Another option is to make nitride window of 2 mm by 2 mm in size. The nitride membrane is very fragile, especially at a large size, but the final etching is done on chip-by-chip basis. Careful handling can provide reasonable device yields. So in our fabrications, we make nitride windows of 2 mm by 2 mm in size.

Design of the Electrode Pattern

The individual chip size is 5 mm by 5 mm while the nitride window size is 2 mm by 2mm. It would be difficult to accommodate more than one nitride windows on a single chip. So to allow multiple available devices on a single chip, the devices should be positioned near the center of the chip, and the leads need to extend to near the edge of the chip to allow wire bonding from the sample holder for the microwave signal input. This is different from the electrode pattern in our standard nanopillar devices. So I redesigned the electrode pattern to be compatible with these requirements. Figure 4.18 shows the electrode pattern on a single chip. Eight nanopillars are located on the edges of a 300 μm by 300 μm square centered on the chip. The shifting of the leads as they extend to the chip edge is to align them with the coplanar waveguide on the sample holder which is not centered. This also allows access to probes from all four directions during the electrical test process.

Fabrication Process Using HSQ as the Etch Mask

I developed, with help from Lin Xue, Luqiao Liu, Hsing-wei Tseng and Yun Li, a fabrication process using negative e-beam resist HSQ as the etch mask for the nanopillar. This simplifies the whole process. In particular, we achieve self aligned top electrodes by lifting off the HSQ resist, which allows the top electrode deposition to be done all at once for the whole wafer, instead of processing individual dies in the standard fabrication process. In the following, I will list the major steps of the fabrication process with some discussions on the considerations and requirements for each step.

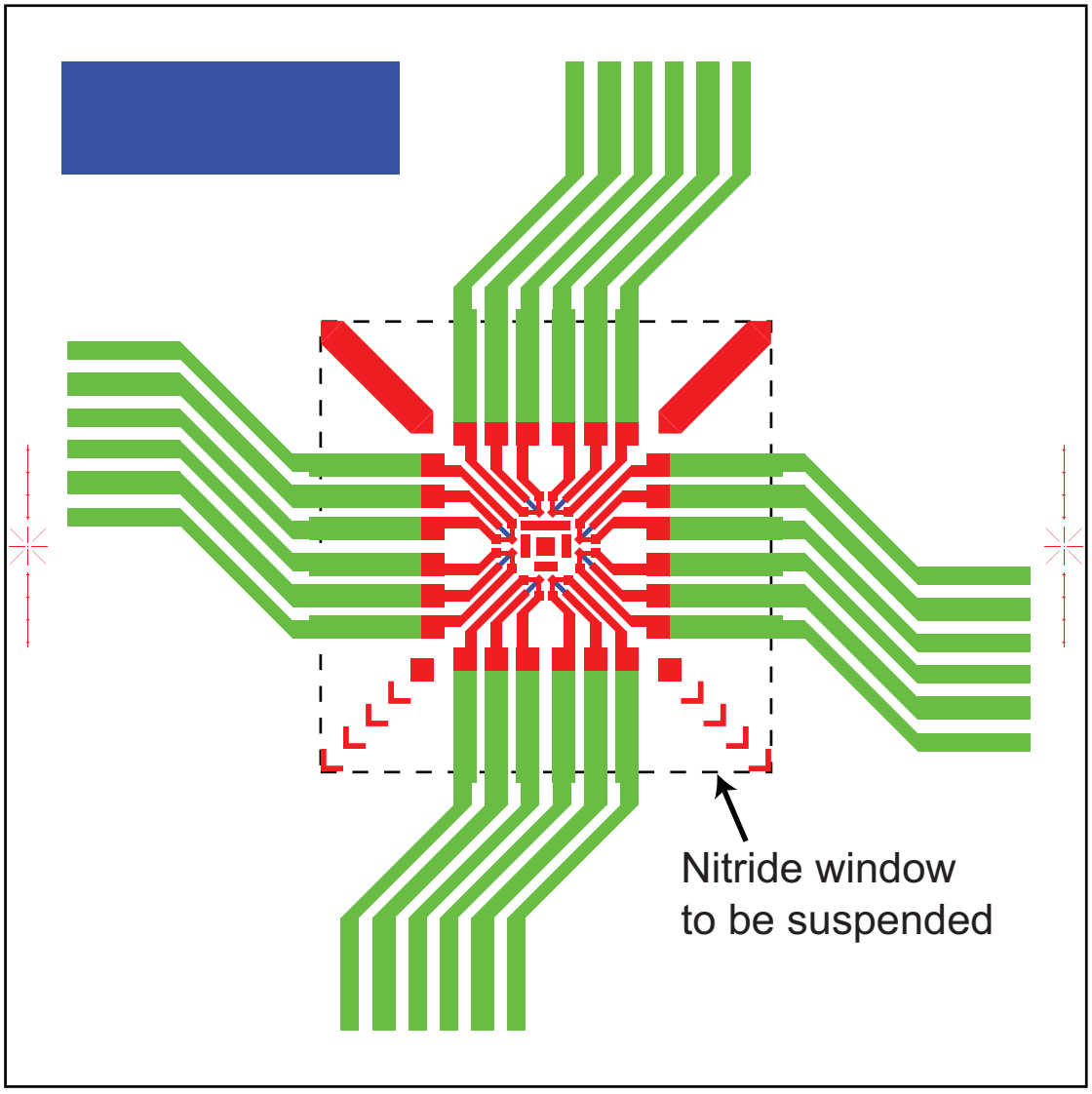

Figure 4.18: The electrode pattern of a single chip. The chip size is 5 mm by 5 mm. The dotted square (2 mm by 2mm) indicate the size of the nitride window to be suspended.

1. Sputter thin film stacks. Use Ru as the capping layer as it provides better adhesion for the HSQ resist layers.

2. Spin HSQ resist.

   (a) Spin Omnicoat at 1500 rpm for 60 sec, then bake for 60 sec at 170°C. Spin a second Omnicoat layer with the same recipe. This bilayer of

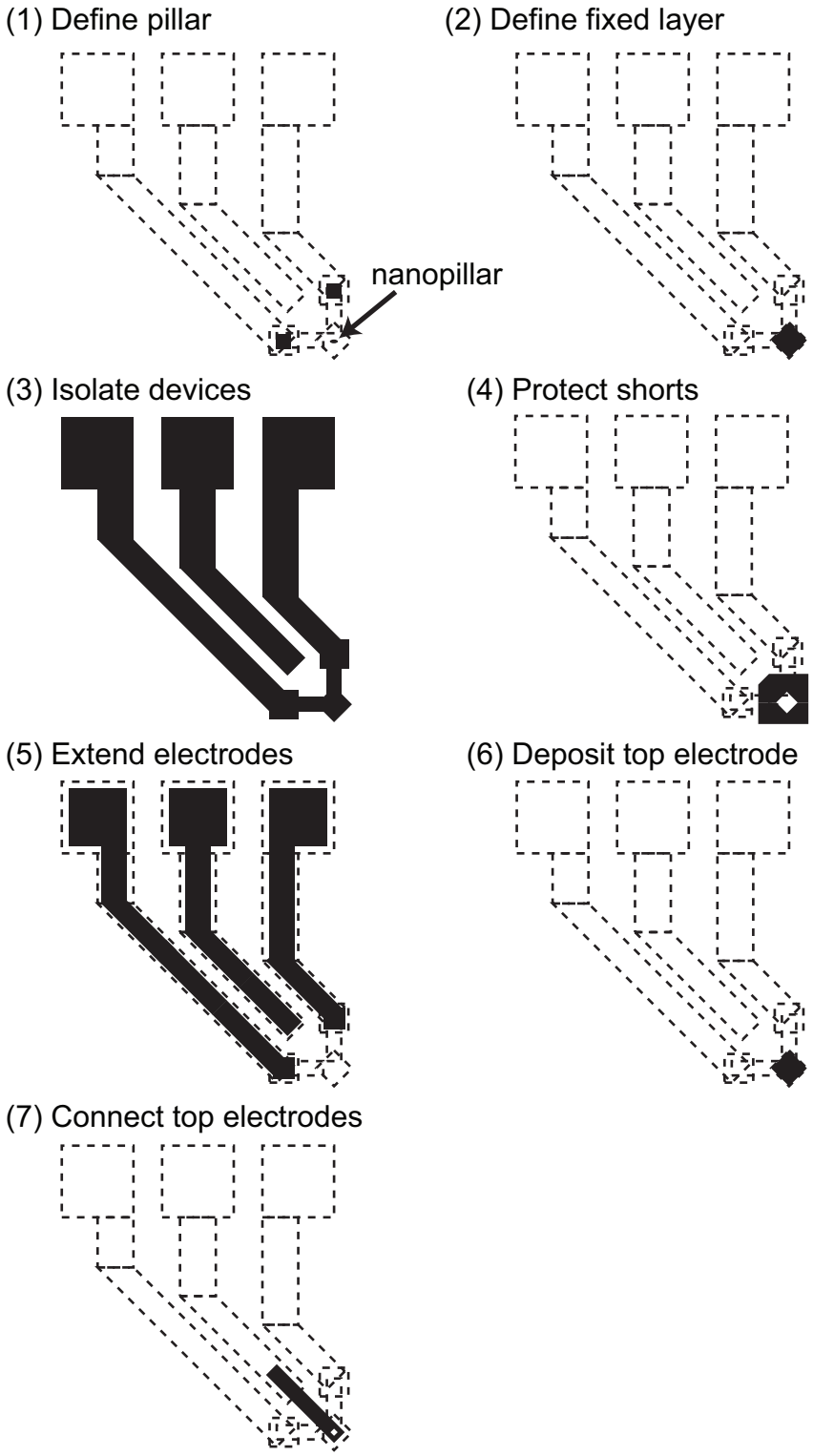

Figure 4.19: Lithography patterns for the HSQ process. For (1)-(3), the black areas are covered by resist. For (4)-(7), the black areas are exposed areas (no resist). The dotted patterns indicate the overall pattern of the device.

Omnicoat is for adhesion.

(b) Spin 2% 495 K PMMA at 4000 rpm for 60 sec, then bake for 15 min at 170°C. This PMMA layer is for lift-off.

(c) Spin 4% HSQ at 3000 rpm for 60 sec, then bake for 1 min at 170°C.

3. E-beam exposure of the nanopillar. E-beam dose used is 3000 $\mu C/cm^2$. Expose two additional pads for electrical contacts, as shown in Fig. 4.19(1).

4. Develop in MIF-300 for 120 sec, then transfer to DI water and blow dry with N_2.

5. Ion-Mill 1: define nanopillar. Use the HSQ resist as the etch mask. Stop etching at the spacer / fixed layer interface by monitoring with the endpoint detector.

6. Immediately after the ion milling, evaporate SiO_2 for a thickness roughly the same as the etch depth. Too much of SiO_2 will result in difficulties in the subsequent lift-off.

7. Lift-off HSQ resist. Ultrasonic the wafer in Remover PG for 60 min. No heating is used. After this step, check the result of the lift-off with SEM. Use the pads to locate the device. If lift-off is successful, the pillar should look like that in Fig. 4.5 with shadows around the edge and low overall contrast.

8. Ion-Mill 2: define fixed layer. Use the mask in Fig. 4.19(2). Etch a few nm into the bottom leads.

9. Ion-Mill 3: isolate device. Use the mask in Fig. 4.19(3). Etch 10-20 nm into the silicon nitride layer.

10. Protect shorts. Use the mask in Fig. 4.19(4). Evaporate SiO_2 with a thickness greater than the overall etch depth, i.e., the distance from the capping layer to the final etch stop in the nitride layer.

11. Extend electrodes. Use the mask in Fig. 4.19(5) and the long electrodes pattern for extension to the edge of the chip (not shown). Sputter or evaporate Cu 200 nm / Pt (sputter) or Au (evaporate) 30 nm.

12. Deposit top electrodes in the IBD ion mill tool or the AJA sputtering tool. Use the mask in Fig. 4.19(6). Clean first with oxygen plasma. If using IBD, do an ion milling for 15 sec to clean the surface, then deposit Cu. Right after this, it is recommended to deposit Au or Pt (by evaporation or sputtering) on top of the Cu. If using AJA, clean surface with Ar back-sputtering, then deposit Cu/Pt bilayers[3].For better X-ray transmission, the thickness of the top electrodes should be thin ($\leq$ 50 nm).

13. Connect top electrodes. Use the mask in Fig.4.19(7). Deposit Cu ~200 nm / Au 30 nm with evaporation or sputtering. Note that the area around the device is covered by photoresist so the metal deposition in this step will not increase the metal thickness directly on top of nanopillar.

KOH Etching

At this stage, all the fabrication steps regarding the devices have been done. Electrical measurements can be performed to characterize the devices. The last yet challenging step is to etch the Si wafer in heated KOH solution to the suspend the devices. KOH is a very aggressive etchant which can etch almost all the materials on our wafers except the low stress silicon nitride layer and

[3]Pt is usually present in the AJA chamber.

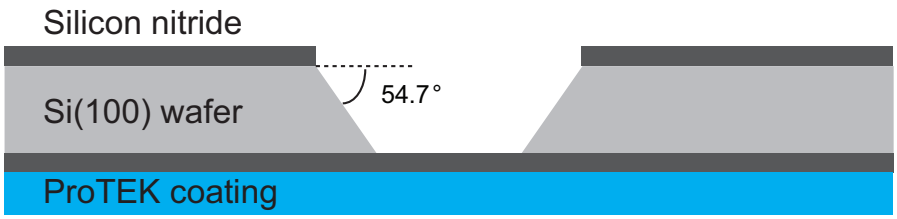

Figure 4.20: Illustration of the anisotropic etch of Si by KOH.

the precious metals such as Au and Pt. It is thus very important to protect the features on the front side of the wafer while the back side is etched in KOH solution. I have developed a process, with help from Vlad Pribiag and Zhipan Li, to achieve this.

The low stress silicon nitride layer is very resistant to KOH etching. So we use the nitride layer on the backside as the etch mask for silicon removal. The size of the final window should be roughly 2 mm by 2 mm, as indicated by the dotted square in Fig. 4.18. The KOH etching of Si is anisotropic - KOH etches Si much faster (a factor of 400) in <100> direction than in <111> direction. For the Si <100> wafer we use, the resulting sidewall will be at an angle of 54.7° relative to the surface, as illustrated in Fig. 4.20. The final window size will be smaller than the mask pattern with the difference related to the thickness of the silicon wafer. This needs to be taken into account when designing the mask for the etch window, especially if a small window size is needed [94]. The etch mask pattern on the back side of the wafer needs to be aligned with the pattern on the front side. This can be done by the EV-620 Contact Aligner at CNF with the backside alignment capability. After the backside photolithography, the nitride layer can be etched by reactive ion etching in the Oxford-81 tool.

To protect the features on the front side of the wafer from the KOH, two measures are used. First, the front side is covered with a protective coating,

ProTEK B3 (made by Brewer Sciences), specifically designed for KOH etching. The coating procedure is the following:

1. Spin ProTEK B3 Primer at 1500 rpm for 60 sec, then bake for 60 sec at 115°C.
2. Spin ProTEK B3 at 2000 rpm for 60 sec, then bake for 4 min at 170°C.

In addition to the ProTEK coating, a mechanical clamp (made by AMMT GmbH) is used to further protect the front side from contact with KOH. When the wafer is loaded in the clamp, O-rings are used on both front and back sides to seal the wafer and reduce mechanical stress on the wafer. This clamp provides very good protection for the front side.

The clamp loaded with the wafer is then put into the KOH solution pre-heated to $\sim$ 90°C. The etch rate is around 2 μm/min. [95] In this step, we only partially etch through the Si wafer, with about 50 μm of silicon left, to avoid possible damage of the nitride membranes and loss of devices during the etching.

The wafer is then cut into individual dies and each die is etched separately. The cutting can be made easy by etching a grid into "V" shape trenches on the back, taking advantages of the anisotropic feature of the KOH etching.

The final etching of the last 50 μm of Si is done chip by chip. During this process, only the ProTEK coating is used. The etching takes about 30 minutes to complete, which can be checked by monitoring whether the nitride window becomes transparent to light. Most of time, the ProTEK coating is good enough for short time etching. Sometimes, the coating near edges of the chip can peel

off. The devices are usually not affected because they are located near the center of the chip, leaving enough room for protection.

After etching, the ProTEK coating can be removed in acetone. All the handling of samples needs be careful from now on since the nitride membrane is already suspended and very easy to break. Each chip should be inspected under an optical microscope to make sure the silicon underneath is completely etched and the surface on top of the nanopillar is clean, free of chemical residuals. Electrical characterization of the devices should also be performed. Good samples are then chosen and mounted onto the sample holder. The last step is to bond gold ribbons from the coplanar waveguide on the sample holder to the sample leads. Complete devices can be stored in glass vials to avoid damage to the nitride membranes and ribbon bonds.

4.4.2 Notes on the Synchronization Circuits

In the X-ray microscopy experiment, the key to perform time-resolved measurements is to achieve reliable synchronization between the microwave drive and the X-ray clock. As discussed briefly in the Experimental Methods section, the microwave frequency needs to be an integer (for XM-1) or fractional (for STXM) harmonic of the X-ray clock frequency as expressed in Eq. 4.2. The circuit diagram to achieve this frequency locking is shown in Fig. 4.7. Here I would like to discuss this synchronization circuit in some more detail.

General Considerations

The idea of the synchronization is to divide the RF frequency f_{RF} down to the same frequency as the X-ray clock frequency f_{clock}. We use frequency divider to achieve this and would prefer a variable division ratio that can be changed depending on the experiment needs. However, the variable-division divider we have has an upper frequency limit of 1 GHz and is not able to process f_{RF}. To solve this problem, we add an additional divider on each leg to prescale the frequencies, f_{RF} and f_{clock}, with the same division ratio. The RF leg is then fed through the variable-division divider. The choices of dividers are different for the two microscopes due to different triggering mechanisms.

Circuit for XM-1

In XM-1, f_{RF} needs to be an integer harmonic of f_{clock}. The circuit for XM-1 is shown in Fig. 4.21. In the RF leg, we actually use three dividers, N_1, N_2 and M. N_1 is a fixed-ratio divider which is able to take signals with frequencies up to 12 GHz. N_2 and M are the same variable-division dividers (made by Pulse Research Labs)[4], which are used to provide NECL[5] interfaces for the digital delay line whose input and output are both NECL standard. When the circuit reaches a steady state, the following frequency relationship holds

$$\frac{f_{RF}}{N_1 N_2 M} = \frac{f_{clock}}{N_0}. \tag{4.3}$$

We choose $N_0 = N_1 N_2$ so that the ratio between f_{RF} and f_{clock} is M which is a variable integer. In our experiment, we use $N_0 = 40$, $N_1 = 20$ and $N_2 = 2$. The

[4]This frequency divider has interfaces for both TTL and NECL.

[5]NECL, standing for Negative Emitter-Coupled Logic, is a logic standard whose logic levels ("1" and "0") are negative voltages.

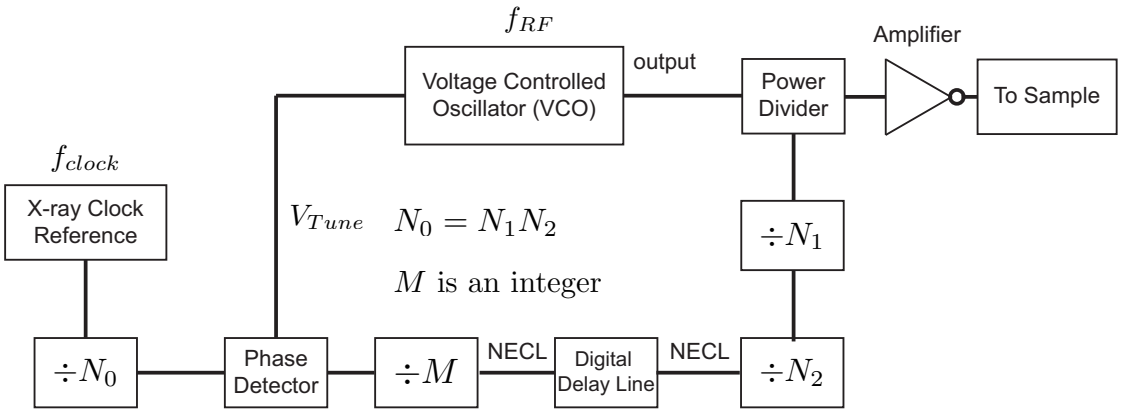

Figure 4.21: The circuit diagram of the phase locked loop designed for XM-1.

digital delay line controls the relative phase between the two frequency. It is in 10 ps steps and can be controlled programmably.

Circuit for STXM

For STXM, f_{RF} needs to be a fractional harmonic of f_{clock} to utilize the multiple counters (up to 16) on STXM. The counters can respond to particular electron buckets in the storage ring. In multi-bunch operation of the storage ring, there are total of $328 = 41 \times 8$ electron buckets evenly spaced in a circle. We need to make sure that the same electron bucket corresponds to the same RF phase so that the counter responding to that electron bucket records signals only at one phase. So the different number of phases we can record is either 41 or 8. In our experiment, we choose to record 8 different phases considering the time resolution is 70 ps while the period corresponding f_{RF} is only a few 100's of ps. So we need to achieve $f_{RF} = (N + 1/8) f_{clock} = (8N + 1)/8 \times f_{clock}$ with N being a variable integer. The circuit for STXM is shown in Fig. 4.22. At the steady state, we have

$$\frac{f_{RF}}{N_1 M} = \frac{f_{clock}}{N_0 N_2}. \tag{4.4}$$

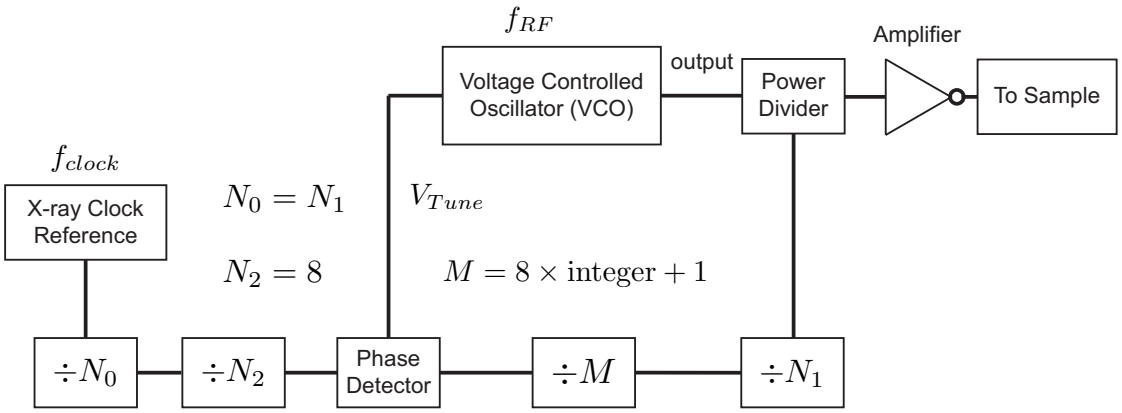

Figure 4.22: The circuit diagram of the phase locked loop designed for STXM.

N_0 and N_1 are to prescale the RF frequency down to acceptable range of the variable-division divider and $N_0 = N_1$. So we have $f_{RF} = (M/N_2) f_{clock}$. With $N_2 = 8$, we simply set $M = 8 \times \text{integer} + 1$ where we set the integer to choose a particular frequency of interest. For example, if we want to image dynamics around 3 GHz, we would set $M = 49$ so that $f_{RF} = (6 + 1/8) f_{clock} = 3.0625$ GHz.

CHAPTER 5

CONCLUSION

In this dissertation, I have described our experimental studies of spin transfer effects, focusing on characterization of the microwave-frequency magnetic dynamics excited by spin torque in a nanoscale magnet.

In the first study, we have demonstrated the proof of principle in achieving resonantly excited spin transfer switching of a nanopillar. The motivation was to take advantage of the precessional motion of the magnetic moment during its switching process. We used a microwave current pulse to resonantly excite the free layer dynamics and then completed the switching with a square current pulse. At low temperature, we observed a strong dependence of the switching probability on the RF phase relative to the onset of the square pulse at the resonance frequency, indicating that the free layer precession excited by spin transfer from the microwave current pulse is coherent and phase locked to the microwave drive. With the assistance of a microwave pulse, the switching time was reduced and achieved a narrower distribution compared to when driven by a square pulse alone, and this can permit significant reductions in the integrated power required for switching. At room temperature, the benefits of resonant excitation were reduced due to strong thermal fluctuations during the square pulse, which dominated the dynamics. Our findings also suggested a way to extend the benefits of resonantly excited switching by inducing a large offset angle between the two magnetic layers so that the microwave pulse can excite the free layer resonantly into large angle precession and only a small square pulse is needed to complete the switching.

In the second study, we have developed a single-shot technique to directly resolve in time domain the magnetic dynamics prior to and during the spin-transfer-driven switching in a magnetic tunnel junction. By optimizing the dynamic range of the time domain measurement, we substantially improved the sensitivity of the measurement which allowed us to directly resolve the resistance oscillations associated with the magnetic dynamics during each individual switching event, obtaining detailed views of switching modes and variations between events. With comparison to micromagnetic simulations, we found that with a small in-plane hard-axis magnetic field the switching dynamics are more spatially coherent than for zero field. The excellent sensitivity also enabled us to perform detailed analyses of spin-transfer-driven magnetic dynamics under the influence of thermal fluctuations, including measurements of the coherent times and the spectra of the magnetic fluctuations during the highly non-equilibrium state prior to switching.

In the third study, we have performed X-ray microscopy experiments at the Advanced Light Source of Lawrence Berkeley National Laboratory, with the goal of imaging the magnetic normal modes which serve as the basis states for the magnetic dynamics excited by spin transfer torque. Using a continuous microwave current to resonantly excite a particular normal mode of interest, we performed time-resolved X-ray microscopy measurements to image the spatial structures of the mode. For initial experiments on samples with a 15 nm free layer, we imaged two modes and observed that they have different degrees of spatial non-uniformity. At low fields where the two modes are close in frequency and excited at the same time, the more non-uniform mode is excited more strongly and dominates the behavior of the dynamics. Further studies are planned to investigate samples with thin (5 nm) free layer so that results

can be connected directly to previous electrical experiments on spin-transfer-driven magnetic dynamics. Though this is still an on-going project, we believe our experiments will provide new insights about the magnetic dynamics on the nano scale.

BIBLIOGRAPHY

[1] S. A. Wolf, D. D. Awschalom, R. A. Buhrman, J. M. Daughton, S. von Molnár, M. L. Roukes, A. Y. Chtchelkanova, and D. M. Treger, "Spintronics: A spin-based electronics vision for the future," *Science* **294**, 1488 (2001).

[2] M. N. Baibich, J. M. Broto, A. Fert, F. N. Van Dau, F. Petroff, P. Etienne, G. Creuzet, A. Friederich, and J. Chazelas, "Giant magnetoresistance of (001)Fe/(001)Cr magnetic superlattices," *Phys. Rev. Lett.* **61**, 2472 (1988).

[3] G. Binasch, P. Grünberg, F. Saurenbach, and W. Zinn, "Enhanced magnetoresistance in layered magnetic structures with antiferromagnetic interlayer exchange," *Phys. Rev. B* **39**, 4828 (1989).

[4] M. Julliere, "Tunneling between ferromagnetic films," *Phys. Lett. A* **54**, 225 (1975).

[5] W. H. Butler, X. Zhang, T. C. Schulthess, and J. M. MacLaren, "Spin-dependent tunneling conductance of Fe|MgO|Fe sandwiches," *Phys. Rev. B* **63**, 054416 (2001).

[6] J. Mathon and A. Umerski, "Theory of tunneling magnetoresistance of an epitaxial Fe/MgO/Fe(001) junction," *Phys. Rev. B* **63**, 220403 (2001).

[7] S. S. P. Parkin, C. Kaiser, A. Panchula, P. M. Rice, B. Hughes, M. Samant, and S. Yang, "Giant tunnelling magnetoresistance at room temperature with MgO (100) tunnel barriers," *Nat. Mater.* **3**, 862 (2004).

[8] S. Yuasa, T. Nagahama, A. Fukushima, Y. Suzuki, and K. Ando, "Giant room-temperature magnetoresistance in single-crystal Fe/MgO/Fe magnetic tunnel junctions," *Nat. Mater.* **3**, 868 (2004).

[9] S. Ikeda, J. Hayakawa, Y. Ashizawa, Y. M. Lee, K. Miura, H. Hasegawa, M. Tsunoda, F. Matsukura, and H. Ohno, "Tunnel magnetoresistance of 604% at 300 K by suppression of Ta diffusion in CoFeB/MgO/CoFeB pseudo-spin-valves annealed at high temperature," *Appl. Phys. Lett.* **93**, 082508 (2008).

[10] J. C. Slonczewski, "Current-driven excitation of magnetic multilayers," *J. Magn. Magn. Mater.* **159**, L1 (1996).

[11] L. Berger, "Emission of spin waves by a magnetic multilayer traversed by a current," *Phys. Rev. B* **54**, 9353 (1996).

[12] E. B. Myers, D. C. Ralph, J. A. Katine, R. N. Louie, and R. A. Buhrman, "Current-Induced switching of domains in magnetic multilayer devices," *Science* **285**, 867 (1999).

[13] J. A. Katine, F. J. Albert, R. A. Buhrman, E. B. Myers, and D. C. Ralph, "Current-driven magnetization reversal and spin-wave excitations in Co/Cu/Co pillars," *Phys. Rev. Lett.* **84**, 3149 (2000).

[14] S. I. Kiselev, J. C. Sankey, I. N. Krivorotov, N. C. Emley, R. J. Schoelkopf, R. A. Buhrman, and D. C. Ralph, "Microwave oscillations of a nanomagnet driven by a spin-polarized current," *Nature* **425**, 380 (2003).

[15] D. Ralph and M. Stiles, "Spin transfer torques," *J. Magn. Magn. Mater.* **320**, 1190 (2008).

[16] J. C. Slonczewski, "Currents and torques in metallic magnetic multilayers," *J. Magn. Magn. Mater.* **247**, 324 (2002).

[17] I. Theodonis, N. Kioussis, A. Kalitsov, M. Chshiev, and W. H. Butler,

"Anomalous bias dependence of spin torque in magnetic tunnel junctions," *Phys. Rev. Lett.* **97**, 237205 (2006).

[18] J. C. Sankey, Y. Cui, J. Z. Sun, J. C. Slonczewski, R. A. Buhrman, and D. C. Ralph, "Measurement of the spin-transfer-torque vector in magnetic tunnel junctions," *Nat. Phys.* **4**, 67 (2008).

[19] H. Kubota, A. Fukushima, K. Yakushiji, T. Nagahama, S. Yuasa, K. Ando, H. Maehara, Y. Nagamine, K. Tsunekawa, D. D. Djayaprawira, N. Watanabe, and Y. Suzuki, "Quantitative measurement of voltage dependence of spin-transfer torque in MgO-based magnetic tunnel junctions," *Nat. Phys.* **4**, 37 (2008).

[20] C. Wang, Y. Cui, J. Z. Sun, J. A. Katine, R. A. Buhrman, and D. C. Ralph, "Bias and angular dependence of spin-transfer torque in magnetic tunnel junctions," *Phys. Rev. B* **79**, 224416 (2009).

[21] C. Wang, Y. Cui, J. A. Katine, R. A. Buhrman, and D. C. Ralph, "Time-resolved measurement of spin-transfer-driven ferromagnetic resonance and spin torque in magnetic tunnel junctions," *Nat. Phys.* **7**, 496 (2011).

[22] R. H. Koch, J. A. Katine, and J. Z. Sun, "Time-resolved reversal of spin-transfer switching in a nanomagnet," *Phys. Rev. Lett.* **92** (2004), 10.1103/PhysRevLett.92.088302.

[23] W. F. Brown, "Thermal fluctuations of a single-domain particle," *Phys. Rev.* **130**, 1677 (1963).

[24] E. B. Myers, F. J. Albert, J. C. Sankey, E. Bonet, R. A. Buhrman, and D. C. Ralph, "Thermally activated magnetic reversal induced by a spin-polarized current," *Phys. Rev. Lett.* **89**, 196801 (2002).

[25] S. Urazhdin, N. O. Birge, W. P. Pratt, and J. Bass, "Current-driven magnetic excitations in Permalloy-Based multilayer nanopillars," *Phys. Rev. Lett.* **91**, 146803 (2003).

[26] S. Urazhdin, H. Kurt, W. P. Pratt, and J. Bass, "Effect of antiferromagnetic interlayer coupling on current-assisted magnetization switching," *Appl. Phys. Lett.* **83**, 114 (2003).

[27] A. Fábián, C. Terrier, S. S. Guisan, X. Hoffer, M. Dubey, L. Gravier, and J. Ansermet, "Current-induced two-level fluctuations in pseudo-spin-valve (Co/Cu/Co) nanostructures," *Phys. Rev. Lett.* **91**, 257209 (2003).

[28] I. N. Krivorotov, N. C. Emley, A. G. F. Garcia, J. C. Sankey, S. I. Kiselev, D. C. Ralph, and R. A. Buhrman, "Temperature dependence of spin-transfer-induced switching of nanomagnets," *Phys. Rev. Lett.* **93**, 166603 (2004).

[29] Z. Li and S. Zhang, "Thermally assisted magnetization reversal in the presence of a spin-transfer torque," *Phys. Rev. B* **69**, 134416 (2004).

[30] D. M. Apalkov and P. B. Visscher, "Spin-torque switching: Fokker-Planck rate calculation," *Phys. Rev. B* **72**, 180405 (2005).

[31] P. M. Braganca, I. N. Krivorotov, O. Ozatay, A. G. F. Garcia, N. C. Emley, J. C. Sankey, D. C. Ralph, and R. A. Buhrman, "Reducing the critical current for short-pulse spin-transfer switching of nanomagnets," *Appl. Phys. Lett.* **87**, 112507 (2005).

[32] L. Liu, T. Moriyama, D. C. Ralph, and R. A. Buhrman, "Reduction of the spin-torque critical current by partially canceling the free layer demagnetization field," *Appl. Phys. Lett.* **94**, 122508 (2009).

[33] A. D. Kent, B. Özyilmaz, and E. del Barco, "Spin-transfer-induced precessional magnetization reversal," *Appl. Phys. Lett.* **84**, 3897 (2004).

[34] O. J. Lee, V. S. Pribiag, P. M. Braganca, P. G. Gowtham, D. C. Ralph, and R. A. Buhrman, "Ultrafast switching of a nanomagnet by a combined out-of-plane and in-plane polarized spin current pulse," *Appl. Phys. Lett.* **95**, 012506 (2009).

[35] S. Mangin, D. Ravelosona, J. A. Katine, M. J. Carey, B. D. Terris, and E. E. Fullerton, "Current-induced magnetization reversal in nanopillars with perpendicular anisotropy," *Nat. Mater.* **5**, 210 (2006).

[36] A. A. Tulapurkar, T. Devolder, K. Yagami, P. Crozat, C. Chappert, A. Fukushima, and Y. Suzuki, "Subnanosecond magnetization reversal in magnetic nanopillars by spin angular momentum transfer," *Appl. Phys. Lett.* **85**, 5358 (2004).

[37] S. Kaka, M. R. Pufall, W. H. Rippard, T. J. Silva, S. E. Russek, J. A. Katine, and M. Carey, "Spin transfer switching of spin valve nanopillars using nanosecond pulsed currents," *J. Magn. Magn. Mater.* **286**, 375 (2005).

[38] T. Devolder, A. Tulapurkar, Y. Suzuki, C. Chappert, P. Crozat, and K. Yagami, "Temperature study of the spin-transfer switching speed from dc to 100 ps," *J. Appl. Phys.* **98**, 053904 (2005).

[39] I. N. Krivorotov, N. C. Emley, J. C. Sankey, S. I. Kiselev, D. C. Ralph, and R. A. Buhrman, "Time-domain measurements of nanomagnet dynamics driven by spin-transfer torques," *Science* **307**, 228 (2005).

[40] N. C. Emley, I. N. Krivorotov, O. Ozatay, A. G. F. Garcia, J. C. Sankey, D. C. Ralph, and R. A. Buhrman, "Time-resolved spin-torque switching and

enhanced damping in Permalloy/Cu/Permalloy spin-valve nanopillars," *Phys. Rev. Lett.* **96**, 247204 (2006).

[41] T. Devolder, J. Hayakawa, K. Ito, H. Takahashi, S. Ikeda, P. Crozat, N. Zerounian, J. Kim, C. Chappert, and H. Ohno, "Single-shot time-resolved measurements of nanosecond-scale spin-transfer induced switching: Stochastic versus deterministic aspects," *Phys. Rev. Lett.* **100**, 057206 (2008).

[42] H. Tomita, K. Konishi, T. Nozaki, H. Kubota, A. Fukushima, K. Yakushiji, S. Yuasa, Y. Nakatani, T. Shinjo, M. Shiraishi, and Y. Suzuki, "Single-shot measurements of spin-transfer switching in CoFeB/MgO/CoFeB magnetic tunnel junctions," *Appl. Phys. Express* **1**, 061303 (2008).

[43] Y. Cui, G. Finocchio, C. Wang, J. A. Katine, R. A. Buhrman, and D. C. Ralph, "Single-shot time-domain studies of spin-torque-driven switching in magnetic tunnel junctions," *Phys. Rev. Lett.* **104**, 097201 (2010).

[44] I. N. Krivorotov, N. C. Emley, R. A. Buhrman, and D. C. Ralph, "Time-domain studies of very-large-angle magnetization dynamics excited by spin transfer torques," *Phys. Rev. B* **77**, 054440 (2008).

[45] J. C. Sankey, I. N. Krivorotov, S. I. Kiselev, P. M. Braganca, N. C. Emley, R. A. Buhrman, and D. C. Ralph, "Mechanisms limiting the coherence time of spontaneous magnetic oscillations driven by dc spin-polarized currents," *Phys. Rev. B* **72**, 224427 (2005).

[46] S. I. Kiselev, J. C. Sankey, I. N. Krivorotov, N. C. Emley, A. G. F. Garcia, R. A. Buhrman, and D. C. Ralph, "Spin-transfer excitations of permalloy nanopillars for large applied currents," *Phys. Rev. B* **72**, 064430 (2005).

[47] K. V. Thadani, G. Finocchio, Z. Li, O. Ozatay, J. C. Sankey, I. N. Krivorotov, Y. Cui, R. A. Buhrman, and D. C. Ralph, "Strong linewidth variation for spin-torque nano-oscillators as a function of in-plane magnetic field angle," *Phys. Rev. B* **78**, 024409 (2008).

[48] W. H. Rippard, M. R. Pufall, S. Kaka, S. E. Russek, and T. J. Silva, "Direct-current induced dynamics in $Co_{90}Fe_{10}/Ni_{80}Fe_{20}$ point contacts," *Phys. Rev. Lett.* **92**, 027201 (2004).

[49] W. H. Rippard, M. R. Pufall, S. Kaka, T. J. Silva, and S. E. Russek, "Current-driven microwave dynamics in magnetic point contacts as a function of applied field angle," *Phys. Rev. B* **70**, 100406 (2004).

[50] V. S. Pribiag, I. N. Krivorotov, G. D. Fuchs, P. M. Braganca, O. Ozatay, J. C. Sankey, D. C. Ralph, and R. A. Buhrman, "Magnetic vortex oscillator driven by d.c. spin-polarized current," *Nat. Phys.* **3**, 498 (2007).

[51] V. S. Pribiag, G. Finocchio, B. J. Williams, D. C. Ralph, and R. A. Buhrman, "Long-timescale fluctuations in zero-field magnetic vortex oscillations driven by dc spin-polarized current," *Phys. Rev. B* **80**, 180411 (2009).

[52] A. M. Deac, A. Fukushima, H. Kubota, H. Maehara, Y. Suzuki, S. Yuasa, Y. Nagamine, K. Tsunekawa, D. D. Djayaprawira, and N. Watanabe, "Bias-driven high-power microwave emission from MgO-based tunnel magnetoresistance devices," *Nat. Phys.* **4**, 803 (2008).

[53] D. Houssameddine, S. H. Florez, J. A. Katine, J. Michel, U. Ebels, D. Mauri, O. Ozatay, B. Delaet, B. Viala, L. Folks, B. D. Terris, and M. Cyrille, "Spin transfer induced coherent microwave emission with large power from nanoscale MgO tunnel junctions," *Appl. Phys. Lett.* **93**, 022505 (2008).

[54] D. Houssameddine, U. Ebels, B. Dieny, K. Garello, J. Michel, B. Delaet, B. Viala, M. Cyrille, J. A. Katine, and D. Mauri, "Temporal coherence of MgO based magnetic tunnel junction spin torque oscillators," *Phys. Rev. Lett.* **102**, 257202 (2009).

[55] L. Bianchini, S. Cornelissen, J. Kim, T. Devolder, W. van Roy, L. Lagae, and C. Chappert, "Direct experimental measurement of phase-amplitude coupling in spin torque oscillators," *Appl. Phys. Lett.* **97**, 032502 (2010).

[56] S. Kaka, M. R. Pufall, W. H. Rippard, T. J. Silva, S. E. Russek, and J. A. Katine, "Mutual phase-locking of microwave spin torque nano-oscillators," *Nature* **437**, 389 (2005).

[57] F. B. Mancoff, N. D. Rizzo, B. N. Engel, and S. Tehrani, "Phase-locking in double-point-contact spin-transfer devices," *Nature* **437**, 393 (2005).

[58] A. A. Tulapurkar, Y. Suzuki, A. Fukushima, H. Kubota, H. Maehara, K. Tsunekawa, D. D. Djayaprawira, N. Watanabe, and S. Yuasa, "Spin-torque diode effect in magnetic tunnel junctions," *Nature* **438**, 339 (2005).

[59] J. C. Sankey, P. M. Braganca, A. G. F. Garcia, I. N. Krivorotov, R. A. Buhrman, and D. C. Ralph, "Spin-transfer-driven ferromagnetic resonance of individual nanomagnets," *Phys. Rev. Lett.* **96**, 227601 (2006).

[60] J. N. Kupferschmidt, S. Adam, and P. W. Brouwer, "Theory of the spin-torque-driven ferromagnetic resonance in a ferromagnet/normal-metal/ferromagnet structure," *Phys. Rev. B* **74**, 134416 (2006).

[61] A. A. Kovalev, G. E. W. Bauer, and A. Brataas, "Current-driven ferromagnetic resonance, mechanical torques, and rotary motion in magnetic nanostructures," *Phys. Rev. B* **75**, 014430 (2007).

[62] G. D. Fuchs, J. C. Sankey, V. S. Pribiag, L. Qian, P. M. Braganca, A. G. F. Garcia, E. M. Ryan, Z. Li, O. Ozatay, D. C. Ralph, and R. A. Buhrman, "Spin-torque ferromagnetic resonance measurements of damping in nanomagnets," *Appl. Phys. Lett.* **91**, 062507 (2007).

[63] D. Berkov and J. Miltat, "Spin-torque driven magnetization dynamics: Micromagnetic modeling," *J. Magn. Magn. Mater.* **320**, 1238 (2008).

[64] Y. Acremann, J. P. Strachan, V. Chembrolu, S. D. Andrews, T. Tyliszczak, J. A. Katine, M. J. Carey, B. M. Clemens, H. C. Siegmann, and J. Stöhr, "Time-resolved imaging of spin transfer switching: Beyond the macrospin concept," *Phys. Rev. Lett.* **96**, 217202 (2006).

[65] J. P. Strachan, V. Chembrolu, Y. Acremann, X. W. Yu, A. A. Tulapurkar, T. Tyliszczak, J. A. Katine, M. J. Carey, M. R. Scheinfein, H. C. Siegmann, and J. Stöhr, "Direct observation of spin-torque driven magnetization reversal through nonuniform modes," *Phys. Rev. Lett.* **100**, 247201 (2008).

[66] V. Chembrolu, J. P. Strachan, X. W. Yu, A. A. Tulapurkar, T. Tyliszczak, J. A. Katine, M. J. Carey, J. Stöhr, and Y. Acremann, "Time-resolved x-ray imaging of magnetization dynamics in spin-transfer torque devices," *Phys. Rev. B* **80**, 024417 (2009).

[67] D. P. Bernstein, B. Bräuer, R. Kukreja, J. Stöhr, T. Hauet, J. Cucchiara, S. Mangin, J. A. Katine, T. Tyliszczak, K. W. Chou, and Y. Acremann, "Nonuniform switching of the perpendicular magnetization in a spin-torque-driven magnetic nanopillar," *Phys. Rev. B* **83**, 180410 (2011).

[68] F. J. Albert, J. A. Katine, R. A. Buhrman, and D. C. Ralph, "Spin-polarized

current switching of a Co thin film nanomagnet," *Appl. Phys. Lett.* **77**, 3809 (2000).

[69] J. Z. Sun, "Spin-current interaction with a monodomain magnetic body: A model study," *Phys. Rev. B* **62**, 570 (2000).

[70] T. Devolder, C. Chappert, J. A. Katine, M. J. Carey, and K. Ito, "Distribution of the magnetization reversal duration in subnanosecond spin-transfer switching," *Phys. Rev. B* **75**, 064402 (2007).

[71] K. Rivkin and J. B. Ketterson, "Switching spin valves using rf currents," *Appl. Phys. Lett.* **88**, 192515 (2006).

[72] S. H. Florez, J. A. Katine, M. Carey, L. Folks, and B. D. Terris, "Modification of critical spin torque current induced by rf excitation," *J. Appl. Phys.* **103**, 07A708 (2008).

[73] S. H. Florez, J. A. Katine, M. Carey, L. Folks, O. Ozatay, and B. D. Terris, "Effects of radio-frequency current on spin-transfer-torque-induced dynamics," *Phys. Rev. B* **78**, 184403 (2008).

[74] J.-G. Zhu, X. Zhu, and Y. Tang, "Microwave assisted magnetic recording," *Magnetics, IEEE Transactions on* **44**, 125 (2008).

[75] T. Devolder, P. Crozat, J. Kim, C. Chappert, K. Ito, J. A. Katine, and M. J. Carey, "Magnetization switching by spin torque using subnanosecond current pulses assisted by hard axis magnetic fields," *Appl. Phys. Lett.* **88**, 152502 (2006).

[76] T. Devolder, C. Chappert, and K. Ito, "Subnanosecond spin-transfer switching: Comparing the benefits of free-layer or pinned-layer biasing," *Phys. Rev. B* **75**, 224430 (2007).

[77] G. Finocchio, I. N. Krivorotov, L. Torres, R. A. Buhrman, D. C. Ralph, and B. Azzerboni, "Magnetization reversal driven by spin-polarized current in exchange-biased nanoscale spin valves," *Phys. Rev. B* **76**, 174408 (2007).

[78] J. C. Sankey, *Microwave-frequency characterization of spin transfer and individual nanomagnets*, Ph.D. Dissertation, Cornell University (2007).

[79] P. W. Anderson and H. Suhl, "Instability in the motion of ferromagnets at high microwave power levels," *Phys. Rev.* **100**, 1788 (1955).

[80] S. Yuasa and D. D. Djayaprawira, "Giant tunnel magnetoresistance in magnetic tunnel junctions with a crystalline MgO(001) barrier," *J. Phys. D* **40**, R337 (2007).

[81] S. Serrano-Guisan, K. Rott, G. Reiss, J. Langer, B. Ocker, and H. W. Schumacher, "Biased quasiballistic spin torque magnetization reversal," *Phys. Rev. Lett.* **101**, 087201 (2008).

[82] N. C. Emley, *Magnetic multilayer nanopillars for the study of current-induced reversal of a thin magnetic layer*, Ph.D. Dissertation, Cornell University (2005).

[83] G. Finocchio, B. Azzerboni, G. D. Fuchs, R. A. Buhrman, and L. Torres, "Micromagnetic modeling of magnetization switching driven by spin-polarized current in magnetic tunnel junctions," *J. Appl. Phys.* **101**, 063914 (2007).

[84] D. Aurélio, L. Torres, and G. Finocchio, "Magnetization switching driven by spin-transfer-torque in high-TMR magnetic tunnel junctions," *J. Magn. Magn. Mater.* **321**, 3913 (2009).

[85] K. Ito, T. Devolder, C. Chappert, M. J. Carey, and J. A. Katine, "Micromagnetic simulation on effect of oersted field and hard axis field in spin transfer torque switching," *J. Phys. D* **40**, 1261 (2007).

[86] S. Petit, C. Baraduc, C. Thirion, U. Ebels, Y. Liu, M. Li, P. Wang, and B. Dieny, "Spin-torque influence on the high-frequency magnetization fluctuations in magnetic tunnel junctions," *Phys. Rev. Lett.* **98**, 077203 (2007).

[87] J. Stöhr, "Exploring the microscopic origin of magnetic anisotropies with x-ray magnetic circular dichroism (XMCD) spectroscopy," *J. Magn. Magn. Mater.* **200**, 470 (1999).

[88] J. Stöhr, "Magnetic dichroism spectroscopy and microscopy," http://ssrl.slac.stanford.edu/stohr/xmcd.htm, retrieved in July 2011.

[89] G. Schütz, W. Wagner, W. Wilhelm, P. Kienle, R. Zeller, R. Frahm, and G. Materlik, "Absorption of circularly polarized x rays in iron," *Phys. Rev. Lett.* **58**, 737 (1987).

[90] http://www.cxro.lbl.gov/BL612/index.php?content=resolution.html, retrieved in July 2011.

[91] J. P. Strachan, *Time-resolved X-ray imaging of magnetic nanostructures driven by spin-transfer torque*, Ph.D. Dissertation, Stanford University (2007).

[92] R. D. McMichael and M. D. Stiles, "Magnetic normal modes of nanoelements," *J. Appl. Phys.* **97**, 10J901 (2005).

[93] http://www.cxro.lbl.gov/BL612/index.php?content=sampleinfo.html, retrieved in July 2011.

[94] V. S. Pribiag, *Spin-dependent transport and X-ray imaging of microwave-frequency magnetic vortex oscillations in nanoscale spin valves*, Ph.D. Dissertation, Cornell University (2010).

[95] http://www.cleanroom.byu.edu/KOH.phtml, retrieved in July 2011.